

*Preprint of a book chapter (chapter 3) published in Compendium on Electromagnetic Analysis © [2020] copyright World Scientific Publishing Company,
<https://doi.org/10.1142/10987> — August 2020*

Citation: F. Costa and M. Borgese, “Metamaterials metasurfaces and applications,” in *Compendium on Electromagnetic Analysis*. Singapore: World Scientific, 2020, ch. 3, pp. 89–169. https://doi.org/10.1142/9789813270305_0003

Metamaterials, Metasurfaces and Applications

Filippo Costa, Michele Borgese

I. METAMATERIALS, METASURFACES AND APPLICATIONS

This chapter is a high level introduction to metamaterials, metasurfaces and Frequency Selective Surfaces (FSS). A brief description of the basic theoretical aspects and possible applications of these composite structures are presented. The focus is posed on the some important concepts which allowed the design of innovative devices. It is chosen to limit the number of formulas to only those really necessary. Given the extent of the subject, the presented material has not the ambition to be an exhaustive review of metamaterials but it might be a useful starting point for educational purpose, for beginners or for engineers who need to approach this complex and pervasive research topic.

CONTENTS

I	Metamaterials, Metasurfaces and Applications	2
II	Introduction	5
III	Electromagnetic Metamaterials	6
III-A	Metamaterial classification	6
III-B	Artificial negative dielectric permittivity medium	7
III-C	Artificial negative magnetic permeability medium	9
IV	Retrieving Constitutive Parameters of bulk metamaterials	11
V	Metasurfaces: Synthesis and Circuit Model	14
V-A	Quasistatic Region	18
V-B	Resonant region	18
V-B1	Cell periodicity	19
V-B2	Dielectric effect	20
V-B3	Incidence angle	20
V-B4	Anisotropic Metasurfaces	21
V-C	Multimode region	21
VI	Generalized Snell's Law	23
VII	Artificial Impedance Surfaces (AIS)	24
VII-A	Surface waves on AIS	27
VIII	Tunable Metasurfaces	30
VIII-A	Lumped loaded FSSs	31
VIII-A1	Liquid crystal substrates	31
VIII-A2	Conductivity change of periodic patterns	32
IX	Acoustic Metamaterials	33
X	Application Examples	36
X-A	Cloaking	36

X-A1	Coordinates transformation	37
X-A2	Hard/soft surfaces	38
X-A3	Coordinate transformation vs hard/soft surfaces	39
X-A4	Transmission line cloaking	39
X-A5	Metal plate cloaking	40
X-A6	Scattering cancellation	40
X-A7	Mantle cloaking	40
X-B	Electromagnetic Absorbers	41
X-C	Radomes and Low-RCS antennas	48
X-C1	Wide Angle Impedance Matching (WAIM)	49
X-C2	Rasorbers	50
X-C3	Low-RCS antennas	50
X-D	Wavefront modification through reflecting artificial surfaces	51
X-D1	Reflectarray antennas	52
X-D2	Reflecting Intelligent Surfaces	53
X-E	Polarization Converters	54
X-F	Antennas based on AIS surfaces	57
X-G	Leaky Antennas	59
X-G1	Uniform/quasi-uniform	61
X-G2	Periodic	61
X-G3	Holografic	62
X-H	Chipless RFID	63
X-I	Metamaterial sensors and chipless wireless sensors	68
References		69

II. INTRODUCTION

The concept of metamaterial [1] dates back to the well-known seminal paper of Viktor Veselago [2]. In this work, he posed himself a rhetorical question: “*what would happen in a material if both the electric permittivity and the magnetic permeability are negative?*”

Even if this question remained unanswered for some time, three decades later Smith et al. [3] designed an artificial material which, in the same frequency band, could produce both negative permittivity and negative permeability. The negative index materials was designed by employing two known ingredients: a wire medium which is suitable for synthesizing negative dielectric permittivity [4], [5] and a a split ring resonator medium which is suitable for synthesizing magnetic with effective negative permeability [6]. They showed experimentally that electromagnetic waves cannot propagate in a medium in which one of the materials constant is negative, but propagation is restored when they are both negative. According to Veselago, the refractive index is negative and hence they should be able to observe negative refraction. Although the existence of negative refractive index was a sensational discover, at the beginning it was not employable in practical applications.

Indeed, the initially proposed applications like cloaking and perfect lenses, even though they have able to provide a sensational hype to the subject with articles on famous magazines, do not find immediate application on daily life problems. After these initials claims, the metamaterial field has evolved and a better comprehension of the phenomena has brought artificial materials towards less sensational but more useful and practical applications.

The most appealing aspect of metamaterials is the possibility to realize artificial materials with electromagnetic properties which are not available in nature. In addition, these properties are particularly desirable in several practical applications. Potential applications of metamaterials are microwave and optical filters, medical devices, remote aerospace applications, sensors, smart solar power management, radomes, electromagnetic absorbing materials, high-frequency battlefield communication and lenses. Similar concepts can also be used to modify the behaviour of acoustic waves.

The scientific research of metamaterial is interdisciplinary and involves such fields as electrical engineering, electromagnetism, acoustic, classical optics, solid state physics, microwave and antennae engineering, optoelectronics, material sciences, mechanical engineering, nanoscience and semiconductor engineering.

III. ELECTROMAGNETIC METAMATERIALS

Electromagnetic properties of natural or chemically synthesized materials are determined mainly by their chemical composition [7]. On the contrary, within the metamaterial paradigm, the electromagnetic properties of materials can be controlled not only by varying chemical composition but also by engineering meta-atoms shapes and their internal structures, as well as mutual positions and orientations of meta-atoms in the composite material [7]. Metamaterials can be designed to absorb, reflect, transmit or deviate electromagnetic waves. Therefore, the design of metamaterials involves additional degrees of freedom with respect to conventional materials [8].

A metamaterial is a composite material formed by a mixture of metals and dielectrics. The materials are usually arranged in repeating patterns, at scales that are much smaller than the wavelengths of the phenomena they interact with. Metamaterials properties derive from the properties of the substrate materials but also from their precise shape, geometry, size, orientation and arrangement. As long as the meta-atom sizes are sufficiently small with respect to the wavelength of interest, the same approaches to the macroscopic description of electromagnetic properties of matter can be applied to metamaterials made of meta-atoms, just like to ordinary materials formed by atoms or molecules.

As previously pointed out, metamaterials are formed by a periodic arrangement of particles and can be distinguished from photonic crystals for which the period is comparable to (or larger than) the guided wavelength. Photonic crystals operate in the Bragg regime where the periodic structure is diffractive rather than refractive, and it cannot be characterized in terms of a single refractive index [9].

The 2D version of metamaterials, formed by engineered meta-atoms arranged in a plane, are called metasurfaces [1].

A metafilm (also referred to as a metasurface) is the surface equivalent of a metamaterial. More precisely, a metafilm is a surface distribution of suitably chosen electrically small scatterers. Metafilms are becoming popular as an alternative to full three-dimensional metamaterials [8].

A. Metamaterial classification

Metamaterials are generally made of periodic arrangements and satisfy the effective medium condition only over a restricted frequency bandwidth. A classification of materials is reported in Fig. 1.

- **Double positive medium (DPS)** Double positive mediums (DPS) do occur in nature, such as naturally occurring dielectrics. Permittivity and magnetic permeability are both positive and wave propagation is in the forward direction.
- **Epsilon Negative Media (ENG)** Epsilon negative media (ENG) display a negative ϵ_r , while μ_r is positive. Many plasmas exhibit this characteristic. For example, noble metals such as gold or silver are ENG in the infrared and visible spectrums. Metamaterials behaving like ENG can be synthesized by using a wire medium [5].
- **Mu-Negative Media (MNG)** Mu-negative media (MNG) display a positive ϵ_r and negative μ_r . Gyrotropic or gyromagnetic materials, which are altered by the presence of a quasistatic magnetic field, exhibit this characteristic. Metamaterials behaving like MNG can be synthesized by using a periodic arrangement of split Ring Resonators (SRR) or Spiral Resonators (SR) [6].
- **Double Negative (DNG)** In negative-index metamaterials (NIM), both permittivity and permeability are negative, resulting in a negative index of refraction [15]. These are also known as double negative metamaterials or double negative materials (DNG). Other terms for NIMs include “left-handed media”, “media with a negative refractive index”, and “backward-wave media”. Metamaterials behaving like DNG medium have been synthesized by combining thin wires and split ring resonators.

Categorizing metamaterials into double or single negative, or double positive, it seems that the metamaterial has independent electric and magnetic responses described by ϵ and μ . However, in many cases, the electric field causes magnetic polarization, while the magnetic field induces electrical polarization, known as magnetoelectric coupling. Such media are denoted as bi-isotropic [10].

B. Artificial negative dielectric permittivity medium

A structure consisting of a square matrix of infinitely long parallel thin metal wires, embedded in a dielectric medium, can be used to synthesize negative permittivity over a certain frequency range. The layout of the artificial plasma is shown in Fig. 2a. The relative dielectric permittivity of composite material is negative at frequency $\omega < \omega_p$, where ω_p is the plasma frequency of the structure. Its value depends on the radius and placement period of wires, therefore plasma frequency of such structure is controlled.

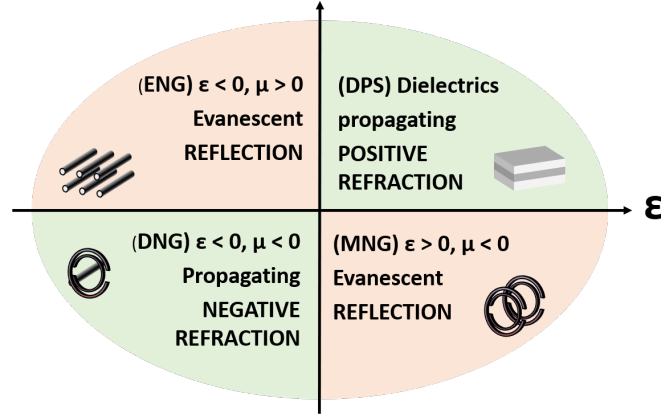


Fig. 1: Classification of metamaterials.

If an electric field, polarized along the direction of the wires, is impinging on the structure, the (free) electrons inside the wires will be forced to move in the direction of the incident field. If the wavelength of the incident field is considerably larger compared to the side length of the unit cell, $\lambda \gg a$, then the whole structure will appear (to the incident electromagnetic field) as an effective medium whose electrons (confined in the wires) move in the $+z$ direction.

It can be characterized like a uniaxial medium with a tangent dielectric permittivity equal to the dielectric permittivity of the hosting medium and a normal dielectric permittivity computed according to theory of wire media [5]:

$$\varepsilon_n = \varepsilon_r \left(1 - \frac{k_p^2}{k_0^2 \varepsilon_r} \right) \quad (1)$$

where k_p is called “plasma wavenumber” and its local approximation reads:

$$k_p = \frac{1}{a \sqrt{\frac{1}{2\pi} \ln \left(\frac{a^2}{4r_0(a-r_0)} \right)}} \quad (2)$$

Where r_0 is the radius of the wires, a is the lattice constant, ε_n represents the normal component of the permittivity which, differently from an ordinary medium, differs from ε_t .

The normal component of the relative permittivity of a wire medium equals zero in correspondence of the so-called plasma frequency and it is negative below this frequency. We recognize an effective permittivity as in the Drude model. The grounded wire array, as well as its infinite counterpart, is strongly dispersive even in the low frequency range [11]. However, if metallic patches are accommodated above the wires, the current along the wires are almost constant and

the spatial dispersion is suppressed [12], [13]. The suppression of the spatial dispersion in the wire array allows for the adoption of a local model to approximate the behavior of the wire array [13]. The position of the plasma resonance is determined by the radius of the vias as shown in Fig. 2b. Since the wire medium is an anisotropic medium, triple wire medium have been proposed to obtain an homogeneous negative permittivity medium [14].

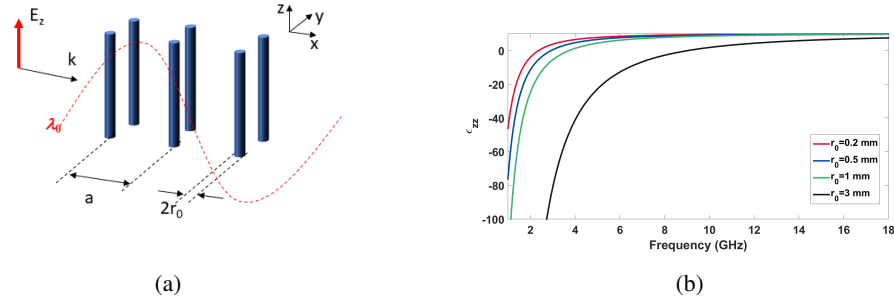


Fig. 2: (a) Layout of the wire medium. (b) frequency behaviour of the effective dielectric permittivity.

C. Artificial negative magnetic permeability medium

Artificial materials exhibiting magnetic activity can be designed through a periodic arrangement of particles interacting with magnetic fields. Two popular particles employed to synthesize miniaturized magnetic resonators are the split ring resonator and the spiral resonator. The layout of the periodic structure is shown in Fig. 3a.

The relative magnetic permeability of this artificial medium can be calculated by resorting to LC equivalent circuit model of the resonators. Both SRR and Spiral resonators can be described as a series LC model. Differently from a wire medium, where the inductive response is the major contribution, these resonators are characterized by a non-negligible capacitance. An expression for the normal component of the magnetic permeability is the following [6]:

$$\mu_n = 1 - \frac{\frac{\pi r_0^2}{a^2}}{1 - \frac{3dc_0^2}{\pi\omega^2 r_0^3} + j\frac{2\sigma}{\omega r_0 \mu_0}} \quad (3)$$

where r_0 is the radius of the split ring resonator and d represents the gap between the two cut loops and c_0 is the speed of light. According to this model, which follows a Lorentzian behavior, the

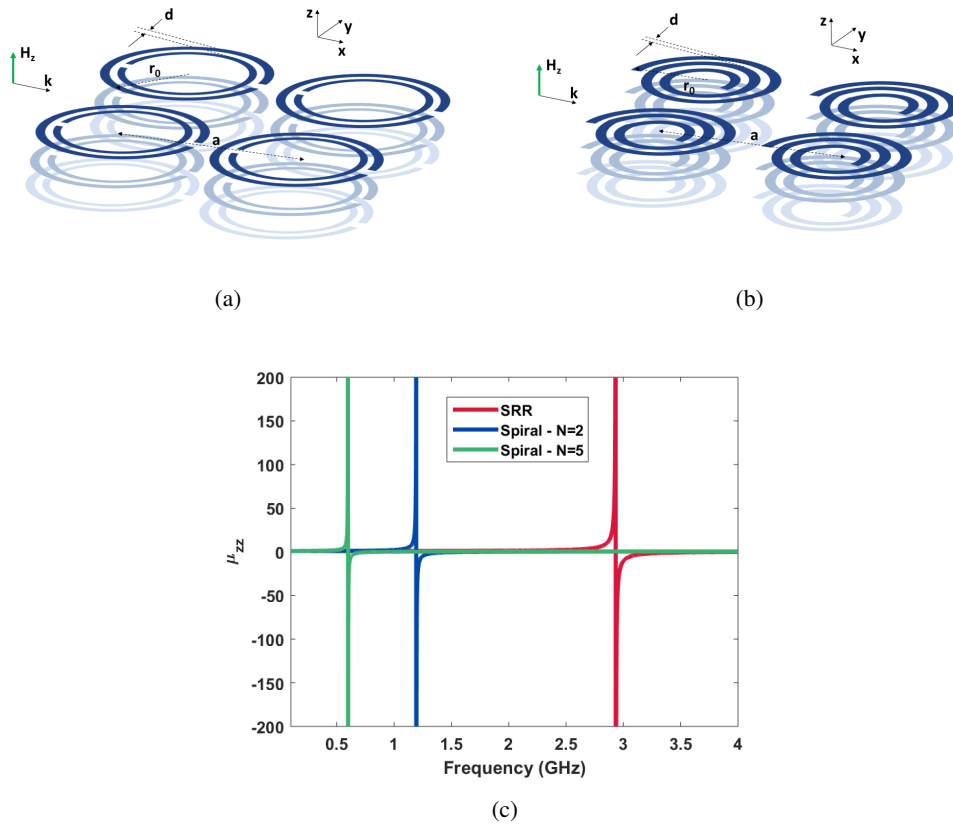


Fig. 3: (a) Layout of the SRR and spiral resonator medium. (b) frequency behaviour of the effective magnetic permeability. (c) Frequency behavior of the effective magnetic permeability

value of the magnetic permeability becomes negative between two frequencies, the self-resonance ω_0 :

$$\omega_0 = \sqrt{\frac{3dc_0^2}{\pi^2 r_0^3}} \quad (4)$$

and the magnetic plasma resonance ω_{mp} :

$$\omega_{mp} = \sqrt{\frac{3dc_0^2}{\pi^2 r_0^3 \left(1 - \frac{\pi r_0^2}{a^2}\right)}} \quad (5)$$

An improved level of miniaturization can be achieved by employing spiral resonators, for which the resonance frequency strictly depends on the number of turns of the miniaturized

spiral N :

$$\mu_n = 1 - \frac{\frac{\pi r_0^2}{a^2}}{1 - \frac{dc_0^2}{2\pi^2\omega^2 r_0^3(N-1)} + j\frac{2\sigma}{\omega r_0\mu_0(N-1)}} \quad (6)$$

The typical behaviour of the magnetic permeability of the SRR medium and the spiran resonator medium with two different number of turns is shown in Fig. 3b. The structures shown above give magnetic properties when the field is aligned along the axes of the cylinders, but have essentially zero magnetic response in other directions. An isotropic version of the material can be obtained by a three-dimensional arrangement of the SRR or SR [6].

IV. RETRIEVING CONSTITUTIVE PARAMETERS OF BULK METAMATERIALS

One of the most popular procedure for the electromagnetic (EM) characterization of materials and metamaterials is the Nicolson-Ross-Weir (NRW) method [15]. It is based on Transmission/Reflection (T/R) measurements of the specimen under test. In this way, a metamaterial may be described like a natural material, with local effective permittivity and permeability, and aims at extracting these parameters. However, the inversion approach cannot ensure that the extracted parameters have a proper physical meaning [16]. Even if the NRW approach is appealing for its simplicity, it often provides constitutive parameters with non-physical frequency dispersion, in particular near the inclusion resonances, yielding complex values of permittivity and permeability that violate basic passivity and causality constraints [16]. In particular, frequency bands in which one of the two retrieved parameters experiences a non-physical anti-resonant response with negative slope and negative imaginary part are common in metamaterial retrieval procedures. The properties of materials are retrieved from their impedance and the wave velocities in the materials. The main drawback of this method is related to the ambiguities in the determination of the electrical parameters when the thickness of the specimen is an integer multiple of a half wavelength in the material [17]. Since the guided wavelength in a material and especially in a metamaterial is unknown *a priori*, the ambiguities are not easily removable. For the characterization of a material sample with a thickness d , the latter is located inside a two-port microwave device such as a coaxial cable or a waveguide. According to the theory of multiple reflections [15], the scattering parameters of the finite length sample (S_{11} and S_{21}) can

be written as a function of the reflection coefficient at the interface of two infinite media Γ and as a function of the phase factor T :

$$S_{11} = \Gamma_{IN} = \frac{\Gamma(1 - T^2)}{1 - \Gamma^2 T^2}, \quad S_{21} = \frac{(1 - \Gamma^2)T}{1 - \Gamma^2 T^2} \quad (7)$$

where the phase factor (T) and the reflection coefficient Γ are defined as:

$$\begin{cases} T = e^{-j k d} = e^{-\gamma d}, \\ \Gamma = \frac{Z_1 - Z_0}{Z_1 + Z_0} \end{cases} \quad (8)$$

where Z_0 and Z_1 are the transmission line characteristic impedance in case of the absence and in the presence of the sample, respectively.

By rearranging equations (7), the reflection coefficient Γ , which contains the impedance of the unknown medium, and the phase factor T , which contains the propagation constant of the unknown medium, can be expressed as a function of the scattering parameters of the sample:

$$\begin{cases} \Gamma = K \pm \sqrt{K^2 - 1} \\ T = \frac{S_{11} + S_{21} - \Gamma}{1 - (S_{11} + S_{21})\Gamma} = |T| e^{-j\phi} \end{cases} \quad (9)$$

where K is an auxiliary parameter which is a function of the scattering parameters as: $K = \frac{S_{11}^2 - S_{21}^2 + 1}{2S_{11}}$.

As is apparent in equation (9), the reflection coefficient Γ is characterized by a sign ambiguity. The sign should be properly chosen to obtain the correct impedance and propagation constant of the medium [18], [19] (passivity condition) which can be verified at the end of the inversion procedure. However, if one needs to estimate only the dielectric permittivity and the magnetic permeability of the medium, both signs can be arbitrarily chosen. Indeed, since the dielectric permittivity and the magnetic permeability are a product of the impedance of the medium and its propagation constant, the correct sign is always restored [17].

Since the phase factor T of relation (8) is a complex number characterized by an amplitude $|T|$ and a phase term ϕ , the propagation constant γ can be obtained by applying the natural logarithm of the complex variable T . The natural logarithm of the complex variable T will be complex. Its real part can be expressed as the logarithm of its amplitude and the imaginary part will be the phase term ϕ plus a 2π phase ambiguity:

$$\gamma = jk = \frac{1}{d} [-\ln(|T|) - j\phi + j2\pi n], \quad n = \dots - 2, -1, 0, 1, 2 \dots \quad (10)$$

It is evident from equation (10) that there is an ambiguity in the calculation of γ because of the term $2\pi n$. The existence of an infinite number of valid solutions is called *branching*. Therefore, in order to solve this ambiguity, the NRW method requires a thin specimen material (usually smaller than a quarter of wavelength) so that $n=0$ at the analysed frequencies. In a waveguide environment [20], the magnetic permeability can be similarly calculated by using the equivalent transmission line circuit of the waveguide:

$$\mu_r = \frac{\gamma}{\gamma_0} \frac{Z^{TE}}{Z_0^{TE}} = \frac{\sqrt{k_0^2 \epsilon_r \mu_r - k_t^2}}{\sqrt{k_0^2 - k_t^2}} \frac{\omega \mu_0 \mu_r}{\sqrt{k_0^2 \epsilon_r \mu_r - k_t^2}} \frac{\sqrt{k_0^2 - k_t^2}}{\omega \mu_0} \quad (11)$$

where k_0 is the propagation constant in free space and k_t is the cut off wavenumber of the waveguide. On the contrary, the dielectric permittivity should be derived from the propagation constant ($k = \sqrt{k_0^2 \epsilon_r \mu_r - k_t^2}$) after the derivation of the magnetic permeability:

$$\epsilon_r = \frac{k^2 + k_t^2}{k_0^2 \mu_r} \quad (12)$$

An example of application of the NRW procedure for the characterization of a dielectric material is reported hereinafter [21]. A homogeneous material sample with thickness equal to 8 mm and $\epsilon_r = 9 - j0$, $\mu_r = 1 - j0$ is considered. The transmission and reflection coefficient simulated with a transmission line model are reported in Fig. 4-(a).

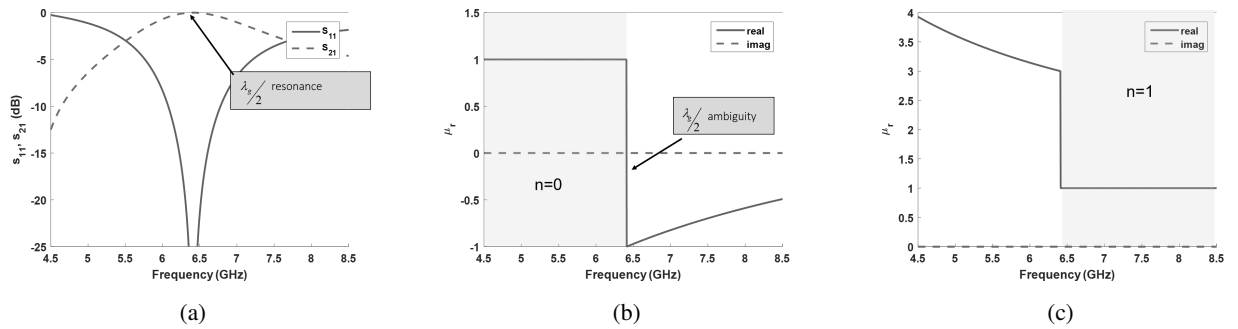


Fig. 4: (a) amplitude of the transmission and the reflection coefficient of a rectangular sample of 8 mm thickness with $\epsilon_r = 9 - j0$, $\mu_r = 1 - j0$ (b) ambiguity in the obtained relative permeability for $n = 0$ applying the NRW procedure (c) ambiguity in the obtained relative permeability for $n = 1$ applying the NRW procedure.

The application of the NRW with $n = 0$ and $n = 1$ provides the results reported in Fig. 4-(b) and (c). As is evident from the graphs, when the thickness of the sample is equal to half wavelength in the dielectric media ($\lambda_g/2$), the NRW method produces ambiguous results. In this

particular case, the thickness of the sample is equal to $\lambda_g/2$ at 6.4 GHz. The results obtained with $n=0$ are valid up to 6.4 GHz, where the estimated parameters are constant with frequency. Similarly, with $n = 1$, the results are valid starting from 6.4 GHz. Therefore, it is evident that this formulation of the NRW method implies the need to choose the valid results depending on the different values of n . In order to overcome the limitations of the branch point selection, a stepwise scheme of the NRW method has been proposed [22]. The procedure is based on the circumstance that the measured sample is thinner than half-guided wavelength at the lowest frequency. Therefore, the propagation constant is computed according to equation 10 by putting the $n=0$. The argument of the propagation constant for the subsequent frequency points p is selected by using a step-by-step increment which avoids the selection of the branch value n :

$$\phi(p) = \phi(p-1) + \arg\left(\frac{T(p)}{T(p-1)}\right) = \phi(0) + \sum_{p=1}^n \arg\left(\frac{e^{jk_{M,p}d}}{e^{jk_{M,p-1}d}}\right) \quad (13)$$

If the sample is thicker than a half-guided wavelength at the lowest frequency, unphysical solutions are obtained also by using the stepwise method. The NRW direct inversion procedure is sensitive to the inaccuracies of the S-parameters at the $N\lambda_g/2$ resonances, with N entire number. Indeed, at that frequency, the sample becomes a half-wavelength window and the reflection coefficient tends to zero. Consequently, it is not possible to apply the direct inversion procedure. Moreover, in the case of noisy measurements, this method will induce a high uncertainty in the extracted parameters of the material and may cause problems in finding the correct branch in the vicinity of these frequencies [23]. The estimation error depends on the accuracy of the available scattering parameters [24].

V. METASURFACES: SYNTHESIS AND CIRCUIT MODEL

Metasurfaces can be seen as the bidimensional version of bulk metamaterials. They are becoming much more popular than the 3D counterpart because of the simplicity in the fabrication process and their numerous practical applications. The presence of a metasurface constitutes discontinuity for a propagating wave [25]. The complex field distribution in the vicinity of the metasurface can be explained with the presence of a relevant number of evanescent high-order modes. The first order effect of the discontinuity can appropriately be accounted for by a frequency-independent capacitance/inductance for TM/TE polarization [26]. The analysis of a metasurface can be therefore computed by resorting to a transmission line model where the metasurface is represented by a shunt impedance. The real part of the equivalent impedance

R , takes into account ohmic losses in the metal and in dielectric layers and the reactance X , represents the inductive or capacitive nature of the periodic surface. The transmission and reflection coefficients (s_{11} , s_{21}) of the metasurfaces or Frequency Selective Surfaces (FSS) can be computed according to the standard transmission line relations:

$$s_{11} = \frac{AZ_0 + B - CZ_0^2 - DZ_0}{AZ_0 + B + CZ_0^2 + DZ_0}, \quad (14)$$

$$s_{21} = \frac{2Z_0}{AZ_0 + B + CZ_0^2 + DZ_0}. \quad (15)$$

where A, B, C, D represents the terms of the $ABCD$ matrix of the system comprising the FSS and a generic number N of dielectrics [27]:

$$\begin{bmatrix} A & B \\ C & D \end{bmatrix} = [M_1] \cdot \dots \cdot [M_n] \cdot [M_{FSS}] \cdot [M_{n+1}] \cdot \dots \cdot [M_N] \quad (16)$$

In equation (16) the subscript n represents the n^{th} dielectric substrate and M are the ABCD matrix of every layer:

$$[M_n] = \begin{bmatrix} \cos(k_{zn}d_n) & jZ_n \sin(k_{zn}d_n) \\ j\frac{\sin(k_{zn}d_n)}{Z_n} & \cos(k_{zn}d_n) \end{bmatrix}, \quad (17)$$

$$[M_{FSS}] = \begin{bmatrix} 1 & 0 \\ 1/Z_{FSS} & 1 \end{bmatrix}$$

where Z_{FSS} is the approximate FSS impedance computed with the retrieved LC parameters, $Z_n^{TE} = (\omega\mu_r\mu_0)/k_{zn}$; $Z_n^{TM} = k_{zn}/(\omega\varepsilon_r\varepsilon_0)$ are the characteristic impedance of the slab for TE and TM polarization, $k_{zn} = \sqrt{\varepsilon_r k_0^2 - k_t^2}$ is the normal component of the wavenumber and $k_t = k_0 \sin(\vartheta)$ is the transverse component of the wavenumber with ϑ representing the incidence angle of the incoming wave with respect to the normal and k_0 the free space propagation constant. The quantities ε_0 , ε_r , μ_0 , μ_r represent the free space and the relative dielectric permittivity and magnetic permeability. Since the FSS is a passive reciprocal system, the transmission coefficient of the structure is identical independently of the incidence side. If the analyzed configuration is symmetric (same dielectrics on both side of the FSS) also the reflection coefficients computed on the two sides of the FSS coincide (symmetric scattering matrix). An important parameter in

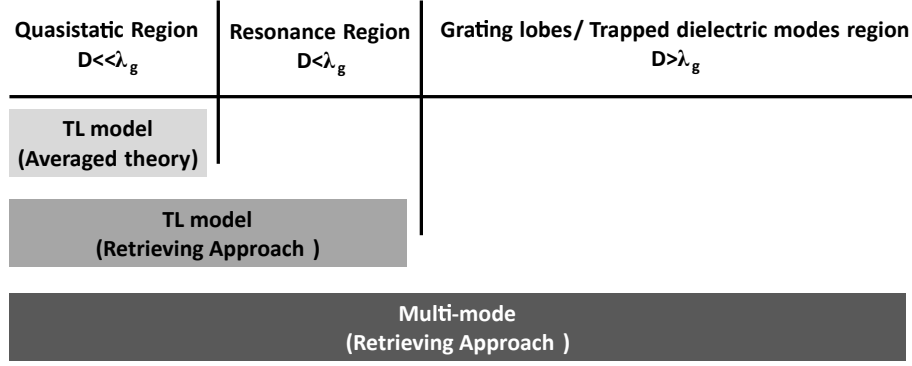


Fig. 5: Characteristic regions and analytic models employed to characterize the frequency response of FSSs.

the FSS analysis is the wavelength at which the grating lobes onset [28]. For freestanding FSS, the wavelength of the first grating lobe reads:

$$\lambda_g^{\varepsilon_r} = D (\sqrt{\varepsilon_r} + \sin(\vartheta)) \quad (18)$$

where D represents the inter-element spacing, c is the speed of light and θ is the incident angle. For wavelengths longer than λ_g (or frequencies smaller than c/λ_g) the only propagating Floquet mode is the fundamental one. Higher modes are evanescent and decay exponentially away from the mesh. At normal incidence the grating lobes wavelength is equal to the FSS periodicity ($\lambda_g = D$). In the analysis of periodic structures, three different fundamental regions can be individuated [29]. At long wavelengths, when the FSS periodicity D is much smaller than the operating wavelength λ , quasi-static regime, the periodic surface can be efficiently analyzed by using homogenized theory. In the intermediate frequency range, where the FSS periodicity is smaller but comparable with the operating wavelength, the periodic surface becomes resonant since the element composing the FSS screen starts to resonate. In this region the FSS can still be modeled by using the circuit theory but the values of the lumped parameters need to be retrieved by using a full-wave simulation followed by an inversion procedure. The last region, where the periodicity becomes larger than the guided wavelength λ_g , is the most non-linear and FSS elements (also single resonant ones) need to be represented by using a multi-mode network. The three regions are summarized in Fig. 5.

An almost infinite set of geometries can be designed as unit cell of a periodic screen. Some of these geometries are more popular than others and are also simple to understand and to control. It can be demonstrated that the expression of the FSS reactance satisfies the Foster theorem, that is, it possesses the same pole-zero analytic properties as a passive LC network. The

number of lumped elements is directly proportional to the number of resonances. For simple non-resonant elements as wire grids or patch arrays, the impedance is mainly inductive or capacitive, respectively. When a resonant element (e.g. loop or cross or others) is employed in place of a purely capacitive or inductive one, a simple LC circuit can be used to fit the frequency response of an FSS. The circuit will be series for capacitive frequency selective surface whereas a shunt LC connection replaces the LC series for an inductive FSS. In absence of losses, the metasurface impedance is purely imaginary and it is represented by two lumped parameters. Losses can be introduced by adding a series resistance in the equivalent circuit [30]. A summary of the circuit models for some simple FSS elements is reported in Fig. 6.

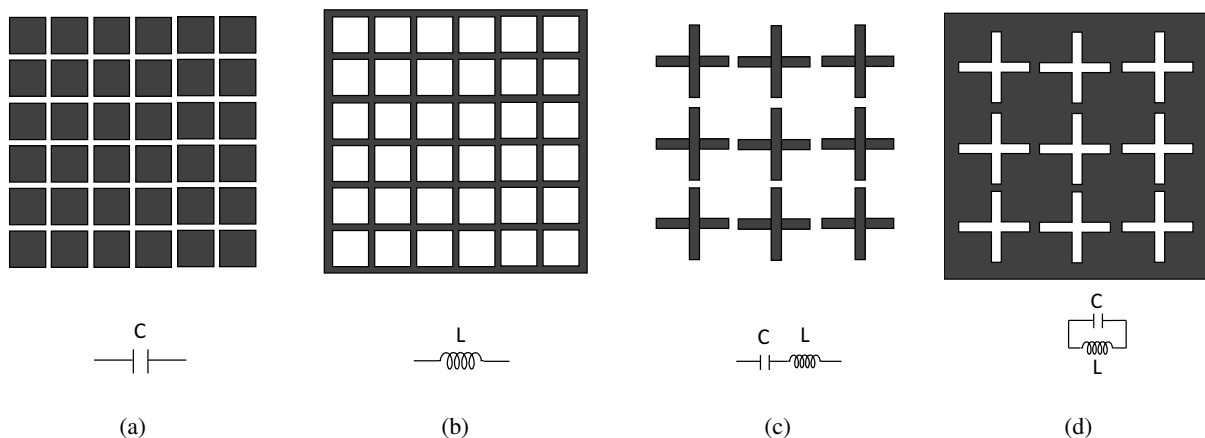


Fig. 6: Typical FSS elements and their circuit model representation. (a) capacitive patch, (b) inductive grid, (c) capacitive cross, (d) inductive cross.

We introduce in Table I a classification of the most popular geometries on the basis of resonant properties and equivalent circuits.

TABLE I: FSS elements classification and circuit model topology.

Element type	Element shape	Equivalent circuit
Non-resonant elements	Strip, patch, wire grid	C
Single resonant	loop, dipole, cross, tripole, dogbone	(LC)
Double-resonant	double cross, cross frame, double loop, Jerusalem cross, etc.	(LC)//(LC) or (LC)(L//C)
Multi-resonant	Concentric loops, fractal elements, quadrifilar spiral, meandered dipole	(LC)//(LC)// (LC)...
Other	split ring, cut loop, genetically optimized	-

A. Quasistatic Region

The calculation of the inductance or the capacitance value can be accomplished by averaging the currents flowing on the periodic structure [5]. The derived FSS impedance is of the second order since it is angle dependent and it has a different expression for the TE and the TM polarization. In the case of a patch array the impedance, $Z_{patch}^{TE/TM} = 1/(j\omega C_{patch})$, is just a capacitor:

$$C_{patch}^{TE} = \frac{D\varepsilon_0(\varepsilon_{r1} + \varepsilon_{r2})}{\pi} \ln\left(\frac{1}{\sin\left(\frac{\pi w}{2D}\right)}\right) \left(1 - \frac{k_0^2 \sin^2(\vartheta)}{k_{eff}^2}\right)$$

$$C_{patch}^{TM} = \frac{D\varepsilon_0(\varepsilon_{r1} + \varepsilon_{r2})}{\pi} \ln\left(\frac{1}{\sin\left(\frac{\pi w}{2D}\right)}\right)$$
(19)

while for grids, the impedance, $Z_{grid}^{TE/TM} = j\omega L_{grid}$, is an inductor:

$$L_{grid}^{TE} = \frac{D\mu_0}{2\pi} \ln\left(\frac{1}{\sin\left(\frac{\pi w}{2D}\right)}\right)$$

$$L_{grid}^{TM} = \frac{D\mu_0}{2\pi} \ln\left(\frac{1}{\sin\left(\frac{\pi w}{2D}\right)}\right) \left(1 - \frac{k_0^2 \sin^2(\vartheta)}{k_{eff}^2}\right)$$
(20)

where D represents the periodicity of the FSS, w is the gap between the squares patches and ε_{r1} and ε_{r2} are the relative dielectric permittivity of the dielectric slabs surrounding the periodic surface (typically the upper dielectric is air). k_0 is the wave number in free space, $k_{eff} = k_0\sqrt{(\varepsilon_{r1} + \varepsilon_{r2})/2}$ is the wave number of the incident wave vector in the effective host medium and θ is the incident angle. The agreement between the approximated and full-wave results is good if the FSS periodicity is smaller than half-wavelength. In [31] the formulas for an array of Jerusalem crosses are also given but they are sufficiently accurate only up to the first resonance of the Jcross.

B. Resonant region

In order to compute FSS reactance the knowledge of the current density on the FSS element is necessary even for the zero order approximation. Alternatively, a retrieving approach which starts from on the determination of the complex reflection coefficient through a preliminary full-wave

simulation can be employed [32]. Then, according to classical transmission line model reported in Fig. 7 , it is possible to obtain the impedance of the freestanding FSS as follows:

$$Z_{FSS} = -\frac{Z_0^2(1 + \Gamma_{in})}{2Z_0\Gamma_{in}} \quad (21)$$

where Γ_{in} is the reflection coefficient of the periodic structure calculated at the FSS position and Z_0 is the free space impedance. Once computed the FSS impedance, the L and C values have been computed starting from the calculation of the null of the FSS impedance. Once imposed the resonance condition $C = 1/\omega_0^2 L$, the inductance is obtained by an iterative procedure which minimizes the Euclidean distance between the MoM and the LC series impedance. If the frequency selective surface is embedded within dielectric layers, additional transmission lines representing the dielectric layers need to be considered in retrieving L and C parameters [32].

The equivalent circuit parameters are obtained for a particular FSS configuration but the FSS behavior depends on several degrees of freedom: periodicity, incidence angle, dielectric layers. The derivation of simple relations to generalize lumped parameters allows to use lumped capacitances and inductances, pre-emptively obtained at normal incidence and stored in a database of shapes, in an equivalent transmission line for computing the response of generic FSS configurations with no additional computation effort. Let us now briefly analyze separately the effect of these degree of freedom.

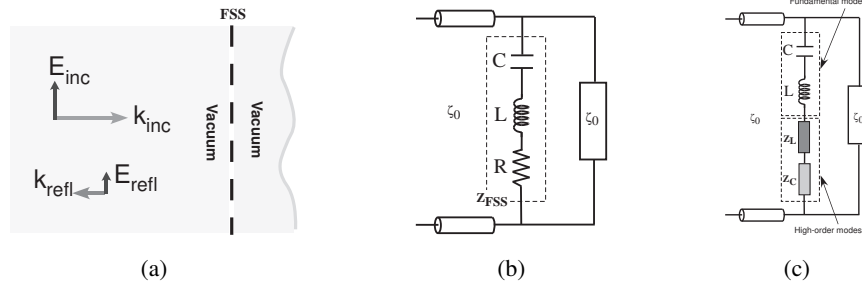


Fig. 7: (a) Freestanding FSS; transmission line model of the freestanding FSS with (b) single mode, and (c) multi-mode network representation.

1) *Cell periodicity*: If FSS element dimensions are simply rescaled with a certain scaling factor, a shift of the resonance frequencies is obtained. Starting from a given periodicity (e.g. 10 mm), the frequency behavior of the scaled FSS can be obtained by rescaling all the inductance and capacitance values. Clearly this stretch of the unit cell leads to the modification of the

elements lengths as well. For this reason it is much more convenient to think FSS element dimensions not as an absolute value but referred to the element periodicity. The validity of the procedure will be shown in the final section.

2) *Dielectric effect:* When a frequency selective surface is printed on a dielectric substrate the equivalent impedance is modified proportionally to the dielectric permittivity and the thickness of the supporting dielectric. Fixing the relative permittivity of the substrate, the increase of its thickness leads to a gradual shift of the FSS resonance towards lower frequencies. The resonant frequency of an FSS in presence of a thick dielectric substrates on both sides is reduced by a factor equal to $\sqrt{\varepsilon_r}$ and by a factor $\sqrt{(\varepsilon_r + 1)/2}$ when the dielectric is present only on one side of the FSS [5].

Within quasi-static regime ($D \ll \lambda$), the influence of dielectric layers can be accounted with acceptable error by considering an effective permittivity independent of the dielectric thickness but the approximation is no further acceptable in the resonant zone of the FSS. The presence of thin dielectric substrates involves a relevant number of Floquet modes and, given the complexity of the problem, a closed formula based on the Green function cannot be obtained. A good solution can be the derivation of a simple interpolating formula which exactly matches the variation of the effective permittivity as a function of the dielectric thickness. Such simplified approach is useful both for understanding the physics of the problem and it is also a good mean for achieving a preliminary estimate of the response of the FSS filter printed on an arbitrary thin substrate. To this aim an expression that fits exactly the effective permittivity reads [32]:

$$\varepsilon_{eff} = \varepsilon_r^{av} + (\varepsilon_r^{av} - 1) e^{-Nx} \quad (22)$$

where $d = d_1 + d_2$ is the global thickness of the right and left substrates and $x = 10d/D$, $\varepsilon_r^{av} = (d_1\varepsilon_{r1} + d_2\varepsilon_{r2}) / (d_1 + d_2)$ and N is an exponential factor that takes into account the slope of the curve. This parameter can vary for different cell shapes depending on the unit cell filling factor [32].

3) *Incidence angle:* When an oblique wave strikes the FSS, the FSS impedance changes with respect to the incidence angle. For instance, the expressions derived for patch arrays by using the averaged approach [33] are angle dependent. These expressions include the first order tangential derivative and therefore are valid for normal and oblique incidence when the grid is reasonably homogeneous ($D < \lambda/2$). The dependence on ϕ can be neglected if the element is

symmetric. For more general shapes, the following statements are valid [32]. Loop shapes have a similar angular dependence as observed for patches. The thin cross elements are characterized by a limited angular dependence of the TE capacitance. The angular dependence of the TM capacitance can be neglected for capacitive elements.

4) *Anisotropic Metasurfaces*: The equivalent circuit representation of an anisotropic FSS cannot be calculated with the conventional approach [29] if off-diagonal terms of $\underline{\underline{Z}}$ are not zero. However, since a metasurface is a passive system, its impedance matrix can be diagonalized by using the spectral theorem [34], [35], through a rotation of an angle φ^{rot} . The diagonal terms of the rotated matrix on the crystal axes χ_1, χ_2 (Z_{χ_1} and Z_{χ_2}) are finally matched with simple LC networks. The circuit model representation of the anisotropic element can be used to analyse anisotropic FSSs with a generic azimuth angle by using a compact description of generic FSS elements with only five parameters: the lumped parameters of the LC network $L_{\chi_1}, C_{\chi_1}, L_{\chi_2}, C_{\chi_2}$ and the rotation angle φ^{rot} [35].

C. Multimode region

In general, when an electromagnetic wave impinges on an interface, the direction of the reflected and transmitted waves follows the Snell law [36]. However, when the interface is formed by a periodic surface with an inter-element distance exceeding one wavelength, interference phenomena due to the lattice lead scattered waves to be directed towards multiple directions known as diffraction orders or Floquet harmonics [28], [37], [38]. The propagation directions are solely determined by the geometry of the lattice on which unit cells of the periodic surface are disposed. In a one dimensional case, the non-specular directions of scattering can be computed according to basic theory of diffraction gratings [38]:

$$\theta_{scatt} = \sin^{-1} \left(\frac{n\lambda}{D} - \sin(\theta_{inc}) \right) \quad (23)$$

where n represents the harmonic number, D is the inter-element spacing, λ is the operating wavelength, and θ_{inc} is the angle of incidence. As an example, the direction of Floquet harmonics as a function of frequency, when $\theta_{inc} = 30^\circ$, is represented in Fig. 8. Similarly, the scattering angles can be derived for a bidimensional periodic array [39]. It is evident from the above relations that a certain number of higher order Floquet modes are in propagation when the FSS periodicity exceeds one wavelength. However, the degree of excitation of each Floquet harmonic

depends on the specific shape of the FSS unit cell. The total scattered field can be seen as a summation of the harmonic contributions [38]:

$$E^R(\theta, \phi) = E^i(\theta_i, \phi_i) \sum_{i=-\infty}^{+\infty} R_i e^{(j\bar{k}_i \cdot \bar{r})} \quad (24)$$

Where \bar{k}_i represents the wavevector of the i^{th} harmonic, \bar{r} is the propagation direction and R_i represent the reflection coefficient of a specific harmonic, namely towards a specific direction. The energy associated to a specific harmonic is related to the diffraction efficiency [38].

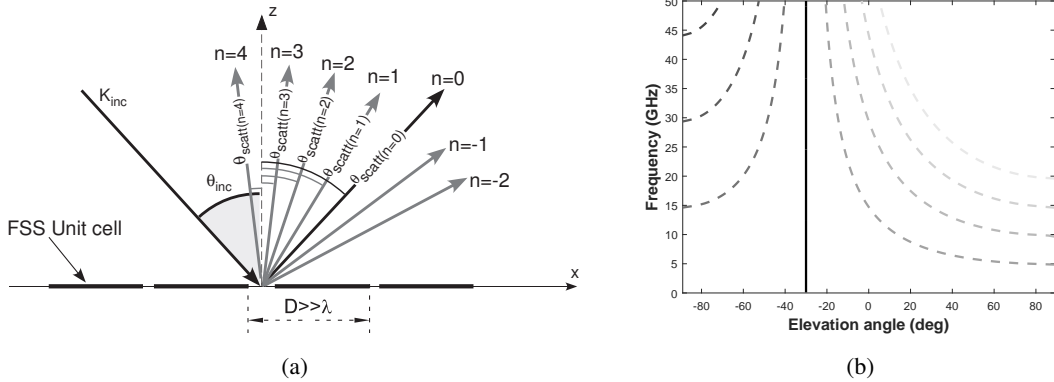


Fig. 8: (a) Representation of scattering directions for an artificial impedance surface with repetition period exceeding one wavelength. (b) Scattering angle/frequency plot of scattered Floquet harmonics for an incident angle of $\theta = 30^\circ$ and $\phi = 0^\circ$.

In order to analyze the behavior of frequency selective surface in the multimode frequency region, a number of additional elements are necessary in the circuit model. Indeed, for every harmonic in propagation, the contribution of the other harmonics has to be considered. For evaluating the reflection and transmission coefficient of the zero order harmonic, two additional impedances can be connected in series with the lumped circuit comprising inductances and capacitances to take into account the resonant phenomenon due to the lattice as shown in Fig. 7(c). The values of the excitation coefficients can be calculated after a run of a full-wave simulation in a sufficient number of frequency points [40]. The introduction of more high-order modes allow to describe also the highly non-linear frequency response of FSSs within the grating lobe zone. The multimode formulation holds for small sized elements which do not resonate in the analyzed frequency range since the current can be assumed as frequency independent.

VI. GENERALIZED SNELL'S LAW

The interaction of EM waves impinging on an interface between two media is regulated by the Snell's Law. Indeed, the reflection and refraction angles are determined by the the different refraction index of the two media according to he conservation of momentum along the tangential directions of the interface. On the other hand, it has been demonstrated that anomalous reflections and refraction are observed when a phase gradient between the two media is present. The phase discontinuity can be achieved employing a metallic patterning at the interface thus obtaining an artificial material with properties which can not be found in nature (metamaterial). The application of the Fermat's principle in the case of metamaterials led to a Generalized Snell's Law which is able to explain the anomalous reflections/refractions. In Fig. 9(a) the interface between two media with refraction index n_i and n_t is shown. The interface is characterized by a phase gradient along the x direction equal to $\frac{d\Phi}{dx}$.

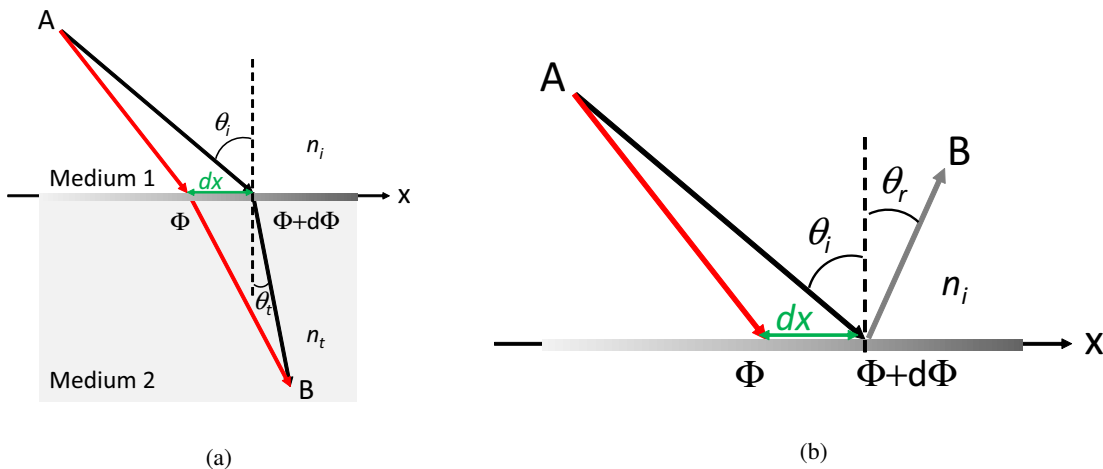


Fig. 9: Generalized Snell's Law: (a) refraction; (b) reflection.

The application of the Fermat's principle in the case of an EM traveling from A to B , leads to the following relation:

$$n_t \sin \theta_t - n_i \sin \theta_i = \frac{\lambda_0}{2\pi} \frac{d\Phi}{dx} \quad (25)$$

In this case, the angle θ_t is determined not only by the index n_i and n_t (classic Snell's law) but also by the phase gradient $\frac{d\Phi}{dx}$. The equation (25) is known as *Generalized Snell's law of refraction*.

Similarly, the application of the Fermat's principle in the case reported in Fig. 9(b), provides the *Generalized Snell's law of reflection*.

$$\sin \theta_r - \sin \theta_i = \frac{\lambda_0}{2\pi n_i} \frac{d\Phi}{dx} \quad (26)$$

In this case, the phase gradient affects the direction of the reflected wave (θ_r).

Metasurfaces have modified the classic Snell's law and allowed for new capabilities which could not be achieved with natural material. It is worth saying that the Generalized Snell's law is valid not only in the microwave band but also in the acoustic and in the optic regime (acoustic and optic metamaterials).

VII. ARTIFICIAL IMPEDANCE SURFACES (AIS)

Artificial Impedance surfaces (AIS) or High-Impedance Surfaces (HIS) are thin resonant cavities that fully reflect incident waves with a near zero degrees reflection phase within a limited frequency band [33], [41]–[43]. They are synthesized by printing a periodic frequency selective surface on the top of a grounded dielectric slab. Vias can be introduced to connect the FSS to the ground plane (mushroom structure) to block the propagation of TM surface waves [41], [42], [44]. For a normal incident plane wave the presence of vias is ineffective since electric field is orthogonal to the wire medium formed by the array of vias [12]. When a plane wave strikes the structure with angles off to the normal direction the presence of vias is relevant for the TM polarized waves [45]. The FSS can vary in shape but is essentially a two-dimensional (2-D) capacitive sheet formed by disconnected metal obstacles. The reflection phase of a AIS crosses zero at just one frequency where the surface behaves like a perfect magnetic conductor, which is complementary to a perfect electric conductor. In Fig. 10 a sketch of a AIS surface is illustrated. Since such peculiar property is valid only in a limited frequency range, the AIS surfaces are sometimes referred as Artificial Magnetic Conductors (AMC). The AMC behavior of the AIS structure results from the formation of a periodic set of small, parallel resonant LC circuits. The spacing between the edges of the elements controls the capacitance, and the magnetic flux created between the patches and the ground plane defines the inductance.

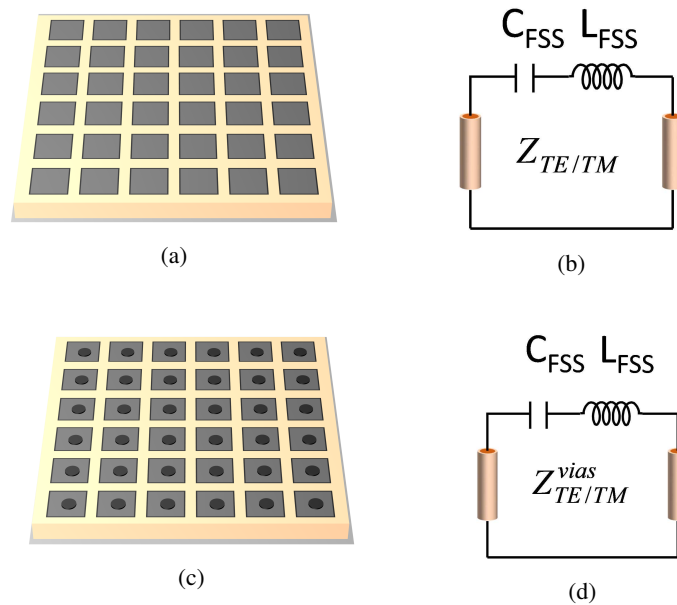


Fig. 10: (a) Artificial impedance surface without vias and (b) its circuit model.(c) High impedance surface with vias and (d) its circuit model.

It is therefore useful to state an operational percentage band of an AMC surface. Usually, the definition reads:

$$B_w\% = \frac{(f_{-90^\circ} - f_{+90^\circ})}{f_0} \times 100 \quad (27)$$

where f_{+90° is the frequency in correspondence of which the reflection coefficient phase assumes a value equal to $+90^\circ$; f_{-90° is the frequency where the phase is -90° and f_0 is the resonance frequency in correspondence of which the phase is zero.

The AMC behavior of the AIS structure results from the formation of a periodic set of small, parallel resonant LC circuits. The spacing between the edges of the elements controls the capacitance, and the magnetic flux created between the patches and the ground plane defines the inductance. The input impedance of the AIS structure is equal to the parallel connection between the FSS impedance Z_{FSS} and the surface impedance of the grounded dielectric slab Z_d :

$$Z_R = \frac{Z_d Z_{FSS}}{(Z_d + Z_{FSS})} \quad (28)$$

The impedance of a FSS can be represented through a series RLC circuit if the cell periodicity is lower than one wavelength. The capacitance of the FSS computed in freestanding configuration is valid if the dielectric is sufficiently thick in order to be able to neglect the high order Floquet harmonics [5]. The input impedance of the grounded dielectric slab can be computed analytically as follows:

$$Z_d = jZ_m^{TE, TM} \tan(k_z d) \quad (29)$$

where $Z_m^{TE} = (\omega\mu_r\mu_0)/k_z$; $Z_m^{TM} = k_z/(\omega\varepsilon_r\varepsilon_0)$ are the characteristic impedances of the slab for TE and TM polarization, $k_z = \sqrt{k^2 - k_t^2}$ is the propagation constant along the normal unit of the slab and $k_t = k_0 \sin(\theta)$ is the transverse wavenumber with θ representing the incidence angle of the incoming wave with respect to the normal.

When the vias that connect the metallic patches and the ground plane are introduced, the input impedance of the grounded artificial substrate need to be modified for TM oblique polarized waves because of the presence of the wire medium [4], [46]. It can be characterized like a uniaxial medium with a tangent dielectric permittivity equal to the dielectric permittivity of the hosting medium and a normal dielectric permittivity computed according equations 1 and 2. The lattice constant a is equal to the FSS periodicity D , while k_z^{TM} is the normal wavevector and is defined as [45]:

$$k_z^{TM} = \sqrt{k_0^2 \varepsilon_t - \frac{\varepsilon_t}{\varepsilon_n} k_t^2} \quad (30)$$

where ε_n represents the normal component of the permittivity which, differently from an ordinary medium, differs from ε_t . The normal component of the relative permittivity of a wire medium equals zero in correspondence with the so-called plasma frequency and it is negative below this frequency. The grounded wire array, as well as its infinite counterpart, is strongly dispersive even in the low frequency range [11] but, when the metallic patches are accommodated above the wires, the current along the wires are almost constant and the spatial dispersion is suppressed [12], [13]. The suppression of the spatial dispersion in the wire array allows for the adoption of a local model to approximate the behavior of the grounded wire array for TM incident waves [13]. When the normal component of the permittivity becomes zero an additional AMC resonance is generated in the AIS structure. This can happen only for the TM polarized waves and only for oblique incidence. Indeed, at normal incidence, the transverse wavenumber

($k_t = k_0 \sin(\theta)$) is zero and the presence of the wire medium does not modify the reflection properties of the structure. The position of the resonance is determined by the radius of the vias and therefore can be shifted independently of the main AMC resonance. The typical behavior of the phase of the TM reflection coefficient of a AIS both for normal and oblique incidence is shown in Fig. 11 [12].

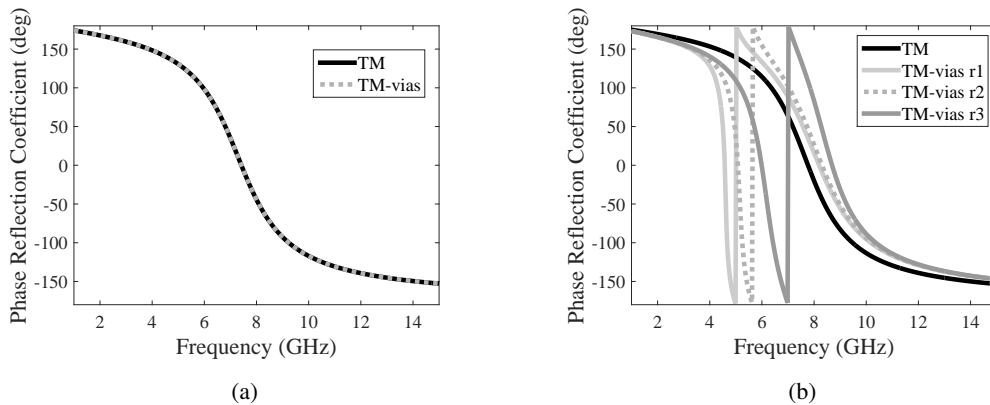


Fig. 11: (a) Typical phase reflection coefficient of a AIS structure at normal incidence with and without vias for a TM incident wave. (b) Reflection coefficient at oblique incidence for TM polarization without vias and in presence of vias with different radius ($r1 < r2 < r3$).

A. Surface waves on AIS

Surface waves are propagating electromagnetic waves that are bound to the interface between metal and free space [44], [47]. At microwave or radio frequencies, the electromagnetic fields extend many thousands of wavelengths into the surrounding space, and these waves are described more appropriately as surface currents. In the visible domain the surface waves supported are known as “surface plasmons” [48], [49]. They are TM polarized and propagate just below the speed of light, being cut-off at the surface plasma frequency. Close to this limiting frequency (typically in the ultraviolet), the mode becomes tightly bound to the interface with enhanced fields on resonance that decay exponentially into the media either side. However, for much lower frequencies, including the microwave spectrum, the dielectric constants of metals become large and imaginary causing such surface waves to propagate almost without attenuation at speeds close to the speed of light. In this regime, these loosely bound modes are often described as surface currents. Artificial impedance surfaces supports spoof surface plasmons at microwave

frequencies. A pictorial sketch of the electric field distribution in the vicinity of the interface is shown in Fig. 12.

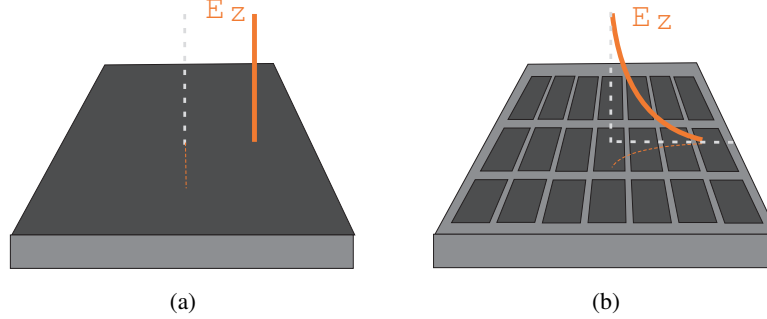


Fig. 12: (a) Schematic representation of electric fields associated with a mode propagating along the surface of a metal (a) and along a high-impedance surface (b) at microwave frequencies.

When the impedance of the AIS switches from inductive to capacitive the interface starts to support the propagating of TE surface waves.

The surface waves associated with a AIS structure, interpretable as a sheet with a certain surface impedance Z_s are the solution of the Helmholtz's equations for H_x (TM-modes) and E_x (TE-modes) at the impedance interface. The solution are the following propagation factors: [5]:

$$\beta_x^{TM} = k_0 \sqrt{1 - \left(\frac{Z_s^{TM}}{\eta_0}\right)^2}, \quad \alpha_x^{TM} = \frac{j\omega\mu_0}{Z_s^{TM}} \quad (31)$$

$$\beta_x^{TE} = k_0 \sqrt{1 - \left(\frac{\eta_0}{Z_s^{TE}}\right)^2}, \quad \alpha_z^{TE} = -j\omega\varepsilon_0 Z_s^{TE} \quad (32)$$

where η_0 and k_0 are the characteristic impedance and the wavenumber in free space, respectively. Propagating surface waves have a purely real propagation constant if the surface impedance is lossless. In this case the decay factor along z is purely real. The propagating waves, which are exponentially decaying with the increase of the distance from the surface have the following expressions:

$$\begin{aligned} TM \text{ waves} : H_y &= A e^{-j\beta^{TM}x - \alpha z} \\ TE \text{ waves} : E_y &= B e^{-j\beta^{TE}x - \alpha z} \end{aligned} \quad (33)$$

It is evident that only surfaces whose impedance has a positive imaginary part (inductive impedance) can support TM surfaces waves and only surfaces with negative reactance can support

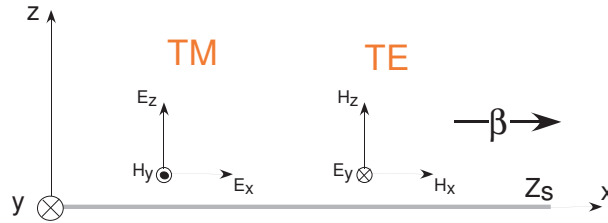


Fig. 13: Surface wave propagating along an impedance surface.

TE waves. For instance, the decay factor of TE waves on inductive surfaces becomes negative and the wave is not attenuated along z but it is a radiating leaky wave. The value of the impedance determines how much the field is confined to the interface. The fields of the TE and TM surface wave is reported in 13.

When the angle dependence of the AIS surface impedance is considered, the propagation constant of the surfaces waves cannot be extracted analytically since the surface impedance of the AIS depends itself on the propagation constant.

In this case the propagation constant is computed numerically by imposing the resonance condition at the interface between the air slab and the impedance surface:

$$\left(Z_{AIS}^{TE, TM}\right)^{-1} + \left(Z_0^{TE, TM}\right)^{-1} = 0 \quad (34)$$

where Z_0 is the free space impedance and Z_{AIS} is the surface impedance of the AIS computed as in the previous sections.

Surface waves appear in many situations involving antennas. If an antenna is placed near a metal sheet, such as a reflector or ground plane, it will radiate plane waves into free space, but it will also generate currents that propagate along the sheet [47]. In a finite in size ground plane these currents propagate until they reach an edge or corner. The result is a kind of multipath interference or “speckle,” which can be seen as ripples in the radiation pattern [41]. Moreover, if multiple antennas share the same ground plane, surface currents can cause unwanted mutual coupling. When the metallic vias are present in the artificial impedance surface, the propagation of surface waves is inhibited within a frequency band which is called *bandgap* of the AIS [41], [44]. The structure is not an electromagnetic band gap material in the traditional sense because it does not derive its surface wave suppression properties from destructive *Bragg scattering* between the waves and its periodic unit cell. In fact, it operates within frequency range where

the period is a small fraction of the free space wavelength. An example of the dispersion curves of the first TM and TE modes supported by an artificial impedance surface with and without vias are reported in Fig. 14. The dispersion curves are obtained by solving the dispersion equation in (34) derived according to the transmission line model of the structure. The plots are derived for an AIS surface comprising a patch array printed on a 1.52 mm thick dielectric substrate with a dielectric permittivity equal to 3. The patch array is characterized by a periodicity of 12 mm and a patch gap of 0.3 mm. The via radius is set to 1 mm. It is evident that the propagation of the first TE mode is allowed in both cases when the surface impedance of the AIS becomes capacitive (after the parallel resonance). The first TM mode is strongly influenced by the presence of vias which inhibit its propagation after the plasma resonance. The presence of the surface wave bandgap is obtained if the via radius is designed in such way that the stop frequency of the TM waves is located before the onset of the first TE surface wave mode, that is, after the parallel resonance of the high-impedance surface. The via radius affects the extension of the bandgap frequency region.

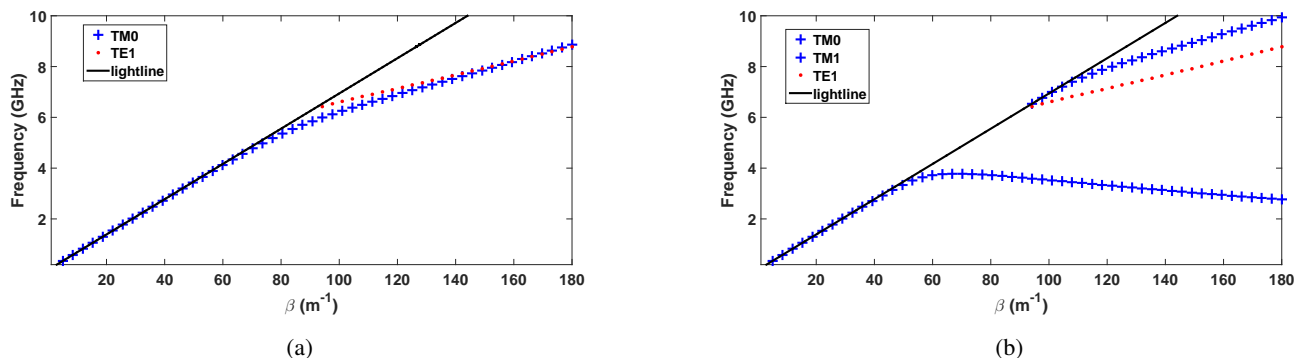


Fig. 14: Dispersion diagram of an Artificial Impedance Surface (a) with and (b) without vias. The AIS surface comprises a patch array printed on a 1.52 mm thick dielectric substrate with a dielectric permittivity equal to 3. The patch array is characterized by a periodicity of 12 mm and a patch gap of 0.3 mm. The via's radius is set to 1 mm.

VIII. TUNABLE METASURFACES

Several mechanisms have been investigated to make the a metasurface tunable. Some of the main mechanisms will be briefly introduced in this section:

- Diode loaded FSSs;

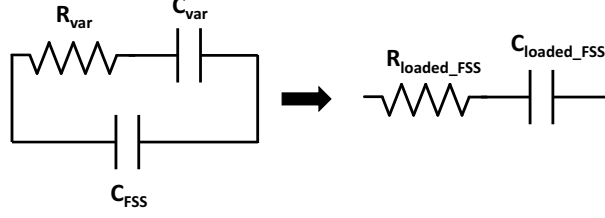


Fig. 15: Modelization of the patch array loaded with varactor diodes.

- Liquid crystal substrates;
- Conductivity change of the periodic patterns

A. Lumped loaded FSSs

By loading the frequency selective surfaces with varactor diodes or MEMS (Micro Electro-Mechanical Systems) on each unit cell, the distributed capacitance of the periodic surface can be dynamically controlled. If we represent the impedance of the capacitive patch array as a lumped capacitor ($Z_{patch}^{TE/TM} = 1/j\omega C_{patch}$), the connection of an active device can be represented with a lumped element impedance in parallel to the FSS impedance. The simplified equivalent circuit of the active capacitive FSS is shown in Fig. 15. The varactor diode is modelled as a series of a resistor R_{var} and a capacitor C_{var} . Assuming that the value of the resistor is small enough (below 10Ω) we can assume that the total capacitance of the FSS is:

$$C_{loaded_FSS} \approx C_{var} + C_{patch} \quad (35)$$

On the other hand, the new series resistance which represents losses has the following expression:

$$R_{loaded_FSS} \approx \frac{R_{var} C_{var}^2}{(C_{var} + C_{patch})^2} \quad (36)$$

If the capacitance of the varactor is of the same order of magnitude of the patch array capacitance, the effect of the diode resistor is equivalent to $R_{var}/4$.

1) *Liquid crystal substrates:* Liquid Crystal (LC) substrates may be used to dynamically control the resonant behavior of the absorber. Indeed, dielectric permittivity of the LC substrates can be varied by applying a DC, or a low frequency AC, bias voltage, that is, a torque necessary to rotate molecules from perpendicular (permittivity ϵ_{\perp}) to parallel orientation (permittivity ϵ_{\parallel}).

As a result, the permittivity of the tunable substrate varies between two values (biased state) and (0 V state) and therefore the dielectric anisotropy is given by:

$$\Delta\varepsilon = \varepsilon_{\parallel} - \varepsilon_{\perp} \quad (37)$$

The properties of some LC mixtures measured in the literature across different frequency ranges are summarized Table II. LC were initially employed to design tunable reflectarrays whose layout is geometrically similar to that of recently proposed tunable metamaterial absorbers. The difference is that the reflectarray aims to obtain a low loss reflection coefficient whereas the absorber is designed to minimize the reflection coefficient amplitude. By using one of the substrates reported in Table II, an example of LC tunable absorber can be designed. For simplicity, only the liquid crystal mixture is considered as substrate even if in practice the LC must be confined in a closed structure formed by other thin dielectrics. Since the permittivity variation between biased and unbiased states is quite limited the tunability of LC absorbers is much lower than that obtained with varactor loaded structures.

2) *Conductivity change of periodic patterns:* The variation of the surface resistance of the periodic patterns can be also used to modulate or tune the absorbing properties of the resonant HIS absorbers.

TABLE II: Properties of two liquid crystal mixtures obtained within two different frequency ranges.

Type of LC	Frequency [GHz]	ε_{\parallel} (biased)	ε_{\perp} (0V)
MERCK K15 LC	5	2.9-j0.087	2.7-j0.108
LC MDA 03-2838	35	3.1-j0.0124	2.3-j0.0253
MERCK BL037 LC	110-170	3.2-j0.064	2.8-j0.056
LC 5CB	2600	4	3.3

There exist some materials that are able to change their conductivity when a DC voltage is applied to them. Two popular materials are Indium Thin oxide (ITO) and Graphene. ITO is a heavily-doped n-type semiconductor with a large bandgap which makes it mostly transparent in the visible part of the spectrum [50]. Graphene is a zero-gap semiconductor formed by pure carbon in the form of a very thin (one atom thick) nearly transparent sheet [51]. ITO is used in a large variety of applications (e.g. liquid crystal displays, touch panels, solar cells) since it can be precisely etched into fine patterns [52] but it has some drawbacks including high cost due to

limited supply of indium, costly layer deposition, fragility and lack of flexibility [53]. Graphene allows dynamic control of both real and imaginary part of the conductivity when a DC voltage is applied. In microwave range graphene can guarantee a change of the real part of conductivity while in THz range also the imaginary part of the conductivity can be changed since plasma frequency of graphene is in THz range, which is much lower than noble metals. A change of the real part of conductivity can guarantee a absorption modulation while a dynamic control of the imaginary part can be efficiently used to achieve a tunable device. The main limitation of graphene is that the process of separating it from graphite requires technological development to be economical enough for industrial processes. This is the reason why today, graphene is not used in commercial applications. Graphene can be modeled by surface conductivity tensor which depends on several parameters as well as electrical and magnetic field bias [54]. Since graphene behaves as resistive material at microwave frequencies, it can be efficiently employed to time modulate the reflection properties of a FSS absorbers [55].

IX. ACOUSTIC METAMATERIALS

The intense research activity on electromagnetic metamaterials has stimulated the interest in developing acoustic metamaterials [56]–[64]. An acoustic metamaterial is a material designed to manipulate sound waves as these might occur in gases, liquids, and solids. Probably, the simplest approach to deal with acoustic metamaterials for electromagnetic engineers is to exploit the similarities between sound waves and electromagnetic waves. It is well known that there are mathematical similarities between the two problems, but the physical meaning of the quantities involved in the equations are very different. The major difference between sound waves and electromagnetic waves is that while sound waves require a medium to travel, electromagnetic waves do not. In electromagnetism, both electric and magnetic fields are transverse wave while acoustic waves are longitudinal waves. While electromagnetic waves are described by electric and magnetic fields, the physical parameters used to describe an acoustic wave are pressure and particle velocity. However, the two wave systems share the concepts of wavevector, wave impedance, and power flow. Moreover, in a two-dimensional (2D) case, when there is only one polarization mode, the electromagnetic wave has scalar wave formulation [36]. Therefore, the two sets of equations for acoustic and electromagnetic waves in isotropic media are dual of each other as shown in Table III. In Table IV the analogy between acoustic and transverse magnetic field in 2D under harmonic excitation is presented. From this equivalence, the desirable mass

density and compressibility need to be established by structured material to realize exotic sound wave properties.

TABLE III: Acoustic and electromagnetic equations.

Acoustic	Electromagnetism (TMz)
$\frac{\partial P}{\partial x} = -j\omega\rho_x v_x$	$\frac{\partial E_z}{\partial x} = -j\omega\mu_y H_y$
$\frac{\partial P}{\partial y} = -j\omega\rho_y v_y$	$\frac{\partial E_z}{\partial y} = j\omega\mu_x H_x$
$\frac{\partial v_x}{\partial x} + \frac{\partial v_y}{\partial y} = -j\omega\beta P$	$\frac{\partial H_y}{\partial x} - \frac{\partial H_x}{\partial y} = -j\omega\varepsilon_z E_z$

TABLE IV: Equivalence between acoustic and electromagnetic parameters.

Acoustic parameters	Electromagnetic parameters
<i>acoustic pressure</i> : P	<i>electric field</i> : $-E_z$
<i>velocity</i> : $-v_x, v_y$	<i>magnetic field</i> : H_x, H_y
<i>mass density</i> : ρ_x, ρ_y	<i>magnetic permeability</i> : μ_y, μ_x
<i>compressibility</i> : $\beta=1/B$	<i>dielectric permittivity</i> : ε_z

The control of sound waves is mostly accomplished through the control of the bulk modulus (or compressibility $\beta = 1/B$) and the mass density ρ . The bulk modulus B of a substance reflects the substance's resistance to uniform compression. It is defined in relation to the pressure increase needed to cause a given relative decrease in volume.

$$B = -\frac{P}{\Delta V/V_I} \quad (38)$$

where $\Delta V = V_F - V_I$. The significance of the negative sign in above equation is that when P is positive, then $V_F < V_I$ and ΔV is negative. The mass density of a material is defined as mass per unit volume:

$$\rho = \frac{m}{V} \quad (39)$$

The quantity is expressed in grams per cubic centimeter (g/cm^3). For acoustic materials and acoustic metamaterials, both bulk modulus and density are component parameters, which define their refractive index ($n^2 = \rho/\beta$). The differential equations in III can be combined to obtain the wave equation. The angular frequency is represented by ω and v is the propagation speed of acoustic signal through the homogeneous medium. In order to develop a propagating (plane) wave through the material, it is necessary for both ρ and B to be either positive or negative. In

electrical engineering, the quantity called impedance is the ratio of the driving force in a circuit, the voltage, to the rate at which charge passes by a point in the circuit, the current. Similarly, the acoustic impedance is the ratio of the driving force of an acoustic wave, the pressure, to the rate at which the particle in the medium pass a particular point, the velocity:

$$Z = \frac{P(x, t)}{v(x, t)} = \rho v \quad (40)$$

The macroscopic wave fields, either electromagnetic or acoustic wave, are averaged over the fluctuating local fields at individual atoms and molecules. Natural materials have both positive density and bulk modulus, but, negative values are mathematically possible and were experimentally demonstrated by using composite materials [56]–[58]. Composite materials extend the concept of natural material by replacing the molecules with man-made structures, viewed as “artificial atoms”. The spacing of the “artificial atoms” distinguishes metamaterials from phononic crystals.

Metamaterials are constructed using resonant subwavelength meta-atoms that enhance sound-matter interaction, it is possible to engineer the wave properties to obtain values of the effective acoustic-material parameters that are not observed in nature. One of the most unusual regimes for acoustic metamaterials arises when the real parts of the effective mass density and bulk modulus are negative in the same frequency range.

The first acoustic artificial metamaterial [65] used rubber-coated spheres to create locally resonant and deeply subwavelength structures that responded to incident acoustic waves. Materials with tailored parameters are attractive for applications such as steering of waves and super-resolution imaging. In particular, there has been a focus on negative parameters and imaging, which has led an initial surge in research into acoustic metamaterials [62]. Helmholtz resonators [66], closed cavities connected to a waveguide via a narrow channel, have been largely employed to design acoustic metamaterials. Attaching a series of open side-branches to the waveguide produces resonators with very low resonance frequency, and sound waves are entirely reflected up to the frequency at which the sign of the bulk modulus changes [62]. Loss and absorption can be limiting factors in metamaterial applications but it is actually desirable when the objective is to create metamaterials that maximize sound absorption [67], [68].

The quest to enhance wave–matter interactions and to manipulate waves using the smallest possible amount of space has led to the exploration of acoustic metasurfaces. Metasurfaces belong

to the family of wavefront-shaping devices with thicknesses much smaller than the wavelength. Metasurfaces are monolayer materials that are able to impart an arbitrary phase and amplitude modulation to the impinging wave, and constitute an alternative to bulky crystals. These surfaces are fabricated by using coiled elements, Helmholtz resonators or resonant membranes [69], [70].

Active acoustic metamaterials (externally biased) with unusual acoustic properties have been also considered in several designs. The most common elements used in active meta-atoms are active transducers, nano-electromechanical systems, piezoelectric materials and electrically loaded acoustic elements. These active devices have been successfully employed to synthesize acoustic diodes [71] and acoustic circulators [72].

Phononic crystals are a class of artificial materials with periodic structure on the same scale as the wavelength. Phononic crystals are artificial periodic composite materials consisting of periodically distributed acoustic functional scatter in a matrix with high impedance contrast of mass densities and/or elastic moduli, which can give rise to new acoustic dispersions and band structures due to the periodic Bragg scattering as well as localized Mie scatterings from the individuals [64]. One of the main properties of the phononic crystals is the possibility of having a phononic bandgap. A phononic crystal with phononic bandgap prevents phonons of selected ranges of frequencies from being transmitted through the material. To obtain the frequency band structure of a phononic crystal, Bloch theory is applied on a single unit cell in the reciprocal lattice space (Brillouin zone) [60].

X. APPLICATION EXAMPLES

Metamaterials and Metasurfaces can find application in several of practical scenarios including antennas, material design and sensors. We report some of the most interesting applications.

A. Cloaking

Electromagnetic cloaking is a technique that allows an electromagnetic wave to pass an obstacle unaltered, thus making the object invisible. The cloaking is carried out by means of structures that reduce the scattering of the waves impinging on an object. The ideal cloaking occurs when the object is hit by the EM wave and not any observer does not notice the presence of the object since he does not see alterations of the plane wave propagating in space. The concept of cloaking has its origins in the world of cinema.

What is today actually possible to do is the narrow-band concealment of an object, often of small size, in a rather limited band.

There exist different types of cloaking. Some of the most significant cloaking techniques proposed in the literature are the following:

- **Coordinate Transformation *cloak* (CT)** [73], [74]: The technique was proposed by Pendry, Shurig and Smith in 2006;
- **Hard and Soft Surfaces *cloak*** [75], [76]: The technique was proposed by Kildal, Kishk and Tengs in 1996;
- **Transmission line *cloak* (TL)** [77]: The technique was proposed by Alitalo, Luukkonen, Tretyakov in 2008;
- **Metal plate *cloak* (MP)** [78]: The technique was proposed by Alitalo, Luukkonen and Tretyakov in 2009;
- **Scattering cancellation *cloak*** [79]: The technique was proposed by Alù and Engheta in 2005;
- **Mantle *cloak*** [80]: The technique was proposed by Alù in 2011;
- **Carpet *cloak*** [81]: The technique was proposed by Li and Pendry in 2008;
- **Ray optics illusion** [82]: The technique was proposed by Chen et. al. in 2013.

Some of these techniques are limited because of strong dispersion which inevitably limits the bandwidth of cloaking and distorts the electromagnetic impulse traveling through the cloak. Some review works are available in the literature [83], [84]. The main aspects (both theoretical and practical) of the different cloaking techniques are summarized in the following sections.

1) *Coordinates transformation*: The cloaking technique based on the transformation of coordinates is perhaps one of the best known cloaking techniques in literature [73], [74]. The popularity derives from the fact that the technique has been perceived as the first approach aimed at obtaining invisibility. The technique involves the transformation of a point in the electromagnetic space into a sphere in the physical space, so as to create a spherical volume in which the electromagnetic fields are guided around this volume. The cover designed to conceal the object must satisfy complicated mathematical relationships:

$$\varepsilon_r = \mu_r = \frac{r - a}{r} \quad (41)$$

$$\varepsilon_\theta = \mu_\theta = \frac{r}{r - a} \quad (42)$$

$$\varepsilon_z = \mu_z = \left(\frac{b}{b-a} \right)^2 \frac{r-a}{r} \quad (43)$$

where a and b represent the internal and external radius of the cloak, respectively. To satisfy the aforementioned relations, it is necessary having anisotropic metamaterials lossless with both $\varepsilon_r < 1$ and $\mu_r < 1$. The main problem to be faced with this type of technique is that the wave travelling on the cloak must exceed the propagation speed outside. This implies that, if the wave propagates in the air, it must happen that $v > c$: and this represents a clear problem of the technique. A solution to this type of problem is to insert active elements into the cloak. This solution has as contraindication the fact of making the field unstable and therefore the need to use more complex materials. The advantage deriving from the use of this technique derives from the theoretical simplicity of realization. The limitation of this technique consists in the difficult realization of materials with properties such as to satisfy the demands of this type of cloak. The dimensions of the coat are also quite considerable compared to the object to be masked. The technique was experimentally demonstrated in 2006 with a microwave experiment [74].

2) *Hard/soft surfaces*: The technique is based on so-called hard and soft surfaces and was proposed in 1990 [85]. It consists in covering the object to be masked with a shell having a shape that extends along the direction of propagation of the wave. It is clear that the efficiency of the masking in a case of this type depends on the arrival angle of the electromagnetic wave: this happens because the masking surface is not symmetrical. Hard and soft surfaces can be represented as a PEC or PMC grid. In the case in which we want the reduction of the blockage to be effective both for the TE polarization and for the TM polarization, it is necessary that the surface behaves like a PEC for the TE polarization and as a slab with a dielectric cover of a quarter length wave for TM polarization. This effect can be obtained by adding metal strips on the dielectric surface in such a way that currents are supported in the same direction as the propagation direction of the electromagnetic wave. The size of the strip does not play a decisive role as long as there are at least 2 strips for each wavelength. The operating frequency is tuned by changing the thickness of the dielectric. The equivalent width for a metal cylinder can be reduced by making it rhombic with the sharpest angles possible in the direction of wave propagation. In fact, even the oblong shape with sharp edges works correctly with very large bandwidth. Unfortunately, in practice, the method is only applicable for thin objects, that is, with widths w of the order of a wavelength or less.

TABLE V: Comparison between coordinate transformation and hard/soft surface cloaking techniques.

Cloaking Method	Coordinate Transformation		Hard/Soft Surface	
Required Cross Section	Circular		Oblog	
Dimension of object	$2a \gg D$		$2a < D$	
Other Limitations	Thick; Metamaterial based; narrowband		Fixed angle of arrival	
	TE	TM	TE	TM
Material Requirements	Anisotropic ($\epsilon < 1$)	Anisotropic ($\mu < 1$)	PEC	PMC
Practical Implementation	-	Split ring resonator	Metal	Strips on grounded dielectric

3) *Coordinate transformation vs hard/soft surfaces*: The cloak proposed by Schurig et. al [74] is characterized by rotational symmetry and, unlike the configuration proposed by Kildal, can work for arbitrary angles of incidence in the horizontal plane. The concept of concealment in [74] is based on high frequency ray propagation and, for this reason, the mantle could also be applied to large objects provided that its thickness is equal to some wavelengths. The mantle proposed by Schurig must however be made up of anisotropic materials with permeability and permittivity that rapidly vary from zero to unity in the radial direction. This feature can only be achieved by using very narrow band metamaterials. Therefore, the apparent advantage of rotational symmetry may in fact be of little use as the inherent narrow-band properties of meta materials are very limiting. Furthermore, the Schurig blanket only works for TM polarization. Kildal's technique works on reasonably wide bands and it is characterized by a high implementation simplicity for both the TE and TM incident polarizations. The main advantages and disadvantages of the two techniques are summarized in Table V.

4) *Transmission line cloaking*: The technique called transmission line cloaking [77] is based on the use of structures made up of networks of transmission lines in which the electromagnetic field is propagated. To allow the electromagnetic field to propagate through the transmission lines, a transition metal surface is inserted with which the field is coupled and then sent to the transmission lines. Although the principle is very simple, to get the perfect cloaking in free space you encounter a big difficulty: the speed of the wave in the transmission lines must exceed that of the light and this turns out to be a problem because each branch of the transmission line sees the rest as a periodic load and then the wave is slowed down. In order to improve the method, it is possible to introduce periodic reactive loads in the network, but the structure is considerably complicated and there is also a considerable dispersion. It has therefore been shown that for

practical applications involving the use of broadband signals, it is preferable to use transmission lines without reactive loads, even if the propagation speed is not ideal. The more the cloak size increases, the more increases the amount of scattering. The merit of this type of technique is the ease of realization if the object to be masked has small dimensions, while it becomes a real problem if the object is very large.

5) *Metal plate cloaking*: This cloaking technique [56], [61] allows for the use of laminated metal plates with a hole in the central part where the object to be masked will be present. The height of the plates of this sort of circular waveguide decreases radially moving towards the inside of the structure and the electric field, orthogonally polarized with respect to the metal plates, travels in the guide around the masked region.

6) *Scattering cancellation*: The technique aims at minimizing the scattering of an object by covering the main scatterer with one or more layers of dielectric material, whose scattering is complementary to that of the object to be masked. [79], [86]. Supposing that $\varepsilon > \varepsilon_0$, it is evident that, in order to cancel the scattering, the cloak should have $\varepsilon < \varepsilon_0$ and an appropriate diameter. It has been shown that it is sufficient to cancel the dipolar mode (i.e. the fundamental mode) for sufficiently small scatters [87]. This technique requires the use of materials with $\varepsilon < 1$. These properties can be obtained only in the THz and optical range by using the so called plasmonic materials such as gold and silver. However, their use is limited by the high amount losses that can significantly vary as a function of frequency. When natural materials are not available, metamaterials have to be employed [86], [88].

7) *Mantle cloaking*: The mantle cloaking technique is also based on the scattering cancellation but in this the result is achieved using a different approach than the plasmonic cloaking. Instead of using a homogeneous isotropic materials, a frequency selective surface is used [28], [80]. By adapting the impedance of the mantle, it is possible to cancel the dominant dispersion from the object. The advantage of this method is that the thickness is ultra-thin and therefore the weight is very low. The mantle is typically composed of periodic elements of magnitude equal to a fraction of the wavelength. The diameter of the object is $\lambda_0/3$, and the surface is designed to provide the surface impedance required to cancel the dipolar contribution of the dispersion. The cover allows to obtain a scattering reduction of about 15 dB but on a narrow band of frequencies. It is however necessary to underline how the scattering cross section increases outside the operating band of the mantle [89]. The coat was also experimentally validated in 2009 in a freestanding configuration [90].

B. Electromagnetic Absorbers

Differently from cloaking techniques, that are designed to eliminate the backscattering of an object but also to produce restore the electric field distribution in the shadow region of an object, electromagnetic absorbers are engineered structures able to eliminate the backscattering of an object. Electromagnetic absorbers are much simpler structures than cloaking devices, do not require negative permittivity or permeability values and can operate over a large bandwidth. The use of electromagnetic absorbers is not restricted to RCS reduction applications [91], [92] but they find applications also for reducing harmful effects due to cavity resonance in enclosed monolithic microwave integrated circuits (MMIC) circuits [93], [94], mitigating the effect of apertures in metallic cavities [95] and attenuating surface waves [96], [97]. Avoiding multiple reflections is, for instance, strategic for achieving a correct reading in Radio Frequency Identification (RFID) [98]. Absorbers are also a fundamental building block in designing novel devices such as power imaging devices [99], photodetectors, microbolometers [100], [101] phase modulators [102] or frequency selective emitters [103]. Electromagnetic absorbers design is usually driven by the concept of impedance match to free space. When the absorber fulfills this condition, the impinging electromagnetic waves do not find any impedance discontinuity when they encounter the absorbing layer and thus electromagnetic energy is converted into heat. However, when absorbers are employed for damping cavity resonances or absorbing surface waves, the matching approach is not appropriate. In those scenarios, it is necessary to analyze and solve the dispersion equation trying to maximize, via the use of the most suitable absorbing layer, the attenuation factor of the supported mode [93]. Absorbing materials can be synthesized by carbon loaded cones but the most compact configurations comprises a multilayer of dielectric and magnetic substrates interleaved by tin sheet with a controlled surface impedance. A sketch of a general absorbing material and its transmission line equivalent are reported in Fig. 16. The most classical absorbing configuration is represented by the Salisbury screen which consists of a resistive sheet having a resistance of 377 ohm/sq located a quarter-wavelength out from a reflecting surface. The Jaumann absorber can be conceptually considered an extension of the Salisbury screen since it consists of two or more resistive sheets separated by a distance of approximately $\lambda/4$, thus providing a broadband response.

Absorbers comprising a single high-lossy layer in front of a ground plane are known as Dällenbach layer [104]. Several materials with different chemical properties can be employed for this design

but the final goal is to obtain that the imaginary portions of the electric permittivity and the magnetic permeability are adequately tuned to achieve the desired absorption. Frequency Selective Surfaces (FSSs), that are planar periodic arrays formed by the repetition of scatters with an arbitrary geometry, can also profitably be employed to design both narrowband and wideband electromagnetic absorbers. Narrowband absorbers can be synthesized having thickness much thinner than a quarter wavelength by exploiting the capacitive behavior of the FSS impedance. Ultra-narrow band configurations are also known as perfect metamaterial absorbers because of their very angularly stable absorption behavior at a single wavelength. Single layer employing resistive FSSs can be designed to achieve wideband absorption with a reduced thickness. This configuration, also known as Circuit Analog (CA) absorber, can be considered an extension of the Salisbury screen [105], [106]. Stacking an increasing number of capacitive FSS layers [107]–[109] is also a powerful method to improving absorbing performance of classical Jaumann configuration.

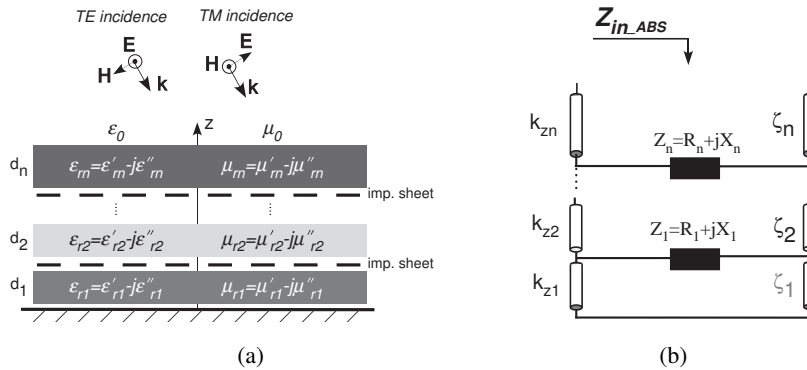


Fig. 16: (a) Layout of a general absorbing structure and its transmission line equivalent circuit (b). Salisbury screen, Jaumann screen, Dallenbach layer and Circuit analogue absorbers (CCA) and different FSS-based absorbers are particular cases of the represented stratified structure.

Electromagnetic absorbers can be efficiently analyzed by using the equivalent transmission-line (TL) method [110]. When a plane wave impinges upon the surface of the absorber, normally or obliquely, the amount of reflected power is determined by the mismatch between free space and absorber impedance. For absorbing surfaces backed by an impenetrable surface there is not transmitted energy and, as a consequence, the power that is not reflected, is dissipated in the

lossy structure. The magnitude of the reflection coefficient of generic absorbing surface reads:

$$|\Gamma^{TE, TM}| = \sqrt{\frac{\left(\operatorname{Re}\{Z_{in_ABS}^{TE, TM}\} - \zeta_0^{TE, TM}\right)^2 + \left(\operatorname{Im}\{Z_{in_ABS}^{TE, TM}\}\right)^2}{\left(\operatorname{Re}\{Z_{in_ABS}^{TE, TM}\} + \zeta_0^{TE, TM}\right)^2 + \left(\operatorname{Im}\{Z_{in_ABS}^{TE, TM}\}\right)^2}} \quad (44)$$

where Z_{in_ABS} and ζ_0 represent the input impedance of the absorbing structure and the characteristic impedance of free space for TE or TM polarization, respectively. For a lossless structure, the real part of the input impedance is null and the reflection coefficient magnitude always equals the unity. As lossy substrates or lossy surfaces are employed in the design, the real part of the input impedance Z_{in_ABS} decreases. The losses can be introduced in the dielectric substrate (dielectric losses) or in a surface (ohmic losses). The former is the case of the Dallenbach layer absorbers [111], [112] and the latter is the case of Salisbury, Jaumann or Circuit Analogue Absorbers (CCA) absorbers [28], [109], [113], [114]. In order to achieve a good absorption level at a single frequency or over a wide frequency band, it is necessary to create one or more resonances where the imaginary part of the input impedance is zero. At the same time, the real part should be matched to the free space impedance which is equal to $\zeta_0 \cos \theta$ and $\zeta_0 / \cos \theta$ for TE and TM polarization, respectively (θ represents the incident angle). In order to guarantee the perfect matching between the free space and the absorber medium, the following conditions should be fulfilled for the real and imaginary parts of the input impedance of the absorber [114]–[117]:

$$\begin{aligned} \operatorname{Re}\{Z_{in_ABS}\} &= \zeta_0^{TE, TM}; \\ \operatorname{Im}\{Z_{in_ABS}\} &= 0 \end{aligned} \quad (45)$$

The real part of the input impedance of the absorbing medium can be derived in a closed form [116]. By deriving an explicit expression of the real part of the input impedance of the artificial impedance surface, which is directly related to the amount of loss at the resonance, several properties of the AIS absorber having immediate practical implications can be easily extracted. The impedance of a frequency selective surface can be represented through a series LC circuit and a couple of resistors which take into account both dielectric and ohmic losses:

$$Z_{FSS} = R_0 + R_D + (1 - \omega^2 LC) / (j\omega C) \quad (46)$$

where C and L represent the capacitance and the inductance of the FSS. The capacitance of an FSS printed on a dielectric substrate is computed by multiplying the unloaded capacitor by the real part of the effective dielectric permittivity due the surrounding dielectrics. The capacitor formed between the adjacent elements has a loss component since the electric field lines are concentrated in a lossy medium. Such loss component is readily represented by the following series resistor [116]:

$$R_D \simeq \frac{-\varepsilon_r''}{\omega C (\varepsilon_r' + 1)} \quad (47)$$

The FSS series resistor R_D is inversely proportional to the FSS capacitance. The ohmic resistor connected in series with the aforementioned dielectric resistor can be evaluated by weighting the classical expression of the surface resistance valid for metals or resistive inks with the ratio between metalized area and periodicity of the unit cell [117]:

$$R_o \approx \frac{S}{A} \frac{1}{\sigma \delta} \quad \text{if } t < \delta, \quad R_o \approx \frac{S}{A} \frac{1}{\sigma t} \quad \text{if } t > \delta \quad (48)$$

where t , δ and σ represent the thickness, the skin-depth and the electrical conductivity of the metallic/resistive pattern, respectively. $S=D^2$, D is the cell periodicity and A is the surface area of the lossy element within a single unit cell. The relation (48) implies that the smaller is the scattering area, the smaller is the surface resistance leading to a certain fixed lumped resistance (same amount of loss). If the FSS is made of copper, ohmic losses obtained according to relation (48) are generally two orders of magnitude lower than the dielectric resistor (47). Conversely, if the metal is replaced with a resistive ink, the resistor assumes values higher than the dielectric resistor. Ohmic losses, which come from the currents flowing on an imperfect conductor, they are increasingly important as the working frequency raises. After some simple algebraic operations, the real part of the input impedance Z_{in_ABS} at the resonance is derived :

$$Re \{Z_{in_ABS}^{res}\} \simeq \frac{(Im \{Z_d\})^2}{(Re \{Z_d\} + R_O + R_D)} = \frac{\frac{\zeta_0^2}{\varepsilon_r} \left[tg^2 \left(k_0 d \sqrt{\varepsilon_r'} \right) \right]}{\left(\frac{D}{L} \right)^2 \frac{1}{\delta \sigma} + \frac{-2\varepsilon_r''}{\omega_0 C_0 (\varepsilon_r' + 1)^2}} \quad (49)$$

The expression in (49) contains all the degrees of freedom of the AIS absorber: FSS capacitance, of the electrical substrate thickness and of the real and imaginary part of the dielectric permittivity. where ω_0 is the first resonance frequency. $Re \{Z_d\}$, the real part of the input

impedance of a grounded substrate, has been neglected since it is usually much smaller than $Re\{Z_{FSS}\}$ at the main resonance of the AIS.

Depending of the prevalent nature of losses, different type of absorbers can be identified from relations (49):

- 1) $R_D \gg R_O$: Ohmic losses negligible with respect to dielectric losses. The loss component is determined by the substrate properties. The substrate thickness and the FSS element needs to be chosen in order to maximize the absorption at the desired frequency. The structure is typically *ultra-narrowband*.
- 2) $R_D \sim R_O$: Both ohmic and dielectric losses contribute to absorption at the resonance. The resistors' values are typically comparable in THz range because ohmic losses start to play a important role also in metallic resonant structures. They can assume comparable values also in the microwave range if low-loss substrates are employed. The structure is typically *ultra-narrowband/narrowband*.
- 3) $R_O \gg R_D$: Ohmic losses are predominant. It is typically the case of lossy frequency selective surfaces manufactured with resistive inks or loaded with lumped resistors. Ohmic losses due to metallic patterns are predominant also in optical range even if the structure is completely metallic. The structure is typically *narrowband, wideband or ultra-wideband*.

The difference between AIS absorbers made up of metallic or resistive FSSs are clarified through a numerical example. The chosen substrate is a commercial FR4. In the former case the dielectric resistor is much higher than the ohmic resistor while in the latter case the losses introduced in the periodic pattern make the ohmic resistor predominant. The use of metallic FSSs forces the choice of the substrate thickness for obtaining, according to relation (49), a value of the real part of the AIS input impedance close to the free space impedance at the resonance. The FSS element is the same in both cases but the periodicity of the metallic cross is slightly higher than the periodicity of the resistive cross in order to have absorption at the same frequency. Moreover, the substrate thickness chosen for perfect absorption in the case of metallic cross is 0.5 mm while the substrate thickness for the resistive cross case is 1.6 mm. The lower substrate thickness leads to an increase of the FSS capacitance due to the influence of high-order Floquet modes and as a consequence, to a slightly lower FSS dielectric resistor.

The synthesis of narrowband absorbers by employing the AIS surfaces can be achieved when the inductive input impedance of the grounded substrate and the capacitive FSS impedance have the same value but opposite signs and, at the same time, a suitable amount of losses are included

in the structure. The typical reflection performance of previously mentioned configurations are reported in Fig. 17a.

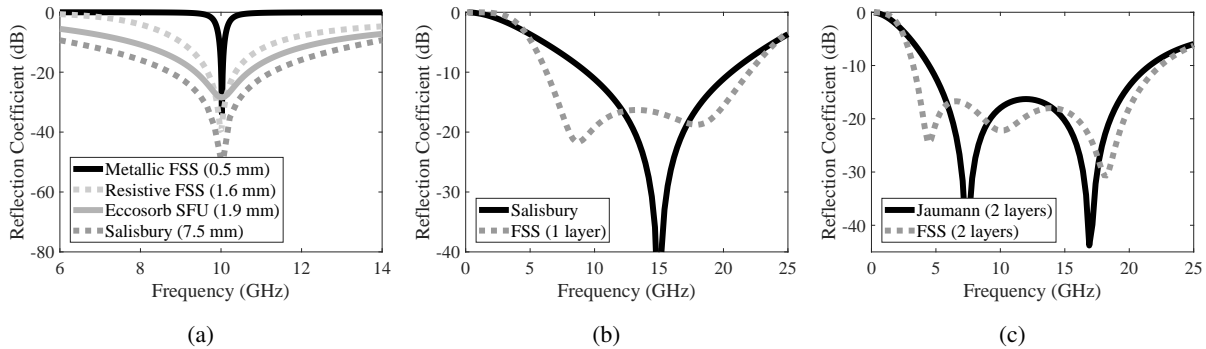


Fig. 17: (a) Reflection coefficient of four different narrowband absorbing configurations. Absorbers employing FSSs and magnetic loaded (Eccosorb) are thinner than a quarter wavelength. (b) Reflection coefficient of a 5 mm Salisbury screen compared with a 5 mm AIS absorber employing an array of resistive loops. (c) Reflection coefficient of a 12 mm Jaumann screen compared with a 12 mm Capacitive Circuit Absorber (CCA) employing an array of resistive patches. Parameters of Jaumann and CCA are the same: $d_1 = d_2 = d_3 = 4 \text{ mm}$, $\epsilon_{r1} = 1$; $\epsilon_{r2} = \epsilon_{r3} = 2$, $R_{s1} = 150 \Omega/sq.$, $R_{s2} = 500 \Omega/sq.$

Metamaterial absorbers employing metallic FSS can be made arbitrarily thin by presenting very good absorption performance at the resonant frequency. This absorption profile is also very stable with the incident angle. The absorption bandwidth is strongly dependent upon substrate thickness and magnetic permeability [118]. For this reason, magnetic loaded absorber (for instance Eccosorb SFU10) guarantees a large bandwidth with a small thickness. Salisbury is the most wideband among the reported configurations, but it is one of the thickest one since it resonates with a quarter-wavelength substrate.

If the AIS surface is suitably designed, an additional resonance can be introduced in order to drastically enlarge the operating bandwidth. The second resonance is obtained if the capacitive impedance of the grounded substrate (thicker than a quarter wavelength) will be equal to the inductive impedance of the FSS (after its proper resonance). At the center of the operating band the input impedance of the substrate tends to infinite and the FSS impedance can be designed to have a purely real impedance with zero imaginary part. The optimal surface resistance can be derived from the equivalent circuit model [114], [119].

If multiple FSS layers are stacked on top of each other with a configuration similar to the Jaumann absorber (uniform resistive sheets are replaced by the FSSs layers), ultra-wideband

absorbers can be also obtained. In the design of ultra-wideband absorber, the unit cell periodicity should be small enough to avoid the propagation of grating lobes (additional propagation directions [28]) at the highest absorption frequency. For this reason, sub-wavelength low-pass arrays are employed instead of the conventional resonating FSS elements [108], [109]. The low-pass arrays have capacitive impedance over the whole frequency band and, when they are made of resistive materials, they can be modeled by series RC circuits over the entire frequency band of interest. Capacitive circuit method is also powerful in the optimization of oblique incidence since patch arrays can be modeled accurately for different incident angles and polarizations [120].

Another important parameter in designing absorbers for oblique angle of incidence is to employ proper dielectric layers since they can provide scan compensation, bandwidth increase and frequency response stabilizations [107]. In order to understand the effect obtained by replacing the resistive sheets typical of Jaumann configuration with arrays of resistive patches, the impedance of both the Jaumann absorber and the capacitive circuit absorber (CCA) are analyzed. A simple dual layer structure is considered for simplicity. In order to compare the performance of Salisbury and Jaumann configurations with those employing periodic surfaces, the following structures are compared:

- 1) a $\lambda/4$ Salisbury screen with 5 mm air substrate is compared with an AIS absorber with the same thickness employing an array of resistive loops having a surface impedance of $70 \Omega/\text{sq}$;
- 2) a Jaumann screen composed by 3 dielectric substrates of 4 mm (total thickness of 12 mm) with two resistive sheets in between is compared with a capacitive circuit absorber having the same dielectric stack up. The only difference is that the uniform resistive sheets are replaced by two arrays of patches characterized by the same surface resistance.

The reflection coefficient achieved with the aforementioned configurations are reported in Fig. 17 b and c. It is apparent that the presence of the FSS layer helps in increasing the absorption without impacting the total thickness and leaving the stack up unaltered. The main objective in the design of an absorber is to get the largest possible bandwidth with the smallest thickness. Rozanov has shown that, for any metal-backed absorber, the infinite integral of the reflectance is bounded under certain conditions [118]. According to [118] the minimum thickness for achieving

a certain absorption profile R , is given by:

$$d \geq \frac{\left| \int_0^\infty \ln |R(\lambda)| d\lambda \right|}{\mu_r 2\pi^2} \quad (50)$$

where λ is the wavelength in free space and μ_r is the static permeability of the layer. The minimum possible thickness can be used as a parameter to judge the efficiency of a design method. Some of the above analyzed configurations are compared against the minimum theoretical thickness calculated according to (50). The integral in (50) is computed by considering the actual profiles shown in Fig. 17. The results are summarized in Table VI.

TABLE VI: Electrical and geometrical parameters of the analyzed wideband and ultra-wideband absorbing structures. The physical limit is computed according to eq. (50)

Configuration	A:Thickness [mm]	B: Rozanov Limit [mm]	Physical limit/ thickness (A/B*100)	Bandwidth [%] (-15 dB) $2(f_{max} - f_{min})/(f_{max} + f_{min})$
Salisbury	5	4.4	88	45.4
FSS (1 layer)	5	4.48	89.6	97.1
Jaumann (2 layers)	12	10.68	89	111.9
Capacitive FSS (2 layers)	12	11.05	92.1	140.2

C. Radomes and Low-RCS antennas

Under many circumstances, a radome cover is placed over the antenna that protects the radiating element from its physical environment (e.g., wind, rain, ice, sand, and ultraviolet rays). It protects the antenna's exposed parts with a sturdy, weatherproof material, typically fiberglass, which keeps debris or ice away from the antenna to prevent any serious damage or malfunctioning [121], [122]. Typically, the radome cover is designed in such way to present a minimal interaction with the enclosed antenna. In this optic, a thin dielectric cover represents a good solution. Other implementations consist of a half-wave thick monolithic dielectric layer or multilayered structure (sandwich radomes) where different dielectric layers are employed to achieve better electromagnetic and mechanical performance. However a radome cover can also play a crucial role both in transmission and in reception mode of the enclosed antenna if it is opportunely designed (Fig. 18). Advanced radome design involves the use of metasurfaces. In the transmitting mode the radome cover should be transparent to radio frequencies to minimally impact the antenna operation. However, the radome cover can also be used to improve the

performance of the enclosed antenna in particular when the beam steering is performed. This design approach requires to carefully analyze the effect of the radome-array interaction. This research trend usually takes the name of Wide Impedance Matching (WAIM). From a scattering point of view, the radome can be of crucial importance in reducing the antenna Radar Cross Section (RCS) [123]. To this purpose, the radome can be designed as a frequency selective filter to reflect back out of band signals. This solution, together with shaping can guarantee a reduction of the RCS of the antenna system. Generally, in-band RCS is dominated by the antenna itself, not by the radome, whereas far out of band, the RCS will be dominated by the shape and by the reflection properties of the radome. This approach can be classified as a fictitious RCS reduction technique since it is effective for monostatic interrogations and if no additional scatters are located in the close proximity of the antenna. More in general, an ideal low-RCS radome should transmit the in-band power and absorb the incoming out of band power. In this case the radome take the name of rasorber (Radome-Absorber). The rasorber usually guarantee a transmission band where the antenna operate and one or two absorption bands. Several designs have been proposed in the last couple of years by employing both 2D and 3D FSS.

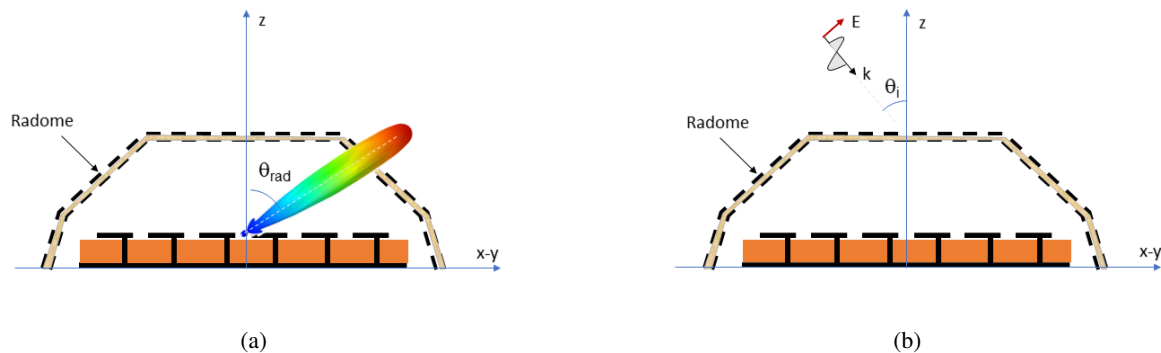


Fig. 18: (a) Transmitting mode. (b) Receiving mode.

1) *Wide Angle Impedance Matching (WAIM)*: The reflection coefficient of a phased-array antenna is subject to variation with the scan angle. This effect approaches a limit for a large planar array of many elements with periodic spacing [124]. Instead of designing the cover separately from the antenna, the can be optimized to enhance the performance in terms of electromagnetic and mechanical features of the radiating element. Multilayered dielectric structures or eventually periodic Frequency Selective Surfaces (FSS) can be employed to design and optimize the

performance of the antenna/radome system [125]. Several approaches have been proposed to analyze the effect of the radome-array interaction such as asymptotic or numerical methods [125]–[127]. Within this framework, also the optimization of the radome cover in presence of the radiating element is of great interest since a proper design could be a way for improving the performance. A generalized transmission-line model can be employed to design the metaradome, which is considered as a homogenized structure [125]. The periodic surface is characterized in terms of surface impedance with a full-wave simulation. A different strategy is based on a representation of the superstrate as a homogeneous anisotropic layer. In this case, the interaction of the radome with the array Generalized Scattering Matrix (GSM) is realized with a set of uncoupled transmission lines [127].

2) *Rasorbers*: In order to transform an antenna into a low-RCS structure, the radome cover should be absorbent when illuminated by out of band signals [128], [129].

The main requirements for a rasorber are the following ones: • Low in-band insertion loss both for transmitted and received signals. • Wideband absorption for out of band incoming signals. • Periodicity of the frequency selective surface lower than a wavelength at the upper frequency limit of the absorption band for avoiding grating lobes.

A possible design of the rasorber consists of a metallic pass-band frequency selective filter characterized by a wide reflection band and a resistive FSS on the other side. The stop band of the metallic FSS is used as a ground plane for an external absorbing structure [129]. Within the frequency range where the FSS behaves as a ground plane, the multilayer absorbs impinging signals as a wideband Artificial-impedance surface absorber described in section X-B).

3) *Low-RCS antennas*: If the radome cover is not employed on top of the antenna, the antenna design can be modified to transform the radiator in a low scattering structure. The RCS of an antenna is determined by an antenna component and by a structural term:

$$\sigma = \left| \sqrt{\sigma_s} - (1 - \Gamma_a) \sqrt{\sigma_a} e^{j\phi} \right|^2 \quad (51)$$

where σ is the total RCS of the target, σ_s is related to the field scattered by the short-circuited antenna, σ_a represents the field scattered by the antenna which involves the value of the port impedance, Γ_a is the antenna reflection coefficient and ϕ is the relative phase between the two terms. Antenna scattering plays a role in the antenna working bandwidth whereas it represents a minor contribution outside. The structural term σ_s is instead the most relevant contribution in

the array scattering. In all investigations, the main focus is on the reduction of the structural term of an antenna array analyzed under the short circuit condition of the feeding port.

The reduction of antenna RCS represents a challenging task for two reasons: i) antennas significantly contribute to the overall RCS of a structure and ii) its shape can be scarcely altered, and a not proper use of radar absorbing materials may degrade the overall radiation efficiency. Moreover, shaping is not so effective in the case of new bistatic radar systems [130] since the scattering energy could be collected also by an opportunistic receiver.

Electromagnetic absorbers have been efficiently employed for the reduction of the RCS of antennas [131], [132] over a narrow or wide frequency band. Several low-RCS types of antenna has been proposed in the literature: single element [133], array [91] and Fabry-Perot antennas [134], [135]. The proposed low-RCS configuration are usually obtained by including a resistive FSS within the antenna configuration with a minimal impact on the radiation performance. Another popular technique, consists including alternating AIS surfaces characterized by a 180° degree difference in order to cancel the back scattering [133]. However, this approach leads to a spreading of the energy towards other directions. For this reason, the claim of RCS reduction could not be adequate. The increase of the bistatic RCS is not a suitable RADAR countermeasure.

D. Wavefront modification through reflecting artificial surfaces

The tailoring of the wavefront through metasurfaces inspired several works on light bending [136], conversion of propagating wave in surface waves [137], flat lenses and axicons [138], transformation optics [139], [140], negative refraction [141], cloaking [142], [143].

Moreover, it is possible to exploit metasurfaces for the design of new types of reflector antennas. The incidence of a EM wave on a planar reflecting surface can be studied with the geometrical optic. In this case all the rays originated from the source impinge on the surfaces travelling along paths of different lengths and the phase delay accumulated by each ray depends on the length of each path. In this case, the reflecting phenomenon observes the classic Snell's law. On the other hand, the adoption of a metasurface as a reflecting mirror allows for the introduction of a phase discontinuity at the interface. The latter, if properly design, could tune the phase distribution at the interface thus focusing all the reflected ray in a particular direction. This is the working principle of metasurface-based antennas such as reflectarrays [144]–[146]. Another popular application of this engineering concept is in the field of communication theory

where the metasurfaces are employed to perform beamforming through Reflecting Intelligent Surfaces [147].

1) *Reflectarray antennas*: The reflectarray is a type of antenna that intends to imitate the parabolic reflectors using a planar array of elements located on a flat or slightly curved reflecting surface. The latter is designed to reflect incident wave coming from a feeder and collimate the beam along a desired direction [148]. This type of operation is conceptually similar to that which occurs in the case of a parabolic reflector which is able to form a plane wavefront in a particular direction. The radiating elements placed on the reflecting surface can be of different type: microstrip patches, dipoles, loops, rings. The spatial feeding of reflectarrays eliminates the complexity and losses resulting from the feeding network phased arrays.

The ability of the reflectarray to direct the beam in a particular direction comes from the design of the individual elements, located on the reflective surface, which reflect the incident field with the appropriate phases. The phase request to each individual element must compensate for the phase shift associated incident wave due to the different lengths of the route that goes from the feeder to each individual element of the reflectarray.

There are several methods to obtain from each radiating element of the reflectarray the desired phase. One possibility is to use identical microstrip patch or loops connected to stubs of variable length [146], [149]. Another possibility is to use patches [150] or dipoles of variable size. In the case of circular polarization is possible to use identical elements rotated by different angles [151].

In order to illustrate the working principle of a reflectarray antenna the geometry reported in Fig. 19 is considered. The reflecting surface of the reflectarray (metasurface) is composed by $M \times N$ discrete scatters spaced of $D = |\vec{r}_{mn}|$ each one characterized by its reflection coefficient $\Gamma^{m,n}$ and its radiation pattern $\cos^{q_e}(\theta)$. The scattering intensity of a chipless tag towards a generic direction \hat{u} is directly proportional to the physical area of the scattering object and it depends on the interference among all the point scattering contributions individuated in the object. The electric field scattered by the reflectarray is a summation of complex contributions given from each of the $M \times N$ discrete scatters. Consequently, the radiation pattern of the reflectarray in the generic direction \hat{u} can be computed similarly to an array antenna as follows:

$$\vec{E}^r(\hat{u}) = \sum_{m=1}^M \sum_{n=1}^N \cos^{q_e}(\theta) |\Gamma^{m,n}(\hat{u}, f)| e^{-jk(\vec{r}_{mn} \cdot \hat{u})} e^{-j(\angle \Gamma^{m,n}(\hat{u}, f))} \quad (52)$$

The argument of the exponential function takes into account the phase shift that experienced by the wave along the specific pointing direction \hat{u} . The terms $|\Gamma^{m,n}(\hat{u}, f)|$ and $e^{-j(\angle\Gamma^{m,n}(\hat{u}, f))}$ represent the reflection coefficient of the (m, n) – *th* discrete scatterer.

2) *Reflecting Intelligent Surfaces*: Reflecting Intelligent surfaces (RISs) have been recently proposed as a solution for 6G communication networks thanks to their capability to reflect and deviate the beams impinging into them by adjusting the biasing state of active components mounted on unit elements of the RIS. RIS technology is attractive from an energy consumption point of view since it is possible forwarding the incoming signal without employing any power amplifier like in MIMO arrays [152]–[154], but rather by suitably designing the phase shifts applied by each reflecting element in order to constructively combine the reflected signal. RIS can be also employed for physical information encoding in the so called massive backscatter wireless communication (MBWC) scheme [155]. RIS structures have the advantage of being easily integrable in the communication environment because of the easy deployment into buildings, ceilings of factories or into human clothing [156]. RISs can be tuned such that signals bouncing off a RIS are combined constructively to increase signal in the position of the intended receiver or destructively to avoid leaking signals to undesired receivers [157]. In the microwave regime, varactor or PIN diodes, whose EM characteristics (say, capacitances) can be dramatically tuned through varying applied voltages, can be incorporated within the surface. By independently controlling the voltages of each unit cell, phase/amplitude profiles can be accurately synthesized in order to shaping and controlling the reflected fields. Examples of varactor-controlled electrically steerable reflector in the microwave regime can be found since the early 2000s [158]–[160]. Alternative approaches to tune EM properties of metadevices rely on the free carrier doping in conductive materials with electrical gating and photoexcitation methods [147], [161]. Mechanical tuning offers another effective way to switch the EM properties of metadevices by reconfiguring the shape and surrounding environment of meta-atoms by the means of MEMS/NEMS, elastic substrate, or microfluidics [147], [161], [162]. By adequately changing the polarization state of the varactors, it is possible to perform the beamforming so that each user can be reached with the maximum available power. It has to be pointed out that the beamforming can be performed both in the near field of the surface (near field focusing) and in the far field synthesizing the classical far field beam directed toward the user. In order to focus a significant amount of the power towards the user, the RIS dimensions might be considerably large because the collected power is related to the physical area of the reflecting surface. Consequently, it is not uncommon that both

the transmitter and the receiver can be located in the near field of the surface [163]. Therefore it is of vital importance that the model of the surface is able to consider the specific incident and reflected angle for each unit cell [164], [165]. The vast majority of research works available to date rely on the assumption that metasurfaces act as perfect reflectors with a controlled phase reflection. Recently a fitting empirical model has been proposed for describing the behaviour of the RIS more physically [166]. However, the model is simply based on empirical functions which do not consider the effect of the physical parameters involved in the interaction between EM waves and RIS. The response of RIS to the radio waves depends on the geometrical and electrical properties of the designed surface, on the choice of substrates (low-loss materials lead to lower losses but the cost of the surface scales rapidly with the size), the characteristics of the tunable components, but also depends on the properties of the impinging EM wave such as angle of incidence, the angle of reflection [164], polarization [167]. Physics based models which take into account the aforementioned design parameters are therefore of crucial importance in order to avoid too optimistic performance predictions [165], [168], [169].

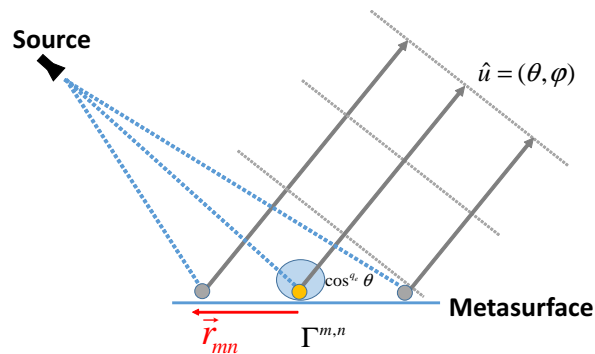


Fig. 19: Working principle of the wave front modification through an engineered surface.

E. Polarization Converters

The manipulation of the electromagnetic wave polarization state is a desirable characteristic in several electromagnetic applications. Common applications are related to microwave communications and antennas [170]. They are also used to perform remote environmental monitoring [171], or to realize microwave devices such as circulators and isolators [171]. Polarization converters are widely applied in optical instrumentation. Typically, they are realized with optical gratings and dichroic crystals [172]. A very effective way to manipulate several basic properties of the EM

(amplitude, phase, polarization) is to use metasurfaces. Recently, metasurface based polarization converters have been intensively studied because of the capability of manipulating the polarization of EM wave. Consequently, different types of polarization converters based on anisotropic and chiral metasurface have been proposed [173]–[175]. However, these polarization converters suffer from a narrow bandwidth which could be a limitation in their practical application. Many studies have been dedicated to exploring techniques for the expansion of the bandwidth. A possible approach is to stack periodic frequency selective surfaces in a multilayer configuration [176], in which complementary circular symmetric split-ring resonators are employed in a multilayer structure. Another approach is to generate multiple plasmon resonances by electric and magnetic resonances.

TABLE VII: Conditions on the uv - components of the reflection (Γ) and transmission (τ) coefficient in the case of reflecting and transmitting polarization converter.

Mode	Condition	Polarization
Transmission	$ \tau_u = \tau_v =1$; $\angle\tau_u - \angle\tau_v = \pi$	Linear
Transmission	$ \tau_u = \tau_v =1$; $\angle\Gamma_u - \angle\Gamma_u = \pi/2$	Circular
Reflection	$ \Gamma_u = \Gamma_v =1$; $\angle\Gamma_u - \angle\Gamma_v = \pi$	Linear
Reflection	$ \Gamma_u = \Gamma_v =1$; $\angle\Gamma_u - \angle\Gamma_v = \pi/2$	Circular

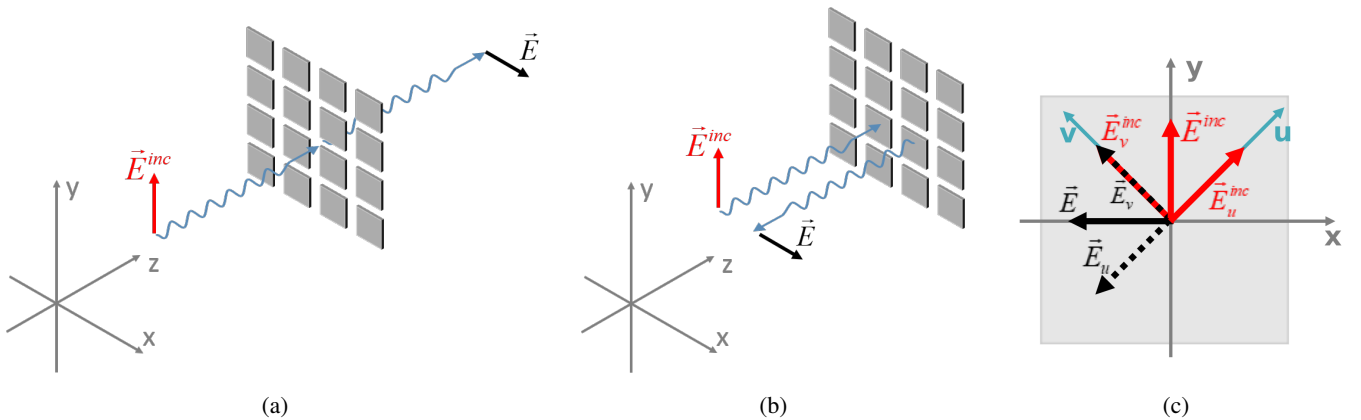


Fig. 20: (a) Transmitting and (b) reflecting polarization converter; (c) Incident and reflected electric field decomposed in the (u, v) -coordinate system;

The interaction mechanism of an EM wave impinging on an interface when the interface is formed of a periodic arrangement of metallic elements are regulated by general Snell's law

[177]. By opportunely designing the surface, it is possible to exploit the anomalous interaction of the EM wave with the interface in order to achieve non-conventional behavior of the reflecting surface. Both transmission or reflection polarization converters can be designed by imposing the conditions summarized in table VIII. In the case of linear polarization converter, the metasurface needs to reflect/transmit the two components of the impinging electric field with the same amplitude and with a phase difference equal to 180° . In Fig. 20a and b, the geometry of a reflective/transmission linear polarization converter is shown.

Let us suppose that an y -polarized wave impinges orthogonally on the bidimensional periodic surface. The working principle of the polarization converter can be explained by considering the additional coordinates system originated from the two perpendicular symmetric axes u and v , which are 45° rotated with respect to the y -axis shown in Fig. 20c. It is therefore possible to decompose the y -polarized field into u and v components and to write the incident electric field as follows.

$$\vec{E}^{inc} = E_0 \hat{y} = \vec{E}^{inc} \cdot \hat{u} + \vec{E}^{inc} \cdot \hat{v} = E_0 \sin\left(\frac{\pi}{4}\right) \hat{u} + E_0 \cos\left(\frac{\pi}{4}\right) \hat{v} \quad (53)$$

The reflected/transmitted electric field ($\vec{E}^{r/t}$) can be written as a function of the reflection/transmission coefficient in the uv -coordinates system:

$$\vec{E}^{r/t} = \vec{E}^{r/t} \cdot \hat{u} + \vec{E}^{r/t} \cdot \hat{v} = G_u \vec{E}^{inc} \cdot \hat{u} + G_v \vec{E}^{inc} \cdot \hat{v} \quad (54)$$

where G represents either the reflection R or the transmission T coefficients of the periodic surface. Consequently, $\vec{E}^{r/t}$ is parallel to the x -axis only if the following conditions are met:

$$G_u \vec{E}^{inc} \cdot \hat{u} = -\vec{E}^{inc} \cdot \hat{u} \Rightarrow G_u = -1 \quad (55)$$

$$G_v \vec{E}^{inc} \cdot \hat{v} = \vec{E}^{inc} \cdot \hat{v} \Rightarrow G_v = 1 \quad (56)$$

On the basis of the conditions (55) and (56), it is possible to deduce the characteristics required to the metasurface. First of all, because $G_u \neq G_v$, the metasurface has to be anisotropic [35]. In addition, because the magnitude of R_u and R_v need to be equal to 1, a dielectric substrate with a very low tangent loss is required.

The polarization converters are usually designed by employing more FSS layers in order to achieve the desired bandwidth performance. The most challenging task of a wide-band polarization converter design is to find the proper combination of thickness, number of layers,

substrate materials and unit cell topology of the metasurface, which meet the conditions (55) and (56) over a wide frequency range.

In case of multiple anisotropic layers, the reflected/transmitted electric field can be interpreted as a summation of infinite contributions of electric fields transmitted through the metasurface interface and reflected by next layer. At the interface air/metasurface, the y-polarized impinging field can be immediately reflected in cross-polarization by the metasurface but some of the signal penetrates the first layer and start bouncing between the following layers. The part of the signal which penetrates the first interface can have two polarizations state (x and y polarization). This signal can emerge in cross-polarization if suitable combinations of reflections exist. It is worth underlining that the total reflection/transmission of the composite surface can be written as a summation of terms of different orders. The number of terms needed to correctly estimate the backscattered field depends on the reflectivity/transmissivity of the multilayer surface.

A possible approach to optimize the performance of such devices is represented by genetic algorithm (GA) approach [178], [179]. The basic periodic cell is discretised in a 16x16 binary pixel matrix in which 1 or 0 represents whether a pixel is metallized or not. The GA selects the topology of the pixel matrix by minimizing the objective function which consists of the reflection coefficient of the fundamental Floquet harmonic over a number of frequency points within the desired frequency band. The goodness of the solution is evaluated by using the following fitness function calculated on $n_f = 21$ frequency points:

$$Fit = \sum_{n=1}^{n_f} |R_{xx}^i|^2 + |R_{yy}^i|^2 \quad (57)$$

where R_{xx} and R_{yy} represent the copolar reflection coefficients for x and y impinging electric field and n_f is the number of frequency points used for the optimization process. At the end of the optimization process, the unit cell topology can be cleaned from isolated pixels on which it is not possible to define a basis function.

The performance of some remarkable examples of reflective linear polarization converter presented in literature have been summarized in Table VIII. Reflecting polarization converters are usually an anisotropic FSS layer on top of a grounded substrate.

F. Antennas based on AIS surfaces

The possibility to make a conformal horizontal dipole radiate efficiently with the use of a Artificial Impedance Surface was introduced by Sievenpiper et al. in [41]. From 1999 onwards,

TABLE VIII: Comparison of the performance of ultra-wideband liner polarization converters.

Pol. Conv.	Thickness	Periodicity	f_{in}	f_{end}	Bandwidth	
	(mm)	(mm)	(GHz)	(GHz)	(GHz)	(%)
ref. [180]	3	4.6	8.49	32.84	24.35	117.8
ref. [181]	1.6	6.4	12.4	27.96	15.56	77.1
ref. [182]	3	11.5	7.57	20.46	12.89	91.2
ref. [183]	3	10	10	18.4	8.4	59.2

a large number of papers have been devoted to optimizing and modeling of antenna systems based on high-impedance surfaces(see, e.g., [47], [184], [185]. The most simple approach to analyze the radiative behavior of a dipole antenna on a AIS is to employ a simplified model in which the AIS is simply interpreted as a Perfect Magnetic Conductor (PMC) [184], [185]. These approaches typically uses the phase coefficient to explain the radiating mechanism of the antenna. However, first order homogenized techniques cannot guarantee a good approximation of the structure when they are applied to finite models [186]. The reason of these inaccuracies is due to the propagation of surface waves on the structure and their edge diffraction which leads to radiation pattern distortion and to additional resonance in the reflection coefficient of the antenna [47]. The influence of the backing plane dimension on the radiation properties of the antenna is therefore of crucial importance. In the TM (Transverse Magnetic) surface wave frequency range (before of the AIS resonance), the shape of the radiation patterns is only related to the size of the structure [187]. The presence of the FSS determines the AIS resonance and thus the antenna matching but it causes the onset of TE (Transverse Electric) surface waves after the AIS resonance. The occurrence of TE surface waves introduces additional resonances and deteriorates the radiation patterns but their effect can be kept out of the antenna operating band.

As shown in Fig. 21-b, the main resonance of the short dipole antenna placed above a grounded patch array radiates can be explained by a simple transmission line model where the capacitive impedance of the short dipole in free space is placed in parallel to the input impedance of the AIS structure. The parallel between the inductive impedance of the HIS and the capacitive impedance of the dipole generates, slightly before the HIS resonance, a parallel resonance in the antenna impedance which determines the matching. The impedance of the short dipole in free space and the impedance of the parallel connection between the antenna impedance and the HIS impedance is reported in Figure 22. This radiation mechanism would be the only useful one if

the high-impedance surface would be infinite.

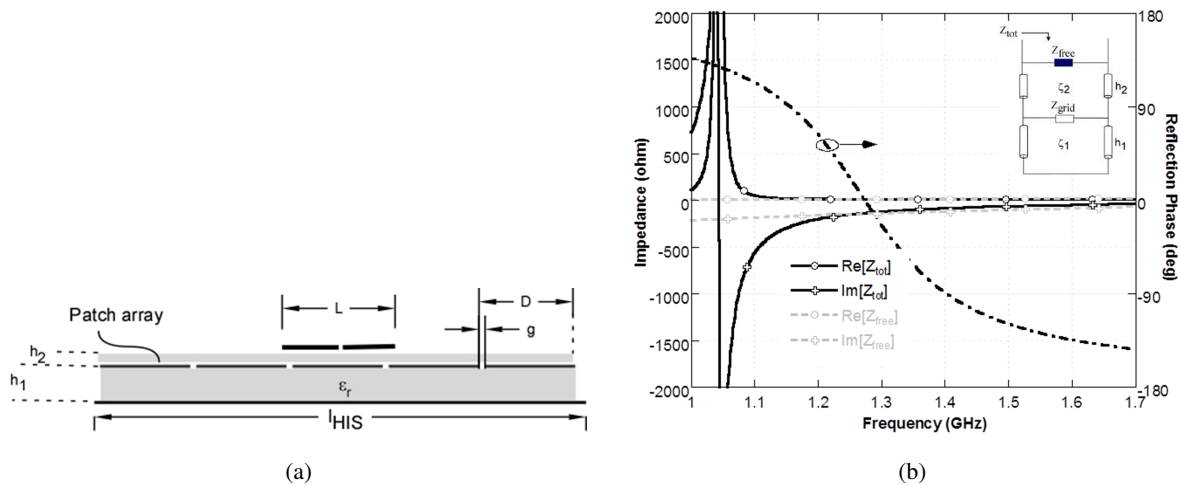


Fig. 21: (a) Layout of a low-profile antenna with a dipole antenna placed in the vicinity of an AIS. (b) Impedance and reflection phase of the AIS surface and impedance of the short dipole. Parallel impedance obtained by the simplified transmission line model of the short dipole on top of the AIS.

However, in a realistic configuration the size of the structure are inevitably finite and in practical designs the surface commonly contains only a few unit cells. In general, the effects of the finite-sized ground plane (distorted radiation pattern, backward radiation etc.) are considered harmful and a number of publications has been devoted to suppression of surface waves on antenna substrates. By considering the finite-sized AIS as a cavity, we can qualitatively determine the TE resonances as [47]:

$$\beta_{TE} l_{AIS} = p\pi \quad p = 1, 2, \dots \quad (58)$$

where β_{TE} represents the propagation constant of the first TE surface wave mode and l_{AIS} is the length of the cavity given by the number of unit cells multiplied by the cell periodicity D .

G. Leaky Antennas

Leaky-wave antennas (LWA) are a wide category of antennas which is increasingly popular because of appealing features as the possibility of realizing highly directive antennas without the need for complicated feeding networks typical of phased arrays. The theoretical foundation on which leaky antennas are based on dates back to fifties when complex mode theory started to be deeply investigated [188].

A leaky antenna is based on a monodimensional (1D) or two-dimensional (2D) guiding structure which gradually loose energy to surrounding space. 2D leaky-wave antennas can realize, at a given frequency, a directive pencil beam at broadside. In 1D case, the leaky wave can propagate a wave either unidirectionally or bidirectionally depending on the position of the source. The source can be positioned at one side or in the center of the guiding structure.

Supposing to have a 1D guiding structure extending towards x-direction (Fig. 22), the propagating wave will be characterized by a complex propagation constant $k_x = \beta - j\alpha$ in the antenna plane. If the antenna is 2D, the problem will be described in cylindrical coordinates [189]. The leakage factor α determines the radiated power per unit length. In order to obtain high directivity of a LW-antenna, a small value of α is required to efficiently illuminate a large aperture. The bandwidth of the antenna is directly proportional to leakage factor α , i.e. the lower is α , the higher is the peak gain but the narrower is the operating bandwidth. Indeed, when the leakage factor is lowered, the guided wave is released more slowly as a function of distance from the source. The propagation factor β must be smaller than the free space one ($\beta < k_0$). The leaky wave is a fast wave and the corresponding normal propagation constant is real. On the contrary, if the supported wave is slower than the one propagating in free space ($\beta > k_0$), the normal propagation constant k_z is purely imaginary, and the field decays exponentially away from the layer. The value of β determines the angle of radiation with respect to the normal direction, according to:

$$\theta_{rad} = \cos^{-1}(\beta/k_0) \quad (59)$$

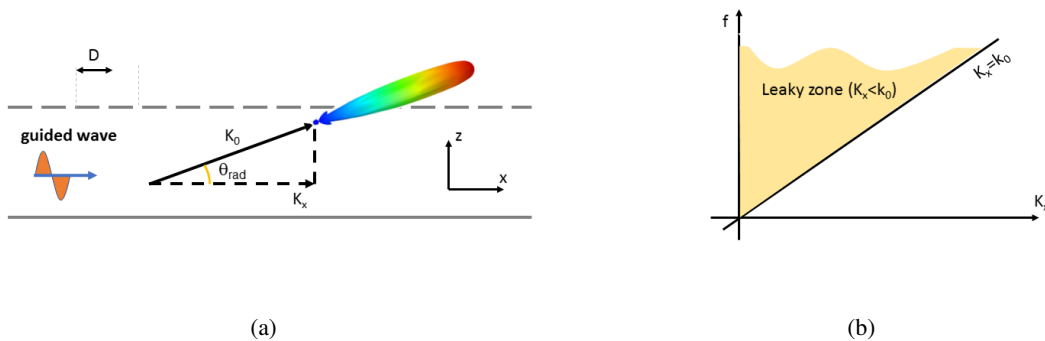


Fig. 22: (a) Leaky radiation from a guiding structure. (b) Dispersion diagram of the guiding structure.

In 2D case, the maximum broadside radiation is obtained when the phase and attenuation constants of the leaky mode are nearly equal [190]. If the radiating structure has cylindrical symmetry, the radiation pattern has a conical shape with the angle depending on the complex propagation constant [191].

One-dimensional LWAs can be broadly divided into three categories:

- uniform or quasi-uniform;
- periodic;
- holographic.

1) *Uniform/quasi-uniform*: A uniform LWA is one where the guiding structure is uniform along the length (taken here as the x-direction). In this case, the structure supports a wave that is fast with respect to free space, so that the complex wavenumber of the leaky mode k_x has a phase constant in the range $0 - k_0$. One-dimensional uniform leaky-wave antennas have a constant geometry along the length of the structure (although in some cases the antenna opening may be gradually tapered, as mentioned above). A typical example is the case of a rectangular waveguide with an open slit in the longitudinal direction. Another important category of leaky-wave antennas is represented by quasi-uniform structures, which are also characterized by a periodic modulation of their geometry. In this case, however, the fundamental mode is a fast wave, as in uniform structures, and the period is chosen to be small enough such that radiation comes only from the fundamental mode, and is not coupled to other space harmonics. An example of this leaky antennas are the Fabry-Perot antennas [192]–[194]. In general, quasi-uniform structures with sub wavelength period can be conveniently modeled with effective homogeneous material parameters or surface impedance concepts. Although in quasi-uniform leaky wave antennas the periodicity does not play a direct role in determining the radiation, since the fundamental mode is already a fast wave, the periodic modulation can be used to control the attenuation and phase constants of the leaky mode.

2) *Periodic*: A periodic LWA is one where the guiding structure supports a wave that is slow with respect to free space, so that $k_x > k_0$. Although the fundamental mode is a slow wave, it is possible to design the periodic structure such that one of the space harmonics (typically the $p=-1$) is fast and, thereby, it will radiate [195], [196]. The fundamental nonradiating mode is made to radiate by introducing periodicity along the length of the structure. The field on the structure is then characterized by an infinite number of space harmonics (also called Floquet

waves) having wavenumbers where p is the period in the x-direction.

$$k_{x-n} = k_x + 2n\pi/D_x \quad (60)$$

where D_x is the periodicity of the periodic surface in x-direction and n is an integer number representing the Floquet mode index. By using space harmonics introduced by the periodic surface, the normal propagation ($k_z = \sqrt{k_0^2 - k_{x-n}^2}$) constant can become real and thus the energy is radiated. One of the advantages of a periodic LWA is that a beam can be created in either the forward or backward directions, since k_{x-n} can be either positive or negative. In many realistic situations (e.g., periodically patterned microstrip lines), the periodic perturbation may also efficiently excite higher-order modes, and some of their space harmonics may significantly contribute to the overall antenna radiation.

3) *Holographic*: Holography is a method of imaging, in which three-dimensional images can be created resulting from electromagnetic-wave diffraction on specially patterned structures [197]. Holograms usually record the magnitude and/or phase of the interference pattern of two waves: the first one is the wave radiated or scattered by the object, while the second one is the reference wave similar to the one required for image recovery. A simple hologram can be made by superimposing two plane waves from the same light source on a holographic recording medium. The two waves interfere giving a straight line fringe pattern whose intensity varies sinusoidally across the medium. The spacing of the fringe pattern is determined by the angle between the two waves, and on the wavelength of the light. The recorded light pattern is a diffraction grating. When it is illuminated by only one of the waves used to create it, it can be shown that one of the diffracted waves emerges at the same angle as that at which the second wave was originally incident so that the second wave has been 'reconstructed'. Thus, the recorded light pattern is a holographic recording as defined above. First practical holograms in optics have been demonstrated in 1962 [198] after invention of lasers. Holographic theory has been exploited to design microwave antennas [199]. A source antenna produces the reference wave, and the desired radiation pattern corresponds to the image wave. The microwave hologram is a collection of scatterers arranged on the interference pattern produced by these two waves. Like the optical analogue, the microwave hologram scatters the reference wave to produce the image wave.

The range of operation of holographic antennas is such as the incident wave is dominated by a surface wave (SW) contribution. The same phenomenon can be also seen as due to a local modulation provided by the holographic surface of the SW wave-number that leads to a transformation from SW to leaky wave (LW). The excitation of leaky waves on holographic surfaces can be rigorously studied by using dispersion analysis. Sinusoidally modulated reactance surfaces (SMRS) have been used to generate LW, as described by Oliner and Hessel in 1959 [200]. They developed a comprehensive model of leaky waves on modulated impedance surfaces. This model describes how the propagation and radiation of leaky waves are controlled by the surface reactance, modulation depth, and period, and it serves as a foundation for the thin printed leaky wave antennas [201], [202].

The area of planar metamaterial dispersion engineering has been also recently referred to as metasurfing [203]. To design these types of antennas, it is essential to determine how to control the guiding and radiation characteristics of the constituent surface and leaky modes for each selected metasurface technology.

The patches are small compared to the wavelength of interest, so their scattering properties can be described in terms of their effective surface impedance. This permits the use of fast numerical methods that can analyze structures that are many wavelengths in size, without modeling the detailed structure of the material, which would render the problem impractically large [204]. By varying the geometry of the patches, one can control the surface impedance as a function of position. While the details of patches are much smaller than the wavelength and the modes supported by the metasurface are not radiating, the holographic modulation allows the excitation of high order Floquet modes in a similar fashion as it happens in the case of periodic type leaky antennas. An example of surface impedance as a function of the position in the metasurface is the following [204]:

$$Z_{\rho} = jX_0[1 + M_0 \sin(2\pi\rho/D - \phi)]; \quad (61)$$

where ρ and ϕ represent the radial coordinates of a specific metasurface position and D is the period of modulation.

H. Chipless RFID

Chipless RFID is a technology aimed at labelling object with completely passive labels. Conventional technologies to label objects are the optical barcode and the radio frequency

identification (RFID). The optical barcode has several advantages such as it being very cost effective, printable and consequently having a conformal shape. On the other end, RFID, which is much more recent technology, provides several improvements in respect to the optical barcode. Its read range is up to several meters and an RFID tag can be detected in a non-line-of-sight scenario. In addition, it is remotely writable and has smart functions such as sensing or cryptography. Moreover, it can have a very large coding capacity because a memory is embedded inside the chip. However, the unit cost of a RFID tag is significant in comparison to an optical barcode.

Chipless RFID can represent a tradeoff between these two technologies. It has advantages from both technologies, such as the high read range and the possibility to detect in a non-line-of-sight scenario. Furthermore, it can be potentially fabricated at a very low unit cost due to the fact that it is fully printable as there is no integrate circuit (IC). Finally, yet importantly, it can have sensing functionality.

The first chipless RFID device was developed by Leon Theremin who designed the first RFID tag in history [205]. The tag was an eavesdropping device that served as a spying microphone for many years. The operation principle of chipless RFID tags is based on the exploitation of the backscattering technique. When an antenna is illuminated by an RF signal, electric currents appear on its conducting parts. These currents create an electromagnetic wave that is re-radiated and it can be seen as a signal reflected by the antenna. Of course, this re-radiated signal depends on geometry of the antenna or the scatter. The physical parameter that characterizes this phenomenon is the Radar Cross Section (RCS).

The successful design of chipless tags requires the control and the optimization of the RCS of the considered structure [206]. The information is encoded in the field scattered by the tag when it is illuminated by the reader. The latter collects the echo and decodes the information. It is worth highlighting that the absence of the IC, determines some advantages but also some limitations in the chipless RFID technology. Firstly, the chipless tag is cheaper than the classic RFID because of a more cost effective manufacturing process. Moreover, the chipless RFID is potentially low power because there is no IC to activate. In addition, a chipless RFID tag can operate in harsh environment. Its robustness is a consequence of the absence of the IC. On the other hand, the chipless RFID tag is not reprogrammable and it exhibits a lower storage capacity with respect to the classic RFID. A more detailed overview of chipless and classic RFID feature is reported in Table IX.

On the basis of how the information is coded and consequently on the reading mechanism of

TABLE IX: Comparison of conventional RFID and Chipless RFID.

Classic RFID	Chipless RFID
Reprogrammable	Not reprogrammable
Radiated Power to activate chip	Potentially low-power (no chip to activate)
Expensive compared to optical bar code (not below 5cent)	Low cost
Single Frequency Operation	Wideband
Good bit storing capacitance	Low storage capacity
Operation in harsh environment	Robust to extreme environments

the data, chipless tags can be distinguished in two categories: time domain tag and frequency domain tag.

The frequency domain tags are the most promising ones since the TD tags allows the encoding of a very limited number of bits. FD tags can be further subdivided into other two categories: tags that work with a retransmission mechanism and those that work with a scattering mechanism. The latter can be realized with periodic [207] or with non-periodic surfaces [208], [209]. An overview of the chipless RFID classification is reported in Fig. 23. In the following section the time domain and frequency domain chipless tag are analysed more in detail.

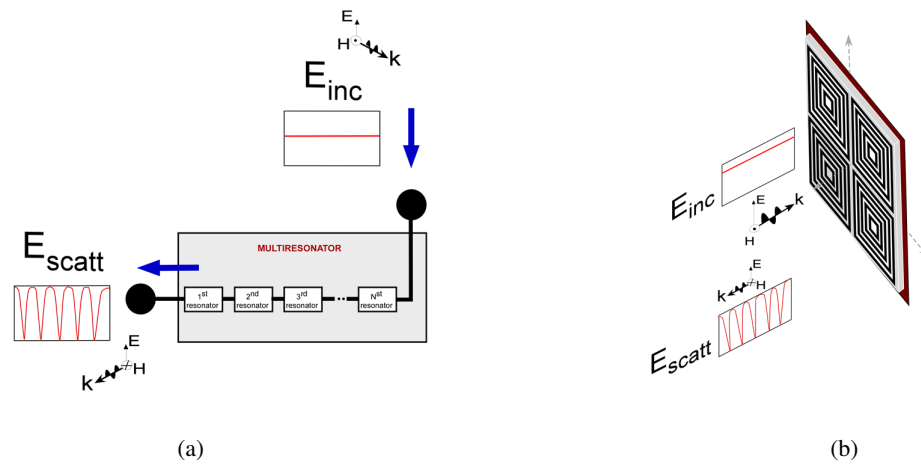


Fig. 23: (a) retransmission based tag. (b) scattering resonator tag.

The main advantage of using AIS based chipless RFID tag with respect to the non periodic tag is that the RCS can be controlled by choosing the number of unit cells (The RCS is proportional to the detection probability of the RFID system [210]). In the retransmission based chipless

RFID tag, a compact RF processing unit to encode and store the information in the tag structure is employed. Depending on the coding mechanism, different topologies of the processing unit are adopted. One common example is to use a set of filter cells to select specific frequencies that correspond to the tag code [211]. The ID code is stored in the processing unit which is composed by a series of cascaded resonators corresponding to a set of frequencies. One or more antennas are needed in order to obtain wireless communications.

In Table X, a summary of recently reported printed chipless RFID tags is presented. The table has been reported form [212].

When a chipless tag is placed on a metallic surface, its backscattered signal results to be very small with respect to the RCS of the metallic platform. The latter become stronger as the dimension of the metallic platform increase. Consequently, a drastic reduction of the read range occurs. A solution to overcome this problem is to embed the information in the crosspolar component of the scattered field of the tag. In [209], [213] has been demonstrated that by using this approach it is possible to distinguish the contribution of the chipless tag from the contribution of the metallic object. Consequently, it is possible to detect RFID tags even if the echo of the metallic platform tends to conceal the absorption peaks of the resonators. In light of these considerations, a polarization converter realized based on a FSS can be employed as a chipless RFID tag. The theoretical foundation of polarization conversion mechanism has been described in X-E section. The dipole on top of a ground plane acts as a perfect polarization converter at a single frequency. The dipole resonator is an good polarization converter for linear polarization when the azimuthal angle of the impinging wave is 45° [214], [215]. If multiple dipoles are employed, several frequency peaks are obtained [209]. A limitation of this solution is that the tag cannot be detected if the EM wave comes with a particular polarization state. Since in a real scenario the angle of incidence is unknown, the system performance are degraded or even compromised when the azimuthal incidence angle is different from the optimal one. The magnitude of the cross-polar reflection coefficient as a function of the polarization angle is shown in Fig. 24. A solution to this problem may be represented by a tag constituted by a combination of the two resonant dipoles. As reported in Fig. 24, the maximum crosspolar reflection coefficient is higher than -5dB for every azimuthal angle.

Chipless RFID is a novel technology, which has accumulated an increasing interest in recent years. Chipless RFID systems are still in their embryonic stage for real applications. Consequently, in order to enable this technology to be employed in commercial applications, many

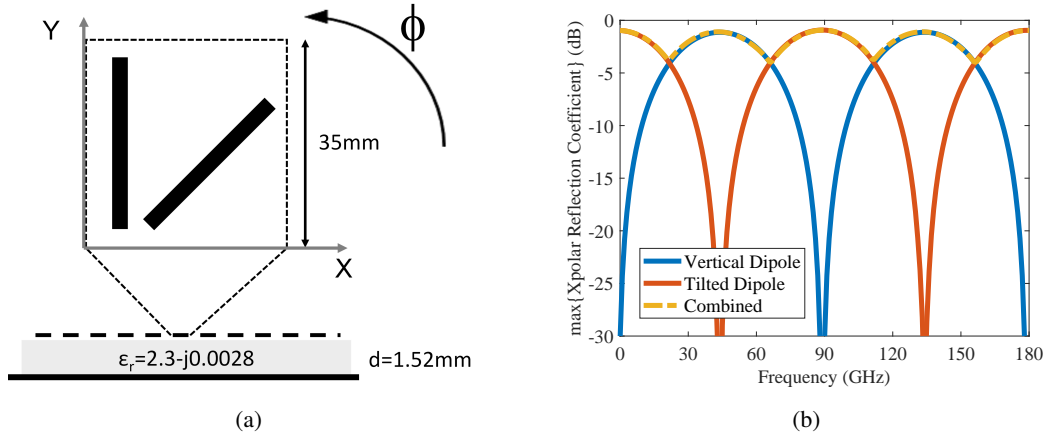


Fig. 24: Depolarizing chipless RFID configuration with angular insensitivity properties. (a) Stack-up and unit cell (b) and maximum of the amplitude of the crosspolar reflection coefficient as a function of the azimuthal angle.

limitations need to be overcome.

The main limitations of chipless RFID technology can be identified in the cost of the reader, the robustness of the reading, the limited read range and the tag reading speed. The information carried by the chipless tag is embedded in the EM signature of the tag. Because of the absence of the Integrated Circuit, the computational burden of the signal scattered by the tag is allocated to the reader. The majority of chipless RFID systems operate over a wide bandwidth. Indeed, several gigahertz of bandwidth are required to chipless RFID tags, which embed the information data in the frequency signature. Typically, these tags are read with UWB signals, which are generated with frequency sweeps and with narrow UWB RF pulses. The first approach employs wideband voltage controlled oscillators, which require a certain settling time to generate the frequency sweep. On the other hand, narrow UWB RF pulses require high-speed ADCs with a consequent increase of the cost of the reader.

In order to improve the detectability of the tag and also improving the immunity to multipath several detection approaches have been investigated. In particular, cross-polarization exploitation [209], [213] or signal processing techniques have been investigated [210]. Circular polarization has been also proved to improve the immunity of the tag response with respect to disturbs [216]. Even if several works have been dedicated to the improvement of the detection of chipless tags, a system level evaluation of the performance of these systems is not generally carried out. Usually, the considered Figure of Merits (FoMs) take into account the size of the tag (bit/cm^2) and the

TABLE X: FSS elements classification and circuit model topology [212].

Classes	Components	Operating frequency	Scal.	Size (cm ²)	Cod. Cap. (bits)
<i>Time Domain</i>	TL, capacitor [218], [219]	Various RFID bands	N	$\sim 4 \times 6$	8
	Dipole barcode [220]	5 – 6 GHz	Y	<i>N/A</i>	5
	Multiband RF barcode [221]	2.4 – 2.483 GHz	Y	<i>N/A</i>	5
		5.1 – 5.35 GHz			
		5.47 – 5.875 GHz			
	SRR array [222]	8 – 12GHz	Y	$\sim 8.6 \times 5.4$	4
	Coplanar strips [208]	2.5 – 7.5GHz	Y	4×2	22.9
Space filling curve [223]	3 – 4.5GHz	Y	<i>N/A</i>	3	
<i>Frequency Domain</i>	Single LC [224]	8.2 MHz	Y	4×4	1
	Spiral resonator [225]	3 – 7GHz	N	$\sim 8.8 \times 6.5$	35
	Elliptical dipole [226]	0 – 15GHz	N	<i>N/A</i>	3
	Complex impedance [227]	6.9 – 7.8GHz	N	0.17×0.43	4
	Patch antenna [228]	2.17, 2.33, 2.52GHz	N	12.5×5.5	3
	Dual polarized I slot [229]	6 – 13GHz	N	1.65×1.65	16

frequency compression of the peaks, but the system level performance in terms of Bit Error Rate (BER) [217] is often neglected.

These issues have been the main cause that has limited the employment of this technology in commercial applications. In a few years, with the progress of the studies, the above-mentioned problems will be solved thus resulting in a spreading of the chipless RFID technology in commercial applications with a consequent reduction of the manufacturing cost of the reader.

I. Metamaterial sensors and chipless wireless sensors

A sensing device is a structure able to convert a small change in a small amount of material in an electrical signal with a proper sensitivity. The sensors must have an operating frequency low enough to avoid the background and substrate absorption but this requirements tends to increase the sensor space which is not desirable [230]. The sensors features can be summarized in the following bullet list:

- small sensor layout while decreasing its operating frequency as much as possible;
- strong and measurable readout signal with a resonant behavior sharp enough to accurately track the shift in transmission spectra;
- linearity of sensing;

Metamaterials particles and resonators are well suited to design sensors since the main feature of metamaterial is their compactness with respect to the operating wavelength [7]. The simplest approach to design a metamaterial sensor is to adopt a transmission line loaded with a miniaturized metamaterial resonator. The operating principle of an EM metamaterial sensing device is reported in Fig. 25. The circuit will produce a sharp resonance in the transmission coefficient due to the presence of the metamaterial resonator. The material characterization is carried out by evaluating the frequency-shift of the resonant frequency. As a sample of unknown material (MUT) is accommodated on top of the resonator, the resonance position is moved as a function of the dielectric permittivity of the material. The variation can be linear or not depending on the shape and the thickness of the unknown sample. The relation between the frequency shift and the dielectric permittivity of the material can be explained by resorting to lumped circuit theory. Indeed, the metamaterial resonator can be roughly seen as a series LC circuit and the presence of the material will modify the capacitance of the circuit as a function of the effective permittivity of the surrounding medium. The surrounding medium is represented by the sample and the substrate of the metamaterial resonator. The effective permittivity can be computed as the average between the substrate permittivity and the MUT if their thickness exceed a certain value. Below this thickness, the effective permittivity is a function of the MUT thickness and thus the frequency shift of the resonance will be not linearly proportional with respect to the MUT permittivity [29], [231].

Moreover, metamaterial sensors can be transformed in a wireless sensor by connecting two monopole antennas at the end of the transmission line [225]. Another type of passive sensor is a chipless tag loaded with a multifunctional material [232]. This material can be in the form of small particle or can be a thin dielectric layer. The two configurations are shown in Fig. 25. In the former configuration, a substance which is sensitive to the desired environmental parameter is placed in the position of the designed resonator where the electric field is maximum in order to maximize the frequency response variation. In the latter case, the thin layer can be used as a superstrate or as a substrate of a resonator [233]. The variation of the properties of the small particle or of the thin layer leads to a resonance shift of the frequency response of the resonator [234]–[236].

REFERENCES

- [1] A. Sihvola, "Metamaterials in electromagnetics," *Metamaterials*, vol. 1, no. 1, pp. 2–11, Mar. 2007.

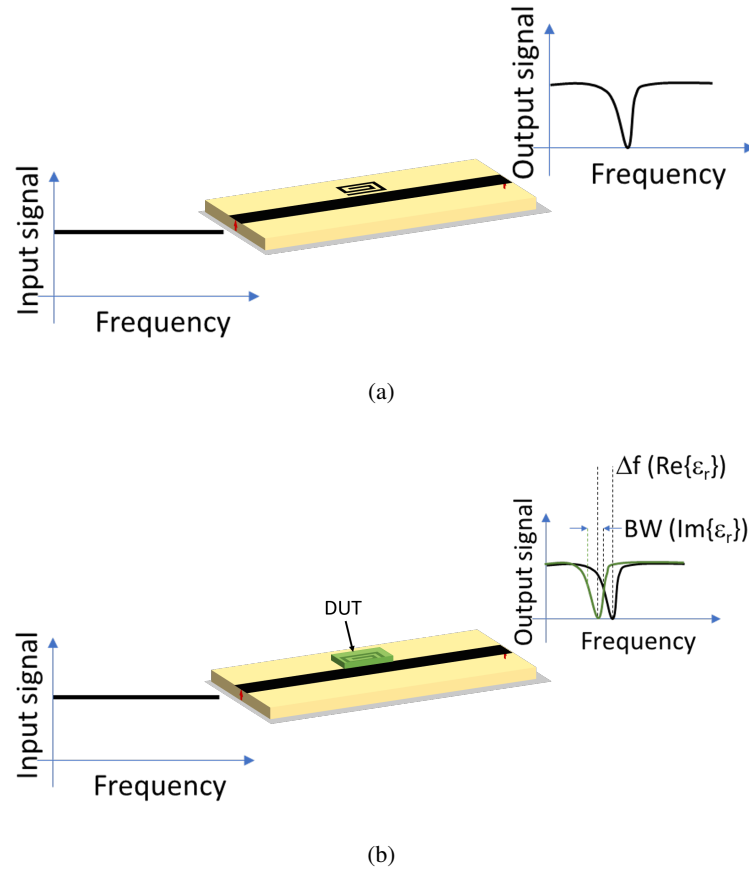


Fig. 25: Working principle of a metamaterial sensor (a) with and (b) without material loading.

- [2] V. G. Veselago, "The electrodynamics of substances with simultaneously negative values of ϵ and μ ," *Soviet Physics Uspekhi*, vol. 10, no. 4, p. 509, 1968.
- [3] D. R. Smith, W. J. Padilla, D. C. Vier, S. C. Nemat-Nasser, and S. Schultz, "Composite Medium with Simultaneously Negative Permeability and Permittivity," *Physical Review Letters*, vol. 84, no. 18, pp. 4184–4187, May 2000.
- [4] J. Brown, "Artificial dielectrics having refractive indices less than unity," *Proceedings of the IEE - Part IV: Institution Monographs*, vol. 100, no. 5, pp. 51–62, Oct. 1953.
- [5] S. Tretyakov, *Analytical Modeling in Applied Electromagnetics*. Artech House, 2003, google-Books-ID: MZ3tpGtadhC.
- [6] J. B. Pendry, A. J. Holden, D. J. Robbins, and W. Stewart, "Magnetism from conductors and enhanced nonlinear phenomena," *IEEE transactions on microwave theory and techniques*, vol. 47, no. 11, pp. 2075–2084, 1999.
- [7] S. A. Tretyakov, "A personal view on the origins and developments of the metamaterial concept," *Journal of Optics*, vol. 19, no. 1, p. 013002, 2017.
- [8] C. L. Holloway, A. Dienstfrey, E. F. Kuester, J. F. O'Hara, A. K. Azad, and A. J. Taylor, "A discussion on the interpretation and characterization of metafilms/metasurfaces: The two-dimensional equivalent of metamaterials," *Metamaterials*, vol. 3, no. 2, pp. 100–112, Oct. 2009.
- [9] C. Caloz, "Perspectives on em metamaterials," *Materials Today*, vol. 12, no. 3, pp. 12–20, 2009.
- [10] I. V. Lindell, A. Sihvola, S. Tretyakov, and A. Viitanen, "Electromagnetic waves in chiral and bi-isotropic media," 1994.

- [11] P. A. Belov, R. Marqués, S. I. Maslovski, I. S. Nefedov, M. Silveirinha, C. R. Simovski, and S. A. Tretyakov, “Strong spatial dispersion in wire media in the very large wavelength limit,” *Physical Review B*, vol. 67, no. 11, p. 113103, Mar. 2003.
- [12] O. Luukkonen, P. Alitalo, F. Costa, C. Simovski, A. Monorchio, and S. Tretyakov, “Experimental verification of the suppression of spatial dispersion in artificial plasma,” *Applied Physics Letters*, vol. 96, no. 8, p. 081501, Feb. 2010.
- [13] O. Luukkonen, M. G. Silveirinha, A. B. Yakovlev, C. R. Simovski, I. S. Nefedov, and S. A. Tretyakov, “Effects of Spatial Dispersion on Reflection From Mushroom-Type Artificial Impedance Surfaces,” *IEEE Transactions on Microwave Theory and Techniques*, vol. 57, no. 11, pp. 2692–2699, Nov. 2009.
- [14] C. R. Simovski, P. A. Belov, A. V. Atrashchenko, and Y. S. Kivshar, “Wire metamaterials: physics and applications,” *Advanced Materials*, vol. 24, no. 31, pp. 4229–4248, 2012.
- [15] A. Nicolson and G. Ross, “Measurement of the Intrinsic Properties of Materials by Time-Domain Techniques,” *IEEE Transactions on Instrumentation and Measurement*, vol. 19, no. 4, pp. 377–382, Nov. 1970.
- [16] A. Alù, “Restoring the physical meaning of metamaterial constitutive parameters,” *Physical Review B*, vol. 83, no. 8, p. 081102, 2011.
- [17] S. Arslanagić, T. V. Hansen, N. A. Mortensen, A. H. Gregersen, O. Sigmund, R. W. Ziolkowski, and O. Breinbjerg, “A Review of the Scattering-Parameter Extraction Method with Clarification of Ambiguity Issues in Relation to Metamaterial Homogenization,” *IEEE Antennas and Propagation Magazine*, vol. 55, no. 2, pp. 91–106, Apr. 2013.
- [18] X. Chen, T. M. Grzegorzczak, B.-I. Wu, J. Pacheco, and J. A. Kong, “Robust method to retrieve the constitutive effective parameters of metamaterials,” *Physical Review E*, vol. 70, no. 1, p. 016608, Jul. 2004.
- [19] T. Koschny, P. Markoš, D. R. Smith, and C. M. Soukoulis, “Resonant and antiresonant frequency dependence of the effective parameters of metamaterials,” *Physical Review E*, vol. 68, no. 6, p. 065602, Dec. 2003.
- [20] W. B. Weir, “Automatic measurement of complex dielectric constant and permeability at microwave frequencies,” *Proceedings of the IEEE*, vol. 62, no. 1, pp. 33–36, Jan. 1974.
- [21] F. Costa, M. Borgese, M. Degiorgi, and A. Monorchio, “Electromagnetic characterisation of materials by using transmission/reflection (t/r) devices,” *Electronics*, vol. 6, no. 4, p. 95, 2017.
- [22] O. Luukkonen, S. I. Maslovski, and S. Tretyakov, “A Stepwise Nicolson–Ross–Weir-Based Material Parameter Extraction Method,” *IEEE Antennas and Wireless Propagation Letters*, vol. 10, pp. 1295–1298, 2011.
- [23] A. Alù, “Restoring the physical meaning of metamaterial constitutive parameters,” *Physical Review B*, vol. 83, no. 8, p. 081102, Feb. 2011.
- [24] D. Sjöberg and C. Larsson, “Cramér–Rao Bounds for Determination of Permittivity and Permeability in Slabs,” *IEEE Transactions on Microwave Theory and Techniques*, vol. 59, no. 11, pp. 2970–2977, Nov. 2011.
- [25] S. B. Glybovski, S. A. Tretyakov, P. A. Belov, Y. S. Kivshar, and C. R. Simovski, “Metasurfaces: From microwaves to visible,” *Physics Reports*, vol. 634, pp. 1 – 72, 2016, metasurfaces: From microwaves to visible. [Online]. Available: <https://www.sciencedirect.com/science/article/pii/S0370157316300618>
- [26] R. Rodriguez-Berral, F. Medina, F. Mesa, and M. Garcia-Vigueras, “Quasi-Analytical Modeling of Transmission/Reflection in Strip/Slit Gratings Loaded With Dielectric Slabs,” *IEEE Transactions on Microwave Theory and Techniques*, vol. 60, no. 3, pp. 405–418, Mar. 2012.
- [27] D. M. Pozar, *Microwave engineering*. John Wiley & Sons, 2009.
- [28] B. A. Munk, *Frequency Selective Surfaces: Theory and Design*. John Wiley & Sons, 2005.
- [29] F. Costa, A. Monorchio, and G. Manara, “An Overview of Equivalent Circuit Modeling Techniques of Frequency Selective Surfaces and Metasurfaces,” *Applied Computational Electromagnetics Society Journal*, vol. 29, no. 12, 2014.

- [30] F. Costa and A. Monorchio, "Closed-Form Analysis of Reflection Losses in Microstrip Reflectarray Antennas," *IEEE Transactions on Antennas and Propagation*, vol. 60, no. 10, pp. 4650–4660, Oct. 2012.
- [31] I. Anderson, "On the theory of self-resonant grids," *The Bell System Technical Journal*, vol. 54, no. 10, pp. 1725–1731, Dec. 1975.
- [32] F. Costa, A. Monorchio, and G. Manara, "Efficient Analysis of Frequency-Selective Surfaces by a Simple Equivalent-Circuit Model," *IEEE Antennas and Propagation Magazine*, vol. 54, no. 4, pp. 35–48, Aug. 2012.
- [33] O. Luukkonen, C. Simovski, G. Granet, G. Goussetis, D. Lioubtchenko, A. V. Raisanen, and S. A. Tretyakov, "Simple and Accurate Analytical Model of Planar Grids and High-Impedance Surfaces Comprising Metal Strips or Patches," *IEEE Transactions on Antennas and Propagation*, vol. 56, no. 6, pp. 1624–1632, Jun. 2008.
- [34] C. Pfeiffer and A. Grbic, "Bianisotropic metasurfaces for optimal polarization control: Analysis and synthesis," *Phys. Rev. Applied*, vol. 2, p. 044011, Oct 2014. [Online]. Available: <https://link.aps.org/doi/10.1103/PhysRevApplied.2.044011>
- [35] M. Borgese and F. Costa, "A simple equivalent circuit approach for anisotropic frequency-selective surfaces and metasurfaces," *IEEE Transactions on Antennas and Propagation*, vol. 68, no. 10, pp. 7088–7098, 2020.
- [36] D. T. Blackstock, *Fundamentals of Physical Acoustics*. John Wiley & Sons, Apr. 2000.
- [37] C. A. Palmer, E. G. Loewen, and R. G. L. Thermo, *Diffraction grating handbook*. Newport Corporation Springfield, OH, 2005.
- [38] T. K. Gaylord and M. G. Moharam, "Planar dielectric grating diffraction theories," *Applied Physics B*, vol. 28, no. 1, pp. 1–14, May 1982.
- [39] F. Costa, A. Monorchio, and G. Manara, "Wideband scattering diffusion by using diffraction of periodic surfaces and optimized unit cell geometries," *Scientific reports*, vol. 6, p. 25458, 2016.
- [40] M. Garcia-Vigueras, F. Mesa, F. Medina, R. Rodriguez-Berral, and J. Gomez-Tornero, "Simplified Circuit Model for Arrays of Metallic Dipoles Sandwiched Between Dielectric Slabs Under Arbitrary Incidence," *IEEE Transactions on Antennas and Propagation*, vol. 60, no. 10, pp. 4637–4649, Oct. 2012.
- [41] D. Sievenpiper, L. Zhang, R. F. J. Broas, N. G. Alexopolous, and E. Yablonovitch, "High-impedance electromagnetic surfaces with a forbidden frequency band," *IEEE Transactions on Microwave Theory and Techniques*, vol. 47, no. 11, pp. 2059–2074, Nov. 1999.
- [42] S. Clavijo, R. E. Diaz, and W. E. McKinzie, "Design methodology for Sievenpiper high-impedance surfaces: an artificial magnetic conductor for positive gain electrically small antennas," *IEEE Transactions on Antennas and Propagation*, vol. 51, no. 10, pp. 2678–2690, Oct. 2003.
- [43] F. Costa, S. Genovesi, and A. Monorchio, "On the Bandwidth of High-Impedance Frequency Selective Surfaces," *IEEE Antennas and Wireless Propagation Letters*, vol. 8, pp. 1341–1344, 2009.
- [44] A. B. Yakovlev, O. Luukkonen, C. R. Simovski, S. A. Tretyakov, S. Paulotto, P. Baccarelli, and G. W. Hanson, "Analytical Modeling of Surface Waves on High Impedance Surfaces," in *Metamaterials and Plasmonics: Fundamentals, Modelling, Applications*, ser. NATO Science for Peace and Security Series B: Physics and Biophysics. Springer, Dordrecht, 2009, pp. 239–254, doi: 10.1007/978-1-4020-9407-1_18. [Online]. Available: https://link.springer.com/chapter/10.1007/978-1-4020-9407-1_18
- [45] O. Luukkonen, F. Costa, C. R. Simovski, A. Monorchio, and S. A. Tretyakov, "A Thin Electromagnetic Absorber for Wide Incidence Angles and Both Polarizations," *IEEE Transactions on Antennas and Propagation*, vol. 57, no. 10, pp. 3119–3125, Oct. 2009.
- [46] W. Rotman, "Plasma simulation by artificial dielectrics and parallel-plate media," *IRE Transactions on Antennas and Propagation*, vol. 10, no. 1, pp. 82–95, Jan. 1962.

- [47] F. Costa, O. Luukkonen, C. R. Simovski, A. Monorchio, S. A. Tretyakov, and P. M. Maagt, "TE Surface Wave Resonances on High-Impedance Surface Based Antennas: Analysis and Modeling," *IEEE Transactions on Antennas and Propagation*, vol. 59, no. 10, pp. 3588–3596, Oct. 2011.
- [48] M. J. Lockyear, A. P. Hibbins, and J. R. Sambles, "Microwave Surface-Plasmon-Like Modes on Thin Metamaterials," *Physical Review Letters*, vol. 102, no. 7, p. 073901, Feb. 2009.
- [49] W. L. Barnes, A. Dereux, and T. W. Ebbesen, "Surface plasmon subwavelength optics," Aug. 2003, dOI: 10.1038/nature01937. [Online]. Available: <https://www.nature.com/articles/nature01937>
- [50] H. Kim, C. M. Gilmore, A. Pique, J. S. Horwitz, H. Mattoussi, H. Murata, Z. H. Kafafi, and D. B. Chrisey, "Electrical, optical, and structural properties of indium–tin–oxide thin films for organic light-emitting devices," *Journal of Applied Physics*, vol. 86, no. 11, pp. 6451–6461, 1999.
- [51] A. K. Geim and K. S. Novoselov, "The rise of graphene," *Nature materials*, vol. 6, no. 3, pp. 183–191, 2007.
- [52] D. S. Ginley, H. Hosono, and D. C. Paine, "Handbook of transparent conductors," 2010. [Online]. Available: <http://link.springer.com/content/pdf/10.1007/978-1-4419-1638-9.pdf>
- [53] F. Yi, E. Shim, A. Y. Zhu, H. Zhu, J. C. Reed, and E. Cubukcu, "Voltage tuning of plasmonic absorbers by indium tin oxide," *Applied Physics Letters*, vol. 102, no. 22, p. 221102, 2013.
- [54] J. Perruisseau-Carrier, "Graphene for antenna applications: Opportunities and challenges from microwaves to THz," in *Antennas and Propagation Conference (LAPC), 2012 Loughborough*. IEEE, 2012, pp. 1–4. [Online]. Available: http://ieeexplore.ieee.org/xpls/abs_all.jsp?arnumber=6402934
- [55] A. Fallahi and J. Perruisseau-Carrier, "Design of tunable bi-periodic graphene metasurfaces," *Physical Review B*, vol. 86, no. 19, p. 195408, 2012.
- [56] "Acoustic metamaterial with negative modulus - IOPscience." [Online]. Available: <http://iopscience.iop.org/article/10.1088/0953-8984/21/17/175704/meta>
- [57] "Acoustic metamaterial with negative density - ScienceDirect." [Online]. Available: <http://www.sciencedirect.com/science/article/pii/S0375960109012754>
- [58] T. Brunet, A. Merlin, B. Mascaró, K. Zimny, J. Leng, O. Poncelet, C. Aristégui, and O. Mondain-Monval, "Soft 3d acoustic metamaterial with negative index," *Nature Materials*, vol. 14, no. 4, p. 384, Apr. 2015.
- [59] "Wave attenuation mechanism in an acoustic metamaterial with negative effective mass density - IOPscience." [Online]. Available: <http://iopscience.iop.org/article/10.1088/1367-2630/11/1/013003/meta>
- [60] P. A. Deymier, *Acoustic Metamaterials and Phononic Crystals*. Springer Science & Business Media, Jan. 2013, google-Books-ID: 8eg_AAAAQBAJ.
- [61] X. Jiang, B. Liang, X.-y. Zou, L.-l. Yin, and J.-c. Cheng, "Broadband field rotator based on acoustic metamaterials," *Applied Physics Letters*, vol. 104, no. 8, p. 083510, Feb. 2014.
- [62] S. A. Cummer, J. Christensen, and A. Alù, "Controlling sound with acoustic metamaterials," *Nature Reviews Materials*, vol. 1, no. 3, p. 16001, Mar. 2016.
- [63] R. V. Craster and S. Guenneau, *Acoustic Metamaterials: Negative Refraction, Imaging, Lensing and Cloaking*. Springer Science & Business Media, Dec. 2012, google-Books-ID: uv4IQ0tQJtkC.
- [64] "Phononic crystals and acoustic metamaterials - ScienceDirect." [Online]. Available: <http://www.sciencedirect.com/science/article/pii/S1369702109703153>
- [65] Z. Liu, X. Zhang, Y. Mao, Y. Y. Zhu, Z. Yang, C. T. Chan, and P. Sheng, "Locally Resonant Sonic Materials," *Science*, vol. 289, no. 5485, pp. 1734–1736, Sep. 2000.
- [66] L. Rayleigh, "The theory of the Helmholtz resonator," *Proceedings of the Royal Society of London. Series A, Containing Papers of a Mathematical and Physical Character*, vol. 92, no. 638, pp. 265–275, 1916.

- [67] J. Mei, G. Ma, M. Yang, Z. Yang, W. Wen, and P. Sheng, “Dark acoustic metamaterials as super absorbers for low-frequency sound,” *Nature Communications*, vol. 3, p. 756, Mar. 2012.
- [68] X. Cai, Q. Guo, G. Hu, and J. Yang, “Ultrathin low-frequency sound absorbing panels based on coplanar spiral tubes or coplanar Helmholtz resonators,” *Applied Physics Letters*, vol. 105, no. 12, p. 121901, 2014.
- [69] “Reflected wavefront manipulation based on ultrathin planar acoustic metasurfaces | Scientific Reports.” [Online]. Available: https://www.nature.com/articles/srep02546/fig_tab
- [70] “Phys. Rev. B 96, 125409 (2017) - Acoustic metasurfaces for scattering-free anomalous reflection and refraction.” [Online]. Available: <https://journals.aps.org/prb/abstract/10.1103/PhysRevB.96.125409>
- [71] “Phys. Rev. Lett. 103, 104301 (2009) - Acoustic Diode: Rectification of Acoustic Energy Flux in One-Dimensional Systems.” [Online]. Available: <https://journals.aps.org/prl/abstract/10.1103/PhysRevLett.103.104301>
- [72] R. Fleury, D. L. Sounas, C. F. Sieck, M. R. Haberman, and A. Alù, “Sound isolation and giant linear nonreciprocity in a compact acoustic circulator,” *Science*, vol. 343, no. 6170, pp. 516–519, 2014.
- [73] J. B. Pendry, D. Schurig, and D. R. Smith, “Controlling Electromagnetic Fields,” *Science*, vol. 312, no. 5781, pp. 1780–1782, Jun. 2006.
- [74] D. Schurig, J. J. Mock, B. J. Justice, S. A. Cummer, J. B. Pendry, A. F. Starr, and D. R. Smith, “Metamaterial Electromagnetic Cloak at Microwave Frequencies,” *Science*, vol. 314, no. 5801, pp. 977–980, Nov. 2006.
- [75] P.-S. Kildal, A. Kishk, and A. Tengs, “Reduction of forward scattering from cylindrical objects using hard surfaces,” *IEEE Transactions on Antennas and Propagation*, vol. 44, no. 11, pp. 1509–1520, Nov. 1996.
- [76] P.-S. Kildal, A. Kishk, and Z. Sipus, “RF invisibility using metamaterials: Harry Potter’s cloak or the Emperor’s new clothes?” in *2007 IEEE Antennas and Propagation Society International Symposium*, Jun. 2007, pp. 2361–2364.
- [77] P. Alitalo, O. Luukkonen, L. Jylha, J. Venermo, and S. Tretyakov, “Transmission-Line Networks Cloaking Objects From Electromagnetic Fields,” *IEEE Transactions on Antennas and Propagation*, vol. 56, no. 2, pp. 416–424, Feb. 2008.
- [78] S. Tretyakov, P. Alitalo, O. Luukkonen, and C. Simovski, “Broadband Electromagnetic Cloaking of Long Cylindrical Objects,” *Physical Review Letters*, vol. 103, no. 10, p. 103905, Sep. 2009.
- [79] A. Alù and N. Engheta, “Achieving transparency with plasmonic and metamaterial coatings,” *Physical Review E*, vol. 72, no. 1, p. 016623, Jul. 2005.
- [80] P.-Y. Chen and A. Alù, “Mantle cloaking using thin patterned metasurfaces,” *Physical Review B*, vol. 84, no. 20, p. 205110, Nov. 2011.
- [81] J. Li and J. Pendry, “Hiding under the Carpet: A New Strategy for Cloaking,” *Physical Review Letters*, vol. 101, no. 20, p. 203901, Nov. 2008.
- [82] H. Chen, B. Zheng, L. Shen, H. Wang, X. Zhang, N. I. Zheludev, and B. Zhang, “Ray-optics cloaking devices for large objects in incoherent natural light,” *Nature Communications*, vol. 4, Oct. 2013. [Online]. Available: <http://www.nature.com/ncomms/2013/131024/ncomms3652/full/ncomms3652.html?message-global=remove>
- [83] P. Alitalo and S. Tretyakov, “Broadband Electromagnetic Cloaking Realized With Transmission-Line and Waveguiding Structures,” *Proceedings of the IEEE*, vol. 99, no. 10, pp. 1646–1659, Oct. 2011.
- [84] R. Fleury and A. Alù, “Cloaking and invisibility: A review,” in *Forum for Electromagnetic Research Methods and Application Technologies (FERMAT)*, vol. 1, 2014, pp. 1–24. [Online]. Available: <http://e-fermat.org/files/articles/15302ddcf89fad.pdf>
- [85] P.-S. Kildal, “Artificially soft and hard surfaces in electromagnetics,” *IEEE Transactions on Antennas and Propagation*, vol. 38, no. 10, pp. 1537–1544, Oct. 1990.
- [86] B. Edwards, A. Alù, M. Silveirinha, and N. Engheta, “Experimental Verification of Plasmonic Cloaking at Microwave Frequencies with Metamaterials,” *Physical Review Letters*, vol. 103, no. 15, p. 153901, Oct. 2009.

- [87] G. Labate, S. K. Podilchak, and L. Matekovits, "Closed-form harmonic contrast control with surface impedance coatings for conductive objects," *Appl. Opt.*, vol. 56, no. 36, pp. 10055–10059, Dec 2017. [Online]. Available: <http://ao.osa.org/abstract.cfm?URI=ao-56-36-10055>
- [88] M. Silveirinha, A. Alù, and N. Engheta, "Infrared and optical invisibility cloak with plasmonic implants based on scattering cancellation," *Physical Review B*, vol. 78, no. 7, p. 075107, Aug. 2008.
- [89] F. Monticone and A. Alù, "Invisibility exposed: physical bounds on passive cloaking," *Optica*, vol. 3, no. 7, pp. 718–724, Jul 2016. [Online]. Available: <http://www.osapublishing.org/optica/abstract.cfm?URI=optica-3-7-718>
- [90] J. C. Soric, P. Y. Chen, A. Kerkhoff, D. Rainwater, K. Melin, and A. Alù, "Demonstration of an ultralow profile cloak for scattering suppression of a finite-length rod in free space," *New Journal of Physics*, vol. 15, no. 3, p. 033037, Mar. 2013.
- [91] S. Genovesi, F. Costa, and A. Monorchio, "Wideband Radar Cross Section Reduction of Slot Antennas Arrays," *IEEE Transactions on Antennas and Propagation*, vol. 62, no. 1, pp. 163–173, Jan. 2014.
- [92] H.-K. Jang, J.-H. Shin, and C.-G. Kim, "Low RCS patch array antenna with electromagnetic bandgap using a conducting polymer," in *International Conference on Electromagnetics in Advanced Applications (ICEAA), 2010*. IEEE, 2010, pp. 140–143. [Online]. Available: http://ieeexplore.ieee.org/xpls/abs_all.jsp?arnumber=5652186
- [93] D. Williams, "Damping of the resonant modes of a rectangular metal package [MMICs]," *IEEE Transactions on Microwave Theory and Techniques*, vol. 37, no. 1, pp. 253–256, Jan. 1989.
- [94] P. Dixon, "Cavity-resonance dampening," *IEEE Microwave Magazine*, vol. 6, no. 2, pp. 74–84, Jun. 2005.
- [95] R. Araneo, G. Lovat, and S. Celozzi, "Low-frequency intertwined spiral-aperture absorbers for Shielded enclosures," in *2013 IEEE International Symposium on Electromagnetic Compatibility (EMC)*, Aug. 2013, pp. 456–461.
- [96] R. Ling, J. Scholler, and P. Y. Ufimtsev, "The Propagation and Excitation of Surface Waves in an Absorbing Layer - Abstract," *Journal of Electromagnetic Waves and Applications*, vol. 12, no. 7, pp. 883–884, Jan. 1998.
- [97] D. Shively, "Surface waves on a grounded dielectric slab covered by a resistive sheet," *IEEE Transactions on Antennas and Propagation*, vol. 41, no. 3, pp. 348–350, Mar. 1993.
- [98] F. Costa, S. Genovesi, A. Monorchio, and G. Manara, "Low-Cost Metamaterial Absorbers for Sub-GHz Wireless Systems," *IEEE Antennas and Wireless Propagation Letters*, vol. 13, pp. 27–30, 2014.
- [99] S. Yagitani, K. Katsuda, M. Nojima, Y. Yoshimura, and H. Sugiura, "Imaging radio-frequency power distributions by an EBG absorber," *IEICE transactions on communications*, vol. 94, no. 8, pp. 2306–2315, 2011.
- [100] T. Maier and H. Brückl, "Wavelength-tunable microbolometers with metamaterial absorbers," *Optics letters*, vol. 34, no. 19, pp. 3012–3014, 2009.
- [101] S. A. Kuznetsov, A. G. Paulish, A. V. Gelfand, P. A. Lazorskiy, and V. N. Fedorinin, "Bolometric THz-to-IR converter for terahertz imaging," *Applied Physics Letters*, vol. 99, no. 2, p. 023501, 2011.
- [102] H.-T. Chen, W. J. Padilla, M. J. Cich, A. K. Azad, R. D. Averitt, and A. J. Taylor, "A metamaterial solid-state terahertz phase modulator," *Nature Photonics*, vol. 3, no. 3, pp. 148–151, 2009.
- [103] X. Liu, T. Tyler, T. Starr, A. F. Starr, N. M. Jokerst, and W. J. Padilla, "Taming the blackbody with infrared metamaterials as selective thermal emitters," *Physical review letters*, vol. 107, no. 4, p. 045901, 2011.
- [104] W. Dallenbach and W. Kleinsteuber, "Reflection and Absorption of Decimeter-Waves by Plane Dielectric Layers," *Hochfreq. u Elektroak*, pp. 152–156, 1938.
- [105] D. Sjöberg, "Analysis of wave propagation in stratified structures using circuit analogues, with application to electromagnetic absorbers," *European Journal of Physics*, vol. 29, no. 4, p. 721, 2008.
- [106] L. Sun, H. Cheng, Y. Zhou, and J. Wang, "Broadband metamaterial absorber based on coupling resistive frequency selective surface," *Optics express*, vol. 20, no. 4, pp. 4675–4680, 2012.

- [107] A. Kazemzadeh and A. Karlsson, "Multilayered wideband absorbers for oblique angle of incidence," *IEEE Transactions on Antennas and Propagation*, vol. 58, no. 11, pp. 3637–3646, 2010.
- [108] A. Kazemzadeh, "Nonmagnetic ultrawideband absorber with optimal thickness," *IEEE Transactions on Antennas and Propagation*, vol. 59, no. 1, pp. 135–140, 2011.
- [109] A. K. Zadeh and A. Karlsson, "Capacitive circuit method for fast and efficient design of wideband radar absorbers," *IEEE Transactions on Antennas and Propagation*, vol. 57, no. 8, pp. 2307–2314, 2009.
- [110] C. Christopoulos, *The transmission-line modeling method*. Oxford University Press, 1995. [Online]. Available: <http://cds.cern.ch/record/1480786>
- [111] G. T. Ruck, *Radar cross section handbook*. Plenum Publishing Corporation, 1970, vol. 1.
- [112] Y. Naito and K. Suetake, "Application of Ferrite to Electromagnetic Wave Absorber and its Characteristics," *IEEE Transactions on Microwave Theory and Techniques*, vol. 19, no. 1, pp. 65–72, Jan. 1971.
- [113] E. Knott and C. D. Lunden, "The two-sheet capacitive Jaumann absorber," *IEEE Transactions on Antennas and Propagation*, vol. 43, no. 11, pp. 1339–1343, Nov. 1995.
- [114] F. Costa, A. Monorchio, and G. Manara, "Analysis and design of ultra thin electromagnetic absorbers comprising resistively loaded high impedance surfaces," *IEEE Transactions on Antennas and Propagation*, vol. 58, no. 5, pp. 1551–1558, 2010.
- [115] R. Fante and M. McCormack, "Reflection properties of the Salisbury screen," *IEEE Transactions on Antennas and Propagation*, vol. 36, no. 10, pp. 1443–1454, Oct. 1988.
- [116] F. Costa and A. Monorchio, "Closed-form analysis of reflection losses in microstrip reflectarray antennas," *IEEE Transactions on Antennas and Propagation*, vol. 60, no. 10, pp. 4650–4660, 2012.
- [117] F. Costa, S. Genovesi, A. Monorchio, and G. Manara, "A circuit-based model for the interpretation of perfect metamaterial absorbers," *IEEE Transactions on Antennas and Propagation*, vol. 61, no. 3, pp. 1201–1209, 2013.
- [118] K. N. Rozanov, "Ultimate thickness to bandwidth ratio of radar absorbers," *IEEE Transactions on Antennas and Propagation*, vol. 48, no. 8, pp. 1230–1234, 2000.
- [119] H.-B. Zhang, P.-H. Zhou, H.-P. Lu, Y.-Q. Xu, D.-F. Liang, and L.-J. Deng, "Resistance selection of high impedance surface absorbers for perfect and broadband absorption," *IEEE Transactions on Antennas and Propagation*, vol. 61, no. 2, pp. 976–979, 2013.
- [120] O. Luukkonen, C. Simovski, G. Granet, G. Goussetis, D. Lioubtchenko, A. V. Raisanen, and S. A. Tretyakov, "Simple and accurate analytical model of planar grids and high-impedance surfaces comprising metal strips or patches," *IEEE Transactions on Antennas and Propagation*, vol. 56, no. 6, pp. 1624–1632, 2008.
- [121] D. J. Kozakoff, *Analysis of radome-enclosed antennas*. Artech House, 2010.
- [122] J. D. Walton, *Radome engineering handbook: design and principles*. M. Dekker, 1970, vol. 1.
- [123] D. Lynch and I. of Electrical Engineers, *Introduction to RF stealth*. Scitech, 2004.
- [124] E. Magill and H. Wheeler, "Wide-angle impedance matching of a planar array antenna by a dielectric sheet," *IEEE Transactions on Antennas and Propagation*, vol. 14, no. 1, pp. 49–53, January 1966.
- [125] T. R. Cameron and G. V. Eleftheriades, "Analysis and characterization of a wide-angle impedance matching metasurface for dipole phased arrays," *IEEE Transactions on Antennas and Propagation*, vol. 63, no. 9, pp. 3928–3938, Sept 2015.
- [126] F. Silvestri, L. Cifola, and G. Gerini, "Diamagneto-dielectric anisotropic wide angle impedance matching layers for active phased arrays," *Progress In Electromagnetics Research*, vol. 70, pp. 1–12, 2016.
- [127] D. Bianchi, S. Genovesi, M. Borgese, F. Costa, and A. Monorchio, "Element-independent design of wide-angle impedance matching radomes by using the generalized scattering matrix approach," *IEEE Transactions on Antennas and Propagation*, vol. 66, no. 9, pp. 4708–4718, 2018.
- [128] B. A. Munk, *Metamaterials: critique and alternatives*. John Wiley & Sons, 2009.

- [129] F. Costa and A. Monorchio, "A frequency selective radome with wideband absorbing properties," *IEEE Transactions on Antennas and Propagation*, vol. 60, no. 6, pp. 2740–2747, 2012.
- [130] M. Cherniakov, *Bistatic Radars: Emerging Technology*. John Wiley & Sons, Oct. 2008, google-Books-ID: Nn2nYaYiPzEC.
- [131] F. Costa, S. Genovesi, and A. Monorchio, "A frequency selective absorbing ground plane for low-rCS microstrip antenna arrays," *Progress In Electromagnetics Research*, vol. 126, pp. 317–332, 2012.
- [132] S. Genovesi, F. Costa, and A. Monorchio, "Low-profile array with reduced radar cross section by using hybrid frequency selective surfaces," *IEEE Transactions on Antennas and Propagation*, vol. 60, no. 5, pp. 2327–2335, 2012.
- [133] Y. Zheng, J. Gao, X. Cao, Z. Yuan, and H. Yang, "Wideband rCS reduction of a microstrip antenna using artificial magnetic conductor structures," *IEEE Antennas and Wireless Propagation Letters*, vol. 14, pp. 1582–1585, 2015.
- [134] W. Pan, C. Huang, P. Chen, X. Ma, C. Hu, and X. Luo, "A low-rCS and high-gain partially reflecting surface antenna," *IEEE Transactions on Antennas and Propagation*, vol. 62, no. 2, pp. 945–949, Feb 2014.
- [135] C. Huang, W. Pan, X. Ma, and X. Luo, "A frequency reconfigurable directive antenna with wideband low-rCS property," *IEEE Transactions on Antennas and Propagation*, vol. 64, no. 3, pp. 1173–1178, March 2016.
- [136] X. Ni, S. Ishii, A. V. Kildishev, and V. M. Shalaev, "Ultra-thin, planar, babinet-inverted plasmonic metalenses," *Light: Science & Applications*, vol. 2, no. 4, p. e72, 2013.
- [137] S. Sun, Q. He, S. Xiao, Q. Xu, X. Li, and L. Zhou, "Gradient-index meta-surfaces as a bridge linking propagating waves and surface waves," *Nature Materials*, vol. 11, p. 426, Apr. 2012. [Online]. Available: <http://dx.doi.org/10.1038/nmat3292>
- [138] F. Aieta, P. Genevet, M. A. Kats, N. Yu, R. Blanchard, Z. Gaburro, and F. Capasso, "Aberration-free ultrathin flat lenses and axicons at telecom wavelengths based on plasmonic metasurfaces," *Nano Letters*, vol. 12, no. 9, pp. 4932–4936, 2012.
- [139] J. B. Pendry, D. Schurig, and D. R. Smith, "Controlling electromagnetic fields," *Science*, vol. 312, no. 5781, pp. 1780–1782, 2006. [Online]. Available: <http://science.sciencemag.org/content/312/5781/1780>
- [140] U. Leonhardt, "Optical Conformal Mapping," *Science*, vol. 312, no. 5781, pp. 1777–1780, 2006. [Online]. Available: <http://science.sciencemag.org/content/312/5781/1777>
- [141] J. B. Pendry, "Negative refraction makes a perfect lens," *Phys. Rev. Lett.*, vol. 85, pp. 3966–3969, Oct 2000. [Online]. Available: <https://link.aps.org/doi/10.1103/PhysRevLett.85.3966>
- [142] W. Cai, V. Shalaev, and D. K. Paul, "Optical Metamaterials: Fundamentals and Applications," *Physics Today*, vol. 63, no. 9, p. 57, 2010.
- [143] N. Engheta and R. W. Ziolkowski, *Metamaterials: physics and engineering explorations*. John Wiley & Sons, 2006.
- [144] J. Huang and J. A. Encinar, *Reflectarray antennas*. Piscataway, N.J.; Hoboken, N.J.: IEEE Press ; Wiley-Interscience, 2008.
- [145] J. Shaker, M. R. Chaharmir, and J. Ethier, *Reflectarray antennas: analysis, design, fabrication, and measurement*, ser. The Artech House antennas and propagation series. Boston: Artech House, 2014, oCLC: ocn868070017.
- [146] M. Borgese, F. Costa, S. Genovesi, and A. Monorchio, "An iterative design procedure for multiband single-layer reflectarrays: Design and experimental validation," *IEEE Transactions on Antennas and Propagation*, vol. 65, no. 9, pp. 4595–4606, 2017.
- [147] O. Tsilipakos, A. C. Tasolamprou, A. Ptilakis, F. Liu, X. Wang, M. S. Mirmoosa, D. C. Tzarouchis, S. Abadal, H. Taghvaei, C. Liaskos *et al.*, "Toward intelligent metasurfaces: The progress from globally tunable metasurfaces to software-defined metasurfaces with an embedded network of controllers," *Advanced Optical Materials*, vol. 8, no. 17, p. 2000783, 2020.

- [148] D. Berry, R. Malech, and W. Kennedy, "The reflectarray antenna," *IEEE Transactions on Antennas and Propagation*, vol. 11, no. 6, pp. 645–651, Nov 1963.
- [149] Y. Zhuang, K.-L. Wu, C. Wu, and J. Litva, "Microstrip reflectarrays: Full-wave analysis and design scheme," in *Antennas and Propagation Society International Symposium, 1993. AP-S. Digest.* IEEE, 1993, pp. 1386–1389.
- [150] D. Pozar and T. Metzler, "Analysis of a reflectarray antenna using microstrip patches of variable size," *Electronics Letters*, vol. 29, no. 8, pp. 657–658, 1993.
- [151] J. Huang and R. J. Pogorzelski, "A ka-band microstrip reflectarray with elements having variable rotation angles," *IEEE transactions on antennas and propagation*, vol. 46, no. 5, pp. 650–656, 1998.
- [152] H. Q. Ngo, E. G. Larsson, and T. L. Marzetta, "Energy and spectral efficiency of very large multiuser mimo systems," *IEEE Transactions on Communications*, vol. 61, no. 4, pp. 1436–1449, 2013.
- [153] E. G. Larsson, O. Edfors, F. Tufvesson, and T. L. Marzetta, "Massive mimo for next generation wireless systems," *IEEE communications magazine*, vol. 52, no. 2, pp. 186–195, 2014.
- [154] P. Rocca, G. Oliveri, R. J. Mailloux, and A. Massa, "Unconventional phased array architectures and design methodologies—a review," *Proceedings of the IEEE*, vol. 104, no. 3, pp. 544–560, 2016.
- [155] H. Zhao, Y. Shuang, M. Wei, T. J. Cui, P. Del Hougne, and L. Li, "Metasurface-assisted massive backscatter wireless communication with commodity wi-fi signals," *Nature communications*, vol. 11, no. 1, pp. 1–10, 2020.
- [156] C. Huang, A. Zappone, G. C. Alexandropoulos, M. Debbah, and C. Yuen, "Reconfigurable intelligent surfaces for energy efficiency in wireless communication," *IEEE Transactions on Wireless Communications*, vol. 18, no. 8, pp. 4157–4170, 2019.
- [157] P. Mursia, V. Sciancalepore, A. Garcia-Saavedra, L. Cottatellucci, X. Costa-Pérez, and D. Gesbert, "Risma: Reconfigurable intelligent surfaces enabling beamforming for iot massive access," *IEEE Journal on Selected Areas in Communications*, 2020.
- [158] D. F. Sievenpiper, J. H. Schaffner, H. J. Song, R. Y. Loo, and G. Tandonan, "Two-dimensional beam steering using an electrically tunable impedance surface," *IEEE Transactions on antennas and propagation*, vol. 51, no. 10, pp. 2713–2722, 2003.
- [159] D. F. Sievenpiper, "Forward and backward leaky wave radiation with large effective aperture from an electronically tunable textured surface," *IEEE transactions on antennas and propagation*, vol. 53, no. 1, pp. 236–247, 2005.
- [160] H. Li, F. Costa, Y. Wang, Q. Cao, and A. Monorchio, "A switchable and tunable multifunctional absorber/reflector with polarization-insensitive features," *International Journal of RF and Microwave Computer-Aided Engineering*, p. e22573.
- [161] Q. He, S. Sun, L. Zhou *et al.*, "Tunable/reconfigurable metasurfaces: physics and applications," *Research*, vol. 2019, p. 1849272, 2019.
- [162] X. Wang, A. Díaz-Rubio, H. Li, S. A. Tretyakov, and A. Alù, "Theory and design of multifunctional space-time metasurfaces," *Physical Review Applied*, vol. 13, no. 4, p. 044040, 2020.
- [163] E. Björnson and L. Sanguinetti, "Power scaling laws and near-field behaviors of massive mimo and intelligent reflecting surfaces," *IEEE Open Journal of the Communications Society*, vol. 1, pp. 1306–1324, 2020.
- [164] W. Chen, L. Bai, W. Tang, S. Jin, W. X. Jiang, and T. J. Cui, "Angle-dependent phase shifter model for reconfigurable intelligent surfaces: Does the angle-reciprocity hold?" *IEEE Communications Letters*, vol. 24, no. 9, pp. 2060–2064, 2020.
- [165] F. Costa and M. Borgese, "Electromagnetic model of reflective intelligent surfaces," 2021.
- [166] S. Abeywickrama, R. Zhang, Q. Wu, and C. Yuen, "Intelligent reflecting surface: Practical phase shift model and beamforming optimization," *arXiv preprint arXiv:2002.10112*, 2020.

- [167] O. Luukkonen, C. Simovski, G. Granet, G. Goussetis, D. Lioubtchenko, A. V. Raisanen, and S. A. Tretyakov, "Simple and accurate analytical model of planar grids and high-impedance surfaces comprising metal strips or patches," *IEEE Transactions on Antennas and Propagation*, vol. 56, no. 6, pp. 1624–1632, June 2008.
- [168] E. Basar, M. Di Renzo, J. De Rosny, M. Debbah, M.-S. Alouini, and R. Zhang, "Wireless communications through reconfigurable intelligent surfaces," *IEEE Access*, vol. 7, pp. 116 753–116 773, 2019.
- [169] G. C. Alexandropoulos, G. Lerosey, M. Debbah, and M. Fink, "Reconfigurable intelligent surfaces and metamaterials: The potential of wave propagation control for 6g wireless communications," *arXiv preprint arXiv:2006.11136*, 2020.
- [170] C. Dietlein, A. Luukanen, Z. Popovi, and E. Grossman, "A W-Band Polarization Converter and Isolator," *IEEE Transactions on Antennas and Propagation*, vol. 55, no. 6, pp. 1804–1809, Jun. 2007.
- [171] M. Euler, V. Fusco, R. Cahill, and R. Dickie, "325 GHz Single Layer Sub-Millimeter Wave FSS Based Split Slot Ring Linear to Circular Polarization Converter," *IEEE Transactions on Antennas and Propagation*, vol. 58, no. 7, pp. 2457–2459, Jul. 2010.
- [172] M. Kotlyar, L. Bolla, M. Midrio, L. O'Faolain, and T. Krauss, "Compact polarization converter in InP-based material," *Optics express*, vol. 13, no. 13, pp. 5040–5045, 2005.
- [173] B. Bai, Y. Svirko, J. Turunen, and T. Vallius, "Optical activity in planar chiral metamaterials: Theoretical study," *Physical Review A*, vol. 76, no. 2, Aug. 2007. [Online]. Available: <http://link.aps.org/doi/10.1103/PhysRevA.76.023811>
- [174] M. Veysi, C. Guclu, O. Boyraz, and F. Capolino, "Thin anisotropic metasurfaces for simultaneous light focusing and polarization manipulation," *Journal of the Optical Society of America B*, vol. 32, no. 2, p. 318, Feb. 2015.
- [175] F. Costa and M. Borgese, "Systematic design of transmission-type polarization converters comprising multilayered anisotropic metasurfaces," *Phys. Rev. Applied*, vol. 14, p. 034049, Sep 2020. [Online]. Available: <https://link.aps.org/doi/10.1103/PhysRevApplied.14.034049>
- [176] Z. Wei, Y. Cao, Y. Fan, X. Yu, and H. Li, "Broadband polarization transformation via enhanced asymmetric transmission through arrays of twisted complementary split-ring resonators," *Applied Physics Letters*, vol. 99, no. 22, p. 221907, 2011.
- [177] N. Yu, P. Genevet, M. A. Kats, F. Aieta, J.-P. Tetienne, F. Capasso, and Z. Gaburro, "Light propagation with phase discontinuities: generalized laws of reflection and refraction," *science*, vol. 334, no. 6054, pp. 333–337, 2011.
- [178] G. Manara, A. Monorchio, and R. Mittra, "Frequency selective surface design based on genetic algorithm," *Electronics Letters*, vol. 35, no. 17, pp. 1400–1401, 1999.
- [179] M. Ohira, H. Deguchi, M. Tsuji, and H. Shigesawa, "Multiband single-layer frequency selective surface designed by combination of genetic algorithm and geometry-refinement technique," *IEEE Transactions on Antennas and Propagation*, vol. 52, no. 11, pp. 2925–2931, 2004.
- [180] M. Borgese, F. Costa, S. Genovesi, A. Monorchio, and G. Manara, "Optimal design of miniaturized reflecting metasurfaces for ultra-wideband and angularly stable polarization conversion," *Scientific reports*, vol. 8, no. 1, pp. 1–11, 2018.
- [181] X. Gao, X. Han, W.-P. Cao, H. O. Li, H. F. Ma, and T. J. Cui, "Ultrawideband and High-Efficiency Linear Polarization Converter Based on Double V-Shaped Metasurface," *IEEE Transactions on Antennas and Propagation*, vol. 63, no. 8, pp. 3522–3530, Aug. 2015.
- [182] J.-L. Wu, B.-Q. Lin, and X.-Y. Da, "Ultra-wideband reflective polarization converter based on anisotropic metasurface," *Chinese Physics B*, vol. 25, no. 8, p. 088101, Aug. 2016.
- [183] B.-Q. Lin, X.-Y. Da, J.-L. Wu, W. Li, Y.-W. Fang, and Z.-H. Zhu, "Ultra-wideband and high-efficiency cross polarization converter based on anisotropic metasurface," *Microwave and Optical Technology Letters*, vol. 58, no. 10, pp. 2402–2405, Oct. 2016.
- [184] F. Yang and Y. Rahmat-Samii, "Reflection phase characterizations of the EBG ground plane for low profile wire antenna applications," *IEEE Transactions on Antennas and Propagation*, vol. 51, no. 10, pp. 2691–2703, Oct. 2003.

- [185] M. F. Abedin and M. Ali, "Effects of EBG reflection phase profiles on the input impedance and bandwidth of ultrathin directional dipoles," *IEEE Transactions on Antennas and Propagation*, vol. 53, no. 11, pp. 3664–3672, Nov. 2005.
- [186] S. Paulotto, P. Baccarelli, P. Burghignoli, G. Lovat, G. W. Hanson, and A. B. Yakovlev, "Homogenized Green's Functions for an Aperiodic Line Source Over Planar Densely Periodic Artificial Impedance Surfaces," *IEEE Transactions on Microwave Theory and Techniques*, vol. 58, no. 7, pp. 1807–1817, Jul. 2010.
- [187] G. Bianconi, F. Costa, S. Genovesi, and A. Monorchio, "Optimal Design of Dipole Antennas Backed by a Finite High - Impedance Screen," *Progress In Electromagnetics Research*, vol. 18, pp. 137–151, 2011.
- [188] A. O. T. Tamir, "Guided complex waves. part 1: Fields at an interface," *Proceedings of the Institution of Electrical Engineers*, vol. 110, pp. 310–324(14), February 1963. [Online]. Available: <http://digital-library.theiet.org/content/journals/10.1049/piee.1963.0044>
- [189] S. K. Podilchak, A. P. Freundorfer, and Y. M. M. Antar, "Surface-wave launchers for beam steering and application to planar leaky-wave antennas," *IEEE Transactions on Antennas and Propagation*, vol. 57, no. 2, pp. 355–363, Feb 2009.
- [190] G. Lovat, P. Burghignoli, and D. R. Jackson, "Fundamental properties and optimization of broadside radiation from uniform leaky-wave antennas," *IEEE Transactions on Antennas and Propagation*, vol. 54, no. 5, pp. 1442–1452, May 2006.
- [191] D. R. Jackson and A. A. Oliner, *Leaky-Wave Antennas*. John Wiley & Sons, Inc., 2007, pp. 325–367. [Online]. Available: <http://dx.doi.org/10.1002/9780470294154.ch7>
- [192] M. Garcia-Vigueras, J. L. Gomez-Tornero, G. Goussetis, A. R. Weily, and Y. J. Guo, "Efficient synthesis of 1-d fabry-perot antennas with low sidelobe levels," *IEEE Antennas and Wireless Propagation Letters*, vol. 11, pp. 869–872, 2012.
- [193] R. Guzman-Quiros, J. L. Gomez-Tornero, A. R. Weily, and Y. J. Guo, "Electronically steerable 1-d fabry-perot leaky-wave antenna employing a tunable high impedance surface," *IEEE Transactions on Antennas and Propagation*, vol. 60, no. 11, pp. 5046–5055, Nov 2012.
- [194] F. Costa, D. Bianchi, A. Monorchio, and G. Manara, "Linear fabry-perot/leaky-wave antennas excited by multiple sources," *IEEE Transactions on Antennas and Propagation*, vol. 66, no. 10, pp. 5150–5159, 2018.
- [195] D. R. Jackson, C. Caloz, and T. Itoh, "Leaky-wave antennas," *Proceedings of the IEEE*, vol. 100, no. 7, pp. 2194–2206, July 2012.
- [196] F. Monticone and A. Alù, "Leaky-wave theory, techniques, and applications: From microwaves to visible frequencies," *Proceedings of the IEEE*, vol. 103, no. 5, pp. 793–821, May 2015.
- [197] P. Hariharan, *Optical Holography: Principles, techniques and applications*. Cambridge University Press, 1996.
- [198] N. D. Yuri, "On the reflection of optical properties of an object in a wave field of light scattered by it," *Reports of Academy of Sciences of USSR*, vol. 144, no. 6, pp. 1275–1278, 1962.
- [199] M. ElSherbiny, A. E. Fathy, A. Rosen, G. Ayers, and S. M. Perlow, "Holographic antenna concept, analysis, and parameters," *IEEE Transactions on Antennas and Propagation*, vol. 52, no. 3, pp. 830–839, March 2004.
- [200] A. Oliner and A. Hessel, "Guided waves on sinusoidally-modulated reactance surfaces," *IRE Transactions on Antennas and Propagation*, vol. 7, no. 5, pp. 201–208, December 1959.
- [201] D. Sievenpiper, J. Colburn, B. Fong, J. Ottusch, and J. Visher, "Holographic artificial impedance surfaces for conformal antennas," in *2005 IEEE Antennas and Propagation Society International Symposium*, vol. 1B, 2005, pp. 256–259 vol. 1B.
- [202] B. H. Fong, J. S. Colburn, J. J. Ottusch, J. L. Visher, and D. F. Sievenpiper, "Scalar and tensor holographic artificial impedance surfaces," *IEEE Transactions on Antennas and Propagation*, vol. 58, no. 10, pp. 3212–3221, Oct 2010.
- [203] S. Maci, G. Minatti, M. Casaletti, and M. Bosiljevac, "Metasurfing: Addressing waves on impenetrable metasurfaces," *IEEE Antennas and Wireless Propagation Letters*, vol. 10, pp. 1499–1502, 2011.

- [204] D. Gonzalez-Ovejero and S. Maci, "Gaussian ring basis functions for the analysis of modulated metasurface antennas," *IEEE Transactions on Antennas and Propagation*, vol. 63, no. 9, pp. 3982–3993, 2015.
- [205] P. Nikitin, "Leon Theremin (Lev Termen)," *IEEE Antennas and Propagation Magazine*, vol. 54, no. 5, pp. 252–257, 2012.
- [206] T. Singh, S. Tedjini, E. Perret, and A. Vena, "A frequency signature based method for the RF identification of letters," in *2011 IEEE International Conference on RFID*, Apr. 2011, pp. 1–5.
- [207] F. Costa, S. Genovesi, and A. Monorchio, "A Chipless RFID Based on Multiresonant High-Impedance Surfaces," *IEEE Transactions on Microwave Theory and Techniques*, vol. 61, no. 1, pp. 146–153, Jan. 2013.
- [208] A. Vena, E. Perret, and S. Tedjini, "Chipless RFID tag using hybrid coding technique," *IEEE Transactions on Microwave Theory and Techniques*, vol. 59, no. 12, pp. 3356–3364, 2011.
- [209] A. Vena, E. Perret, and S. Tedjini, "A depolarizing chipless RFID tag for robust detection and its FCC compliant UWB reading system," *IEEE Transactions on Microwave Theory and Techniques*, vol. 61, no. 8, pp. 2982–2994, 2013.
- [210] F. Costa, M. Borgese, A. Gentile, L. Buoncristiani, S. Genovesi, F. A. Dicandia, D. Bianchi, A. Monorchio, and G. Manara, "Robust reading approach for moving chipless rfid tags by using isar processing," *IEEE Transactions on Microwave Theory and Techniques*, vol. PP, no. 99, pp. 1–10, 2017.
- [211] S. Preradovic and N. C. Karmakar, "Design of fully printable planar chipless RFID transponder with 35-bit data capacity," in *Microwave Conference, 2009. EuMC 2009. European*, Sep. 2009, pp. 013–016.
- [212] B. Shao, Q. Chen, Y. Amin, R. Liu, and L.-R. Zheng, "Chipless RFID tags fabricated by fully printing of metallic inks," *annals of telecommunications - annales des télécommunications*, vol. 68, no. 7-8, pp. 401–413, Aug. 2013.
- [213] F. Costa, S. Genovesi, and A. Monorchio, "Chipless RFIDs for Metallic Objects by Using Cross Polarization Encoding," *IEEE Transactions on Antennas and Propagation*, vol. 62, no. 8, pp. 4402–4407, Aug. 2014.
- [214] N. Barbot, O. Rance, and E. Perret, "Chipless rfid reading method insensitive to tag orientation," *IEEE Transactions on Antennas and Propagation*, 2020.
- [215] M. Borgese, F. Costa, S. Genovesi, and G. Manara, "Depolarizing chipless tags with polarization insensitive capabilities," *Electronics*, vol. 10, no. 4, p. 478, 2021.
- [216] S. Genovesi, F. Costa, F. A. Dicandia, M. Borgese, and G. Manara, "Orientation-insensitive and normalization-free reading chipless rfid system based on circular polarization interrogation," *IEEE Transactions on Antennas and Propagation*, vol. 68, no. 3, pp. 2370–2378, 2019.
- [217] M. Borgese, S. Genovesi, G. Manara, and F. Costa, "Radar cross section of chipless rfid tags and ber performance," *IEEE Transactions on Antennas and Propagation*, 2020.
- [218] L. Zheng, S. Rodriguez, L. Zhang, B. Shao, and L.-R. Zheng, "Design and implementation of a fully reconfigurable chipless RFID tag using Inkjet printing technology," in *2008 IEEE International Symposium on Circuits and Systems, ISCAS 2008; Seattle, WA; 18 May 2008 through 21 May 2008*, 2008, pp. 1524–1527. [Online]. Available: <http://www.diva-portal.org/smash/record.jsf?pid=diva2:437281>
- [219] L. Zhang, S. Rodriguez, H. Tenhunen, and L.-R. Zheng, "An innovative fully printable RFID technology based on high speed time-domain reflections," in *Conference on High Density Microsystem Design and Packaging and Component Failure Analysis, 2006. HDP'06*. IEEE, 2006, pp. 166–170. [Online]. Available: http://ieeexplore.ieee.org/xpls/abs_all.jsp?arnumber=1707587
- [220] I. Jalaly and I. Robertson, "Capacitively-tuned split microstrip resonators for rfid barcodes," in *Microwave Conference, 2005 European*, vol. 2. IEEE, 2005, pp. 4–pp.
- [221] —, "Rf barcodes using multiple frequency bands," *IEEE MTT-S Digest*, p. 4, 2005.
- [222] H.-S. Jang, W.-G. Lim, K.-S. Oh, S.-M. Moon, and J.-W. Yu, "Design of low-cost chipless system using printable chipless tag with electromagnetic code," *IEEE Microwave and Wireless Components Letters*, vol. 20, no. 11, pp. 640–642, 2010.

- [223] J. McVay, A. Hoorfar, and N. Engheta, "Space-filling curve RFID tags," in *2006 IEEE Radio and Wireless Symposium*. IEEE, 2006, pp. 199–202. [Online]. Available: http://ieeexplore.ieee.org/xpls/abs_all.jsp?arnumber=1615129
- [224] N. Lim, J. Kim, S. Lee, N. Kim, and G. Cho, "Screen printed resonant tags for electronic article surveillance tags," *IEEE Transactions on Advanced Packaging*, vol. 32, no. 1, pp. 72–76, 2009.
- [225] S. Preradovic, I. Balbin, N. C. Karmakar, and G. F. Swiegers, "Multiresonator-based chipless RFID system for low-cost item tracking," *IEEE Transactions on Microwave Theory and Techniques*, vol. 57, no. 5, pp. 1411–1419, 2009.
- [226] M. Manteghi, "A novel approach to improve noise reduction in the matrix pencil algorithm for chipless rfid tag detection," in *2010 IEEE Antennas and Propagation Society International Symposium*. IEEE, 2010, pp. 1–4. [Online]. Available: http://ieeexplore.ieee.org/xpls/abs_all.jsp?arnumber=5562223
- [227] S. Mukherjee, "Chipless radio frequency identification by remote measurement of complex impedance," in *Wireless Technologies, 2007 European Conference on*. IEEE, 2007, pp. 249–252. [Online]. Available: http://ieeexplore.ieee.org/xpls/abs_all.jsp?arnumber=4403993
- [228] I. Balbin and N. C. Karmakar, "Phase-encoded chipless RFID transponder for large-scale low-cost applications," *IEEE microwave and wireless components letters*, vol. 19, no. 8, pp. 509–511, 2009.
- [229] M. A. Islam and N. C. Karmakar, "A novel compact printable dual-polarized chipless RFID system," *IEEE Transactions on Microwave Theory and Techniques*, vol. 60, no. 7, pp. 2142–2151, 2012.
- [230] T. Chen, S. Li, and H. Sun, "Metamaterials application in sensing," *Sensors*, vol. 12, no. 3, pp. 2742–2765, 2012.
- [231] F. Costa, C. Amabile, A. Monorchio, and E. Prati, "Waveguide dielectric permittivity measurement technique based on resonant fss filters," *IEEE Microwave and Wireless Components Letters*, vol. 21, no. 5, pp. 273–275, May 2011.
- [232] E. M. Amin, J. K. Saha, and N. C. Karmakar, "Smart sensing materials for low-cost chipless rfid sensor," *IEEE Sensors Journal*, vol. 14, no. 7, pp. 2198–2207, July 2014.
- [233] F. Costa, A. Gentile, S. Genovesi, L. Buoncristiani, A. Lazaro, R. Villarino, and D. Girbau, "A depolarizing chipless rf label for dielectric permittivity sensing," *IEEE Microwave and Wireless Components Letters*, 2018.
- [234] M. Borgese, F. Dicandia, F. Costa, S. Genovesi, and G. Manara, "An Inkjet Printed Chipless RFID Sensor for Wireless Humidity Monitoring," *IEEE Sensors Journal*, vol. PP, no. 99, pp. 1–1, 2017.
- [235] A. Vena, E. Perret, D. Kaddour, and T. Baron, "Toward a Reliable Chipless RFID Humidity Sensor Tag Based on Silicon Nanowires," *IEEE Trans. Microw. Theory Techn.*, vol. 64, no. 9, pp. 2977–2985, Sep. 2016.
- [236] D. Girbau, . Ramos, A. Lazaro, S. Rima, and R. Villarino, "Passive wireless temperature sensor based on time-coded uwb chipless rfid tags," *IEEE Transactions on Microwave Theory and Techniques*, vol. 60, no. 11, pp. 3623–3632, Nov 2012.